

PFC/RR-95-7

**Stress Assisted Intergranular Oxidation Cracking
of Incoloy Alloy 908.**

M.M. Morra
June 1995

Plasma Fusion Center
Superconducting Magnet Development Group
Massachusetts Institute of Technology
Cambridge, MA 02139 USA

This work was supported by the United States Department of Energy, Office of Fusion Energy grant number DE-FC02-93ER54186. Reproduction, translation, publication, use, and disposal, in whole or in part, by or for the United States Government is permitted.

Stress Assisted Intergranular Oxidation Cracking of Incoloy Alloy 908.

by Martin M. Morra

for the Superconducting Magnet Development Group of the MIT Plasma Fusion Center

ABSTRACT

Constant load stress rupture tests were performed on alloy 908. The test matrix used varied oxygen concentration, applied load, temperature, and percent cold work. The effect of modifying surface residual stresses on intergranular oxidation and cracking was examined using constant strain C-ring tests.

The mechanism for high temperature intergranular fracture in alloy 908 is stress assisted intergranular oxidation. Under an applied or residual tensile stress, the depth of intergranular oxidation increases with increasing oxygen concentration. This result is shown to be comparable to the oxidation assisted, intergranular fracture behavior observed for alloy 718. Intergranular cracking did not extend beyond the depth of intergranular oxidation.

Intergranular oxidation in alloy 908, at low temperatures (550 - 800°C), requires the presence of a residual or an applied tensile stress to occur. Tested under identical conditions, non-stressed material did not exhibit intergranular oxidation. The intergranular oxidation zone penetrates to the same depth as predicted for internal (matrix) oxidation. This result can be correlated to that observed in other Ni-Fe and Ni base superalloys and is controlled both by the concentration of oxygen in the environment and the concentration of chromium in the alloy. Analogous to internal oxidation models, a transition from intergranular to external oxidation in alloy 908 occurs when the oxygen concentration at the surface is below 0.1 ppm. The activation energy for intergranular oxidation in air was determined to be 202 kJ/mole for this alloy.

An oxygen concentration threshold based on zero percent intergranular fracture is a better indicator of the potential for intergranular fracture during heat treatment than one based on time to rupture. Control of furnace atmosphere chemistry during heat treatment is essential for the successful heat treatment of alloy 908. An oxygen concentration of below 0.1 ppm is required to heat treat this material under applied or residual tensile stresses. The elimination of residual tensile surface stresses by applying compressive residual stresses through shot peening or reduction in tensile stresses through vacuum stress relief heat treatments eliminates stress assisted grain boundary oxidation.

TABLE OF CONTENTS

Section	Page
INTRODUCTION	8
Key Points, Stress Accelerated Intergranular Oxidation Cracking	10
BACKGROUND	11
Fatigue Crack Growth Rate in Air Versus Vacuum	11
Tensile Embrittlement and Stress Rupture Life	13
Role of Microstructure and Alloy Chemistry	13
Effects of Oxygen Partial Pressure and Stress on Intergranular Oxidation	14
Intergranular Oxidation	17
Application to Stress Accelerated Grain Boundary Oxidation in Alloy 908	19
PROCEDURES	21
Material	21
Stress Rupture Test Procedure	25
C-Ring Residual Stress Modification Study	30
RESULTS	32
Stress Rupture	32
Effect of Oxygen Concentration	35
Interrupted and Non-Loaded Flat Plate Tests	44
Round Bar Microstructure and Fractography	46
Grain Boundary Analysis	53
Modification of Residual Stresses in C-Ring Test Samples	73
SUMMARY OF RESULTS	82
ANALYSIS OF STRESS ACCELERATED GRAIN BOUNDARY OXIDATION	83
CONCLUSIONS	93
Stress Accelerated Grain Boundary Oxidation, as Internal Oxidation	93
Stress Accelerated Grain Boundary Oxidation, Applied	94
REFERENCES	95

LIST OF FIGURES

<u>Figure</u>	<u>Description</u>	<u>Page</u>
1	Variation in fatigue crack growth rate with test frequency and temperature for alloy 718 at 550 and 650°C.	12
2	Fatigue crack growth rate as a function of the oxygen partial pressure under constant ΔK (20 and 28 $\text{Mpa}\sqrt{\text{m}}$) at 650°C in alloy 718.	16
3	Percent intergranular fracture in alloy 718 slow strain rate test (8.3×10^{-4} mm/s) at 650°C versus oxygen partial pressure.	16
4	Lateral growth of Cr_2O_3 layer originating from grain boundaries.	19
5	(a) Grain size and orientation of 3.43 mm thick sheet starting material, heat Y9401K, grain diameter 13 μm . (b) Grain size in tested stress rupture sample (650°C/118 hours).	23
6	(a) (b) Optical micrographs showing grain size in the flat plate sample, and round bar sample, respectively, that had been vacuum heat treated at 650°C for 200 hours. (c) optical micrograph of elongated grains in 20% cold worked material, heat Y9210.	24
7	Double edge notch stress rupture specimen.	26
8	Double notch round bar stress rupture specimen.	27
9	C-ring specimen holder designed to maintain a constant plastic strain of 6% during heat treatment.	31
10	Comparison of 650°C flat plate test sample stress rupture data for alloy 908 in argon with controlled oxygen concentration and the same heat treat of material but with 5% cold work and tested in air.	33
11	Comparison of 20% cold work double notch round bar air data from with low oxygen concentration test data for the same heat of material with 20% cold work, 10% cold work, and solution annealed starting conditions.	34
12	Comparison of time to rupture versus stress for vacuum heat treated then tested samples with samples tested in their as received condition.	36
13	Characteristics of flat plate stress rupture fracture surfaces as a function of oxygen concentration.	37
14	SEM micrographs comparing the intergranular fracture morphology in 650°C/650MPa samples as a function of oxygen concentration.	38
15	Effect of temperature on time to rupture versus stress for solution annealed flat plate samples at 750, 700 and 550°C for different ranges of oxygen concentration.	40

LIST OF FIGURES

<u>Figure</u>	<u>Description</u>	<u>Page</u>
16	SEM micrographs showing the effect of temperature on fracture morphology for a stress of 650 MPa and 195 ppm O ₂ .	41
17	Percent intergranular fracture versus oxygen concentration for 650°C and 651±18 MPa stress range flat plate test samples.	42
18	Percent intergranular fracture versus oxygen concentration for all samples, tested at 650°C and for all stress levels tested, range 535 ± 140 MPa.	43
19	Comparison of 650°C Inconel 718 slow strain rate (8.3x10 ⁻⁴ mm/s) tensile data from Andrieu with 650°C notched stress rupture data from alloy 908 in the 649 ± 18 MPa stress range.	45
20	Cross-section near unfailed notch showing elongated grain at the notch and crack path in a 20% cold-worked 650°C round bar test sample.	47
21	Ratio of ductile fracture area to total fracture area versus oxygen concentration for flat plate samples at 650°C and 651.5 ± 18 MPa stress range.	48
22	Larson-Miller parameter plot of low oxygen concentration flat plate test data compared with 5% cold work flat plate test data.	50
23	Larson-Miller parameter plot of round bar low oxygen concentration data for 20% cold work and solution annealed conditions compared with round bar data for 20% cold work material in air.	51
24	Plot of isostress lines and least squares fits for 650 and 540 MPa stresses.	54
25	“Master curve” for solution annealed flat plate stress rupture data based on new material constant C = 30.	55
26	(a) Normarski optical micrograph of the crack path at the unfailed notch in a 650°C round bar sample. (b) SEM micrograph of affected grain boundaries in a 650°C round bar sample.	57
27	SEM micrograph and oxygen x-ray map of grain boundaries in a 650°C sample (10% cold, work 1000 ppm O ₂ , 469 MPa) 8.2 hours to failure.	58
28	EDS X-ray map of elements present along grain boundaries at the unfailed notch of a round bar sample tested at 650°C, 469 MPa, and 1000 ppm O ₂ .	59
29	Grain boundary at triple point, from 650°C sample round bar sample (1000 ppm O ₂ , 650 MPa, 4 hours to failure), selected for EDS composition profile.	60

LIST OF FIGURES

<u>Figure</u>	<u>Description</u>	<u>Page</u>
30	EDS composition profile across a grain boundary in a 650°C round bar sample (650 MPa, 1000 ppm O ₂ , 4 hours to failure).	61
31	EDS composition profile across an affect grain boundary in a 650°C round bar sample (469 MPa, 1000 ppm O ₂ , 12.3 hours to failure).	62
32	(a) SEM micrographs of oxidized grain boundaries in a 650°C flat plate sample (650 MPa, 38 ppm O ₂ , 122 hours to rupture). (b) Micrograph of grain boundary selected for compositional analysis by EDS.	64
33	EDS composition profile along grain boundary extending to terminus in a 650°C flat plate sample (650 MPa, 38 ppm O ₂ , 122 hours to failure).	65
34	EDS composition profile across grain boundary in a 650°C flat plate sample (650 MPa, 38 ppm O ₂ , 122 hours to failure).	66
35	SEM micrograph of crack at notch in a round bar sample (650 MPa, 1000 ppm O ₂ , 3.65 hours to failure).	67
36	EDS composition profile along grain boundary in a 650°C round bar sample (650 MPa, 1000 ppm O ₂ , 3.65 hours to failure).	68
37	Arrhenius activation energy, Q_{gb} plot for intergranular oxidation in alloy 908 in air. Based on round bar stress rupture data.	72
38	Optical micrograph showing cross section of the outer surface of shot peened sample.	74
39	Microhardness profiles across thicknesses of C-ring samples.	75
40	Ratios of elements present (balance oxygen) in oxides electrolytically extracted from the surfaces of C-ring s that were heat treated under degraded vacuum conditions (10^{-2} Torr range).	77
41	High magnification SEM micrographs taken near the inside diameter of the cracked cross section of a C-ring that failed within 24 hours at 650°C in a 4×10^{-2} Torr vacuum.	79
42	High magnification SEM micrographs taken along the cracked cross section of C-ring S37 after failing within 24 hours at 650°C in a 4×10^{-2} Torr vacuum.	80
43	Transition from internal to external oxidation for Ag-In alloys at 550°C.	84
44	Concentration profile for the exclusive internal oxidation of alloys.	88
45	SEM micrograph showing cross section through the oxidized surface of heat treated alloy 905.	88

LIST OF FIGURES

<u>Figure</u>	<u>Description</u>	<u>Page</u>
46	Comparison of experimental and calculated intergranular oxidation depths as a function of surface oxygen concentration at 650°C and 650 MPa.	90
47	Intergranular oxidation zone (of depth ξ) developed under tensile loading.	91
48	Time to develop a 0.5 mm deep zone of internal oxidation in three alloys at 650°C as a function of oxygen concentration and mole fraction Cr.	92

LIST OF TABLES

<u>Table</u>	<u>Description</u>	<u>Page</u>
1	Compositions of Alloy 908 Used for Stress Rupture Testing.	22
2	Test Matrix Used For Stress Rupture Tests.	28
3	Compositions of Surface and Grain Boundary Oxides From Alloy 908 Stress Rupture Samples.	70
4	Alloy 908 C-Ring Test Results at 650°C, 6% Plastic Strain.	73

INTRODUCTION

Alloy 908 was developed as a Nb₃Sn Cable-In-Conduit-Conductor (CICC) magnet sheathing material. [1] It can be characterized as a low coefficient of thermal expansion iron-nickel base superalloy that contains 4 weight percent chromium. Its chemistry, microstructure and mechanical properties have been optimized for Cable-In-Conduit-Conductor (CICC) use while maintaining a coefficient of expansion that is compatible with this application. Aside from coefficient of expansion considerations, alloy 908 was formulated to precipitation harden and yet remain metallurgically stable for a range of Nb₃Sn heat treatments. [1] The development of alloy 908 centered on three areas that were necessary for its successful application as a low coefficient of expansion cryogenic structural material. These were; its mechanical properties at cryogenic temperatures, welding, and its susceptibility to stress assisted intergranular oxidation cracking. The latter of these is the area with which this report will deal. The application, development, and properties have been reported in other publications. [1, 2, 3, 4]

Chromium has important and contrary effects in low coefficient of expansion superalloys. For the aerospace applications for which they were developed these alloys do not contain chromium. This is because a relatively small increase in the weight percent chromium can have a strong effect on increasing the coefficient of thermal expansion. [5, 6, 7] Increasing the amount of chromium can, however, improve their resistance to stress assisted intergranular oxidation. For the CICC magnet application a balance between these two factors must be maintained. Over the temperature range of interest, 4K to 1000K, the addition of 4 wt.% chromium resulted in an acceptable increase in the mean coefficient of thermal expansion. [1, 2] Stress-rupture tests performed during the development stage of alloy 908 showed that adding 4 weight percent chromium improved its notch-rupture behavior in air over that of the extremely notch-sensitive alloy 903. [1] The effect of chromium addition is incremental with respect to a material's susceptibility to stress assisted intergranular oxidation. So although the effects of oxygen can be seen in Ni or Ni-Fe base superalloys with high chromium levels (18 wt%), the speed at which intergranular oxidation cracking occurs generally decreases with increasing chromium concentration. This translates into longer stress rupture lives at higher chromium levels. Other studies have verified the beneficial effect that chromium has on stress rupture behavior. [8] Addition of 2 wt.% chromium to an experimental Ni-Fe-Co base low coefficient of expansion superalloy has been shown to double the stress-rupture life over a similar chemistry alloy but without chromium. [9] Adding 5 wt.% chromium to another Ni-Fe-Co base low coefficient of expansion alloy improved both its overall oxidation resistance and

stress-rupture life. [10] The stress-rupture behavior of alloy 908 at high temperature in air show characteristics that indicate its susceptibility to stress accelerated grain boundary oxidation. [11]. While the data indicated adequate life expectancy in air for very low stress levels (< 200 MPa), the actual stresses in the pre-heat treatment conduit, from plastic deformation during conduit fabrication and from magnet winding, have not been established. It is anticipated that residual stresses from tube forming and/or extrusion, winding and elastic strains due to constraining the coil after winding will be present. For the magnet designers, a map of the stress accelerated grain boundary oxidation regime for alloy 908 in terms of furnace oxygen concentration and stress, will be essential for the successful heat treatment of large scale Cable-In-Conduit-Conductor magnets.

There is no question that such structures can be successfully heat treated in vacuum. [12, 13] Heat treatment in an argon atmosphere, however, may also be considered. The problem with this approach is that the oxygen concentrations in inert gases may exceed the threshold level for alloy 908.

The goal of this study was threefold. [14] First, from the perspective of Cable-In-Conduit-Conductor magnet heat treatments, is to determine what level of environmental control over oxygen concentration is required to prevent intergranular cracking. Second, and more basically, what is the relationship between oxygen concentration, stress and temperature that leads to intergranular failure in this alloy? And lastly, the role of the above variables as related to the fundamental mechanism of stress accelerated grain boundary oxidation cracking. The effect of modification of surface residual stresses on stress accelerated grain boundary oxidation will also be examined.

Key Points, Stress Accelerated Intergranular Oxidation Cracking

- **Stress accelerated intergranular oxidation cracking requires two components in order to occur in the low temperature range utilized to heat treat CICC magnets (550°C-750°C).**

The first, and most obvious component is oxygen. Studies on numerous Ni, Fe, and Ni-Fe base alloys have shown that the threshold for oxygen lies between 1×10^{-3} and 1×10^{-4} Torr. The second component is residual or applied tensile stress. This component is essential for temperatures below 1000°C. The reason for this is linked to the values for matrix versus intergranular diffusion of both oxygen and the oxidizing species in the alloy. Below 1000°C intergranular diffusion is predominant and transport occurs along this short circuit pathway. Above 1000°C matrix diffusion assumes a greater role in the transport of oxidizable species.

- **The embrittling effects of intergranular oxidation are short range, i.e., the grain boundaries ahead of the intergranular oxidation zone are not embrittled by oxygen.**

This study will show that the depth of intergranular fracture extends only to the depth of intergranular oxidation. This point has been verified for many other superalloys. When the environment surrounding fatigue test samples is changed during testing from an oxygen containing environment to vacuum or to a low ppm oxygen inert gas, an almost immediate cessation of intergranular crack growth occurs.

- **For CICC magnets, the source of stress during heat treatment will be residual from reduction of conduit cross section and winding. If the source of stress can not be eliminated then strict control of oxygen levels during heat treatment is necessary.**

The most practical way to eliminate surface residual stresses is to place the surface in compression by shot peening. If atmosphere control is used, then continuous monitoring of oxygen levels in the furnace atmosphere and the conduit cable space purge gas is essential.

BACKGROUND

There are two primary areas of research that deal with oxygen's intergranular behavior. The first of these are studies that are concerned with the effect of oxygen on high temperature fatigue, creep and stress rupture in Ni and Ni-Fe base superalloys. Second are intergranular oxidation studies covering a range of materials. In many aspects, these two areas overlap.

The phenomenon of oxygen induced embrittlement in materials had been recognized early on to explain differences in mechanical behavior between vacuum and air. While the success of most high temperature alloys has not been hampered by its existence, there are different degrees to which this phenomenon manifests itself.

The list of Ni and Ni-Fe base superalloys that have been reported to exhibit intergranular oxygen effects is fairly extensive. With respect to the effect of oxygen on fatigue fracture, two reviews give fairly wide coverage. Ericsson provides an extensive listing of researchers and materials studied, in which the effect of oxygen on fatigue fracture has been examined. [15] Gell and Duquette have reviewed some of the proposed mechanisms for oxygen's effect on fatigue fracture. [16] A more recent work by Pineau provides an update on some of these mechanisms and provides a more specific overview of oxidation related fracture mechanisms. [17]

Fatigue Crack Growth Rate in Air Versus Vacuum

Early studies on fatigue crack growth reported on the interaction of oxidation processes with dislocation motion that prevents slip band reversal. [18, 19] Other researchers reported higher crack growth rates for fatigue tests performed in air compared with those performed in vacuum. [20, 21] The effect of oxygen can be seen on transgranular and single crystal crack growth rates, as well as intergranular crack growth. [16] . The stress accelerated grain boundary oxidation phenomenon in low coefficient of expansion iron-nickel base alloys is essentially an intergranular effect, so the following discussion will center on behavior leading to increased intergranular crack growth rates.

Intergranular crack growth during fatigue loading is encountered at high temperatures (above 500°C), in combination with oxygen containing environments and low frequencies (≤ 0.05 Hz). [22, 23, 24, 25, 26, 27, 28, 29] Similar environmental effects have been found in creep crack growth studies on Ni-base and Ni-Fe base superalloys. [23, 30, 31, 32, 33] Under dynamic test conditions, such as fatigue loading, the environmental effect of oxygen becomes apparent as the loading frequency is decreased. This is because there is

a time interval required for the damaging species, in this case oxygen, to react with the material. As the loading frequency is increased, mechanical damage surpasses the rate at which the environmental damage done by oxygen can occur, in this case intergranular oxidation. In general, the fatigue crack growth process is time dependent if it increases with increasing temperature and/or decreasing frequency. In the case of intergranular oxidation damage, as the loading frequency is decreased, the crack path changes from transgranular to intergranular. [34] An increase in the fatigue crack growth rate is also associated with the transition to intergranular crack propagation. The effects of loading frequency on the mode of crack growth and on crack growth rate in air are illustrated for alloy 718 in Figure 1. In contrast to dynamic loading, under static loading, the crack growth processes are completely time dependent. Sadananda, et al., reviewed the effects of test variables and environment on crack growth in Ni-base superalloys. [35] The mechanical and environmental variables found to influence fatigue crack growth in alloy 718 have been catalogued in two recent review papers by Ghonem, et al. [28, 36]

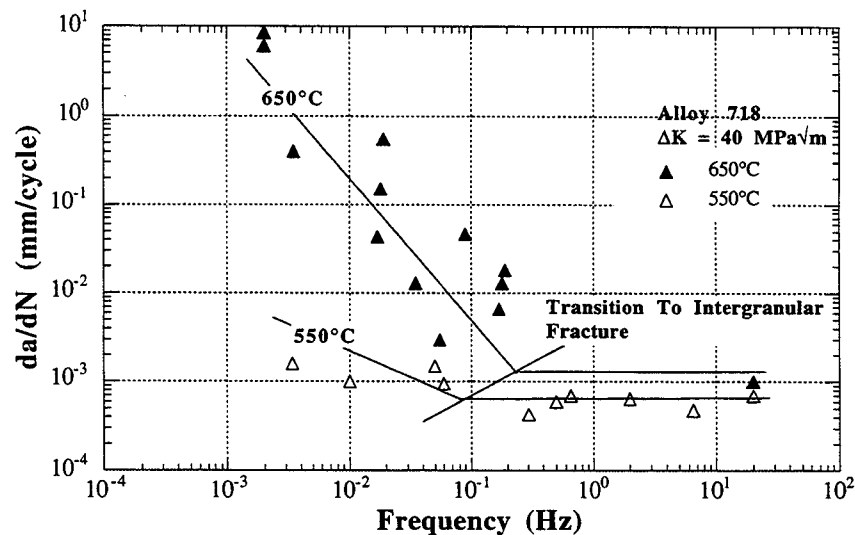


Figure 1. Variation in fatigue crack growth rate with test frequency and temperature for alloy 718 at 550 and 650°C ($\Delta K = 40 \text{ MPa}\sqrt{\text{m}}$). From Pedron, et al., [24]

Floreen and Kane performed an extensive study on the effects of many different furnace environments on fatigue crack growth in alloy 718. [37] Their test methodology utilized low frequency (less than 0.1 Hz) fatigue loading to study environment-dependent crack growth. Another factor considered in their study was the water vapor concentration in the test atmosphere. Here, Floreen and Kane found that relatively high amounts (50,000

ppm) of water vapor in helium were necessary to produce fatigue crack growth rates comparable to those in helium containing 100 ppm oxygen. The same amount of water vapor in hydrogen gas produced fatigue crack growth rates between those of air and helium. The addition of water vapor to air did not result in any significant increase in fatigue crack growth rate. They concluded from helium plus oxygen and the helium plus water vapor tests that oxygen was produced by the reaction between the alloy and water vapor, and was responsible for the increase in fatigue crack growth rate. [37]

Tensile Embrittlement and Stress Rupture Life

Results from Chang's early research showed high temperature tensile embrittlement of several Ni-base superalloys. He attributed this embrittlement to interactions between grain boundary γ' , $\text{Ni}_3(\text{Al,Ti})$, phase and oxygen. [38]

In a series of papers, Woodford and Bricknell examined the effect of oxygen on the tensile embrittlement in different purity grades of nickel. [39, 40, 41, 42] Their test methodology involved very high temperature (1000°C) air or vacuum exposure followed by tensile testing in inert gas or vacuum at temperatures ranging from 25 to 1000°C. Through the use of a series different test atmospheres they identified oxygen as the embrittling species. The effect of oxygen on the temperature dependence of tensile embrittlement was postulated to be the result of decreased grain boundary mobility as a result of oxygen penetration. [39, 40] In addition to studies on nickel, Bricknell and Woodford also examined the effect of prior air exposure on the stress rupture life of some Ni-base and Co-base superalloys. [43, 44]

Role of Microstructure and Alloy Chemistry

The role of grain boundary microstructure appears to influence oxygen embrittlement in two ways. First, and most directly, grain boundary phases act to getter oxygen diffusing along the grain boundary by oxidizing. Second, and less directly, the precipitation and growth of intergranular phases alters grain boundary chemistry, and hence oxidation characteristics.

Pédrón, et al., reported three microstructural features in alloy 718 that reduced the creep crack growth rate in air. [24] Those were increased grain size, coarsening of the γ' (body centered tetragonal, Ni_3Nb) strengthening phase, and intergranular precipitation of orthorhombic δ (Ni_3Nb) phase. Chang found that a deformed grain structure in alloy 718

reduced the fatigue crack growth rate but found less grain size dependence. [27] Floreen, et al., reported that overaging of alloy 718 reduced both the fatigue and creep crack growth rates. [22] Coarse grain size has been reported to reduce crack growth rates. [23] Oxidation of primary (Nb,Ti)C carbides has been observed in many superalloys, and it has been suggested that preferential carbide oxidation may be a factor that contributes to grain boundary embrittlement. [33, 45, 46]

Woodford found that hafnium and boron alloying additions alleviated the detrimental effects of oxygen. [44] Other work showed that boron added to nickel and alloy 903A segregated to grain boundaries due to its low matrix solubility and eliminated intergranular embrittlement. [42, 47, 48] Chang reported that chromium additions to alloy 718 (30 wt.%) improved cracking resistance in the time dependent fatigue crack growth regime. [27].

Early work by Wilson examined the effect of microstructure on stress-rupture properties of alloys 718 and Waspaloy. [49, 50] He reported time-dependent notch sensitivity in the temperature range of 482-649 °C, with cracking occurring in the intergranular mode. Overaging resulted in reduced notch sensitivity. In alloy 718 the overaging treatment that resulted in improved properties introduced intergranular δ (orthorhombic Ni_3Nb) phase. These results were similar to those of Pédrón discussed above. Other grain boundary microstructures can have detrimental effects on stress rupture properties. Reductions in stress rupture lives have been reported in Ni-base superalloys in which intergranular γ' precipitation occurs. [38, 51]

Effects of Oxygen Partial Pressure and Stress on Intergranular Oxidation

The composite goal of all the research categorized above was to attain an understanding of how oxygen and the affected grain boundaries interact to produce embrittlement. Parallel studies on the effect of oxygen on intergranular stress corrosion cracking in aqueous systems can also be found. [52]

The studies cited above have focused on changes that occur when testing is performed either in air versus vacuum or in air versus inert gas. One problem with the use of inert gas testing is that a finite oxygen concentration is present in most "inert" gases. Experiments that examine the effect of changing the partial pressure of oxygen are more pertinent to controlling furnace atmospheres to prevent stress accelerated grain boundary oxidation in alloy 908. These studies are less numerous in the literature.

In most cases, the effect of changing oxygen partial pressure manifests itself as a sigmoidal curve, with the abscissa being the partial pressure of oxygen and the ordinate some mechanical test parameter. Typically, the upper and lower plateaus in these curves correspond to oxygen partial pressures above or below which the test parameter shows no change. [20, 21]

Surprisingly few studies have been carried out to study the effect of oxygen partial pressure on fatigue or creep crack growth rate until relatively recently. Most of the recent research in this area has been focused on alloy 718, and many of the results from work on that alloy may be applicable to understanding the oxygen embrittlement phenomenon in alloy 908.

One of the most recent and complete studies that examined the effect of changing oxygen partial pressure on intergranular crack tip oxidation in fatigue was performed by Andrieu. [53, 54, 55] Andrieu observed a change in fatigue crack growth rate with changing oxygen partial pressure. A plot illustrating his da/dN versus oxygen partial pressure results is shown in Figure 2. As seen in this figure there are two transitions in da/dN , one between 1×10^{-3} and 1×10^{-2} Torr and the other near 1 Torr. The most significant result of this research is the proposal of an intergranular oxidation mechanism to explain the effects seen with changes in oxygen partial pressure. [54]

The mechanism they proposed is linked to the slow strain rate test results that showed an increase in the percent intergranular fracture surface with increasing oxygen partial pressure in alloy 718. [53] These results are shown in Figure 3. A transition between all intragranular fracture and mixed transgranular/intergranular was found to occur between 1×10^{-4} and 1×10^{-3} Torr. The relationship between percent intergranular fracture and oxygen partial pressure is similar to the fatigue crack growth rate behavior observed for alloy 718 as a function of oxygen partial pressure. [55] These results were correlated with Andrieu's Auger analysis of oxides formed on electropolished surfaces of alloy 718 at 650°C. [53] In this analysis, the composition of the oxide(s) formed was determined as a function of oxygen partial pressure. Based on the similarity in the surface oxidation behavior and the sigmoidal shape of the percent intergranular fracture versus oxygen partial pressure curve a two-stage oxidation process was hypothesized .

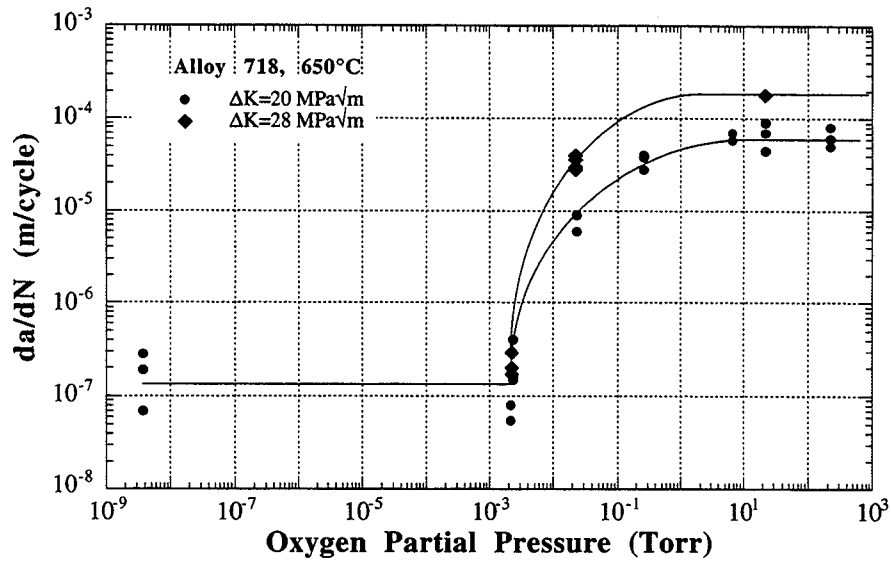


Figure 2. Fatigue crack growth rate as a function of the oxygen partial pressure under constant ΔK (20 and 28 $\text{MPa}\sqrt{\text{m}}$) at 650°C in alloy 718. From Andrieu, et al. [55]

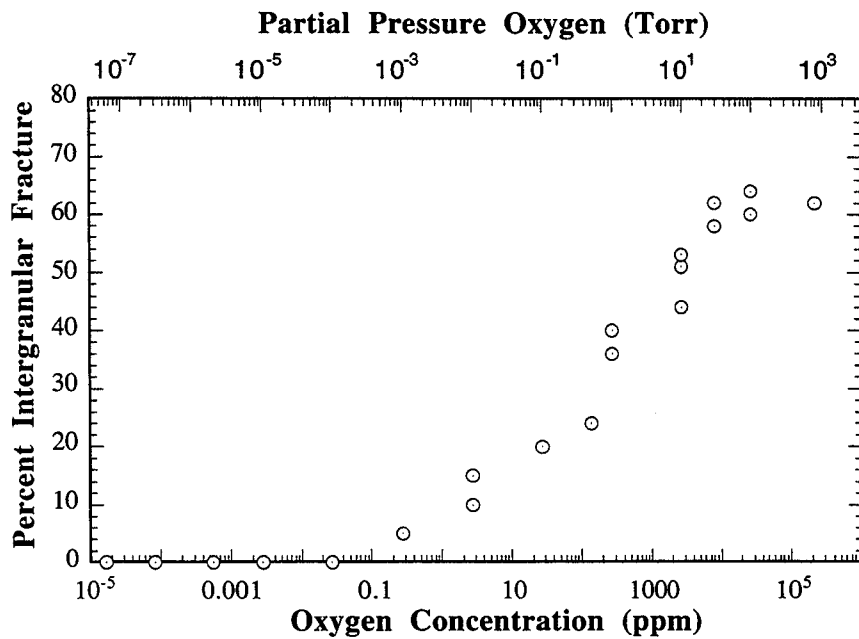


Figure 3. Percent intergranular fracture in alloy 718 slow strain rate test ($8.3 \times 10^{-4} \text{ mm/s}$) at 650°C versus oxygen partial pressure. Data from Andrieu. [53]

In the proposed mechanism intergranular oxidation is influenced by the relative rates of formation of porous non-protective oxides, (Ni,Fe)O, versus those of the passivating chromium containing oxides, Cr₂O₃ and NiCr₂O₄. The kinetics of this process depend upon; the diffusion rate of oxygen through the porous (Ni,Fe)O oxides, temperature, partial pressure of oxygen, diffusion of chromium, and localized stress and strain. [54] The first stage of oxide formation would be predominated by the formation of intergranular FeO and NiO and their spinels. [54] This is generally the result of the faster kinetics for (Ni,Fe)O formation than for Cr₂O₃ or NiCr₂O₄. [56] After some transition time, the chromium-rich oxides precipitate ahead of the oxygen porous (Ni,Fe)O intergranular oxide front and passivate the material, thereby blocking further ingress of oxygen. This transition time was termed the “oxide saturation” time by Andrieu. [78] As the partial pressure of oxygen is lowered, less oxygen is available for transport through the porous oxides. The result is that the oxygen partial pressure at the intergranular oxidation front is driven low enough to thermodynamically favor the formation of chromium-rich oxides. During fatigue loading, this passivation process will be repeated as the former oxide layer is ruptured for each cycle. The frequency of fatigue loading will determine the depth of intergranular oxidation that can occur before rupture restarts the process. Ghonem and Zheng developed a model that attempts to quantify many of the above experimental observations. [57, 58] In correspondence to Andrieu’s work, they invoke a two-stage oxidation process to explain fatigue crack tip oxidation. Their proposed model depends upon the rate of formation of chromium-rich versus that of other oxide types. In this model, the rate at which chromium-rich oxides form depends upon both the intergranular diffusion of oxygen and the transport of chromium from the alloy matrix via a mobile dislocation network. [57]

Intergranular Oxidation

With the research cited above concerning oxide formation the relevance of controlling oxygen partial pressure becomes more apparent. Studies on Ni-Cr alloys provide some clues as to the effect of oxygen partial pressure and concentration on intergranular oxidation. Rapp has classified the Ni-Cr system as Class 3. [59] Materials that fall into this class are dilute alloys of the base metals Ni, Fe, and Co alloyed with Cr, Al, V, and Ti. [59] Because their oxidation behaviors fall into the same class, Ni-Cr alloys can be used to model oxidation of Ni and Ni-Fe base superalloys. [56, 59] The primary oxide types (NiO and Cr₂O₃) formed in this class are p-type, cation deficient. The surface oxide is formed by

cation diffusion from the metal into the scale and then through the scale to the oxide/gas interface.

Intergranular oxidation can be defined as the precipitation of oxides at grain boundaries. [60] Internal oxidation is the process by which oxygen diffuses into an alloy and causes subsurface precipitation of the oxides of one or more alloying elements in the alloy's matrix. [59, 61] To oxidize internally, the alloying elements must form oxides that are thermodynamically more stable than those of the solvent metal. [62] For internal oxidation without external scaling, the oxygen partial pressure in the environment must be greater than that required to oxidize the alloying element but less than that required to oxidize the solvent metal. [61] Even under internal oxidation conditions, grain boundary oxide precipitation is favored because grain boundaries are preferred nucleation sites and the oxidizable alloying elements may be segregated at the grain boundaries. [61] Also, the combination of the low solubility of oxygen in nickel and the fast grain boundary path for oxygen diffusion promotes intergranular oxidation. Based on internal oxidation experiments, the lattice diffusivity of oxygen in nickel has been estimated to be 1.14×10^{-11} m²/s at 1000°C, and approximately 4.27×10^{-16} m²/s at 650°C. [63, 64] In contrast, based on Hwang and Balluffi's work, the grain boundary diffusivity in nickel has been estimated to be on the order of 2.5×10^{-12} m²/s at 650°C. [65] Grain boundary diffusion of the oxidizable solute elements can also be expected to be faster than lattice diffusion. In a Ni-20Cr alloy at 1000°C, for example, the ratio of tracer diffusion coefficients of Cr and Ni, $(D^*_{Cr}/D^*_{Ni})_{g.b.}$, equals 11. [66] For lattice diffusion in Ni-Cr alloys at 1020°C, $(D^*_{Cr}/D^*_{Ni})_{lattice}$ equals 1.7. [66] Also, as the temperature is lowered grain boundary diffusion becomes more rapid relative to lattice diffusion.

Wood, et al., examined Ni-Cr alloys with chromium concentrations ranging from 1 to 5 wt.%. [67] One general observation from their study was that grain boundary diffusion was more significant than lattice diffusion at low temperatures (< 1000°C). Under low P(O₂) conditions, they observed greater intergranular Cr₂O₃ formation than at high P(O₂), where NiO formation was favored.

To review some general elements on the oxidation of Ni-Cr alloys:

- The critical minimum chromium content to ensure the formation of a protective surface oxide is approximately 20 to 25 wt.%. [68].
- The oxide growth rate for NiO is faster than that of Cr₂O₃. [56, 69]
- Preferential growth of the Cr₂O₃ layer down grain boundaries is linked to the short circuit diffusion path provided for chromium by the grain boundaries. [56, 68]

- The fast growing NiO nuclei overgrow the slower growth Cr₂O₃ nuclei. [56]
- An intermediate layer of the spinel NiCr₂O₄ forms. [56, 59]
- The Cr₂O₃ sublayer grows laterally from grain boundary/surface intersections until it forms a continuous layer, this is illustrated in Figure 4. [56, 68]
- The surfaces of fine-grained materials develop better surface area coverage with Cr₂O₃ than large grain materials. A fine grain size results in more sites for diffusion of chromium and shorter lateral growth distances. [70]
- Growth of the Cr₂O₃ layer results in depletion of chromium from the matrix. [56, 68]
- Between 800 and 1200°C and when the concentration of chromium is less than 5 wt.%, Cr₂O₃ is formed internally both at grain boundaries and within the interior of the grains. Under these conditions the alloy is covered by a NiO layer. [68]

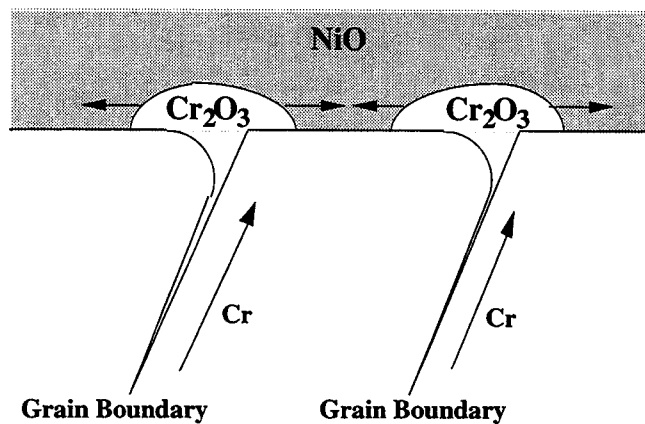


Figure 4. Lateral growth of Cr₂O₃ layer originating from grain boundaries.

Application to Stress Accelerated Grain Boundary Oxidation in Alloy 908

Susceptibility to the oxygen embrittlement phenomenon, by whichever mechanism, can be arranged by alloy group. The hierarchy of this arrangement would appear as,

{Ni/Fe aluminides > LCIN superalloys > Ni-Fe base superalloys ≥ Ni-base superalloys}.

In this ordering the Ni/Fe aluminides are the most susceptible to intergranular oxygen embrittlement. Low coefficient of expansion iron-nickel base superalloys are next in line followed by the Ni-Fe and Ni base superalloys. Co-Cr base superalloys are not ranked

because they are much less susceptible to oxygen effects due to their greater intrinsic ductility at high temperature. [45] The ranking listed above correlates well with decreasing amounts of chromium found in each material, 0 wt.% for Ni aluminides, 0-5 wt. % in low coefficient of expansion iron-nickel base superalloys, and 10 to 20 wt. % in superalloys.

One result suggested by these studies is that the addition of small quantities (< 5 wt. %) of chromium may not be of help in completely eliminating stress accelerated grain boundary oxidation. As most of the above research indicates, alloys with relatively high chromium concentrations (18 wt.%) experience similar intergranular oxidation assisted cracking, although their crack growth rates are lower. The one beneficial effect of having increased chromium levels may be in accelerating the rate of external oxidation (passivation). In the oxidation of Ni-Cr alloys, higher chromium contents translate to more rapid transition from internal to external oxidation.[70] Since stress accelerated grain boundary oxidation is an internal oxidation process, increasing the chromium content will, in effect, accelerate the formation of a passivating surface oxide. Chang's work on high chromium chemistries of alloy 718 demonstrated this. [27] Coefficient of expansion considerations restrict increases in chromium in low coefficient of expansion iron-nickel base alloys. In this case, reducing the diffusion rate of oxygen down grain boundaries may be of greater practical value. Grain boundary precipitation or segregation of oxygen getter phases and elements, respectively, is one example of this approach.

Internal/intergranular oxidation experiments are generally static tests. Stress accelerated grain boundary oxidation requires that the influence of stress on intergranular oxidation be recognized. Aside from physically breaking the intergranular oxide, the role of applied tensile stress is to enhance intergranular oxidation at low temperatures.

It has been suggested that high dislocation densities generated during low temperature deformation act to enhance transport along grain boundaries. Movement of dislocations along grain boundaries also provides a means to lower the barrier to oxide formation by sweeping material to or from the grain boundaries. Normally the volumetric expansion required to form intergranular oxides at higher temperatures is accommodated by matrix diffusion. Also, stresses generated by the formation of an internal or intergranular oxide are relieved by matrix diffusion. [73] At lower temperatures matrix diffusion is less effective, and without an applied tensile stress there is a large volumetric expansion barrier to the nucleation of intergranular oxide precipitates. In their study of Ni-Al alloys, Stott, et. al., and Shida, et. al., have found that intergranular oxidation is facilitated by the stresses developed when surface and internal oxides form. [71, 72] This effect was most prominent at low temperatures (below 800°C), which the authors ascribed to the lesser extent of stress relief at lower temperature. The effect of an imposed tensile stress is to

accelerate the rate of intergranular oxidation by helping to create space to accommodate oxide formation. [73] Mino, et al., found that intergranular oxidation was enhanced under an applied tensile stress at 800 and 900°C. [74]

PROCEDURES

The effect of heat treatment atmosphere on intergranular cracking in alloy 908 was examined using controlled atmosphere notched stress-rupture tests. [14] Normally utilized to establish the stress limits to be designed into components operating at high temperatures, this test method is also an indicator of a material's sensitivity to environmental damage in combination with stress concentrations.

Stress-rupture tests usually run 1 to 1000 hours, allowing a full characterization of stress verses time to failure (rupture) in a shorter time span, as opposed to 1000 to 10,000 hours in creep tests. By design, stress-rupture tests focus on the time to failure. By using a time-temperature parameter that correlates time, temperature, and stress, stress rupture data can be extrapolated to long times (decades).

The effect of modification of surface residual stresses on stress accelerated grain boundary oxidation were examined using constant strain, C-ring tests. [14] After surface modification the samples were heat treated under known stress accelerated grain boundary oxidation conditions.

Material

The primary material used in this program was obtained in the form of 3.43 mm thick sheet (heat Y9401K) from INCO Alloys International Inc., Huntington, West Virginia. The material chemistry is given in Table 1. The processing history started with an electroslag remelted ingot 305 mm x 864 mm x length. The ingot was then hot rolled at 1121°C to 7.6 mm x 737 mm x length, followed by annealing at 954°C in a continuous anneal and pickling (CAP) line. This annealed form was then cold rolled to 3.43 mm x 737 mm x length and annealed in the CAP line at 982°C. This heat, with the addition of a final cold rolling step to obtain 5% cold-work, is the same as that used for air stress-rupture tests performed at INCO. [75]

The material used for the double notch round bar stress-rupture tests in this study had a different history and was obtained from heat Y9210 (chemistry given in Table 1). The processing steps followed for this material were vacuum induction melt, homogenize at 1191°C for 16 hours and fast cool. A series of forging and reheat steps produced

approximately 25.4 mm thick plates that were mill annealed at 980°C for 1 hour. The final processing step involved the cold rolling of strips cut from the plates to obtain 10 and 20% cold work. [11] The 20% cold work material was the same as that used by Nicol in his air stress rupture tests. [11]

Table 1. Compositions of Alloy 908 Used for Stress Rupture Testing.

Heat	Composition (weight percent)												
	Ni	Fe	Cr	Nb	Ti	Al	Si	Mn	C	Co	Mo	P	S
Y9401K	49.3	40.8	3.99	3.04	1.55	1.01	0.16	0.05	0.01	0.01	0.01	0.004	0.001
Y9210	49.5	40.9	3.86	2.99	1.57	0.97	0.13	0.04	0.01	—	—	—	0.001
HV5107	48.7	40.8	4.12	3.04	1.54	1.10	0.17	0.09	0.01	0.01	0.001	0.002	0.002

Additional double notch round bar samples were manufactured from heat HV5107 that started as a 21 kg vacuum induction melt ingot produced by INCO, chemistry given in Table 1. [1] The ingot was homogenized at 1191°C for 16 hours, fast cooled, and then forged at 1191°C to plate 31 mm thick by 102 mm wide by 1170 mm long. The material was then annealed at 980°C for 1 hour and air cooled. Cold rolling introduced approximately 20% cold work.

Heat Y9401K had a starting grain diameter of 13 μm . The grain orientation and morphology of the starting material are shown in Figures 5a and 5b. After stress rupture testing at 650°C, the grain diameters in several samples were measured and an average value of 14.5 μm was calculated. Vacuum heat treatment at 650°C for 200 hours prior to testing did not contribute to further grain growth, as shown in Figure 6a. The grain diameter for this condition, 14.2 μm , is essentially the same as that of the other tested stress rupture samples. The 20% cold work material, heat HV5107, that was vacuum heat treated at 650°C for 200 hours, has a duplex grain size. The small size grains that form the predominant volume fraction, have a diameter of 25.2 μm . The large grains in this material are essentially equiaxed, have a diameter of 200 μm , and show no texturing with rolling direction, as shown in Figure 6b.

The 20% cold work material, heat Y9210, also has a duplex size distribution. In this material, however, the large grains were extremely elongated and oriented with the cold rolling direction. [11] The small size fraction had a grain diameter of 15.8 μm . The large

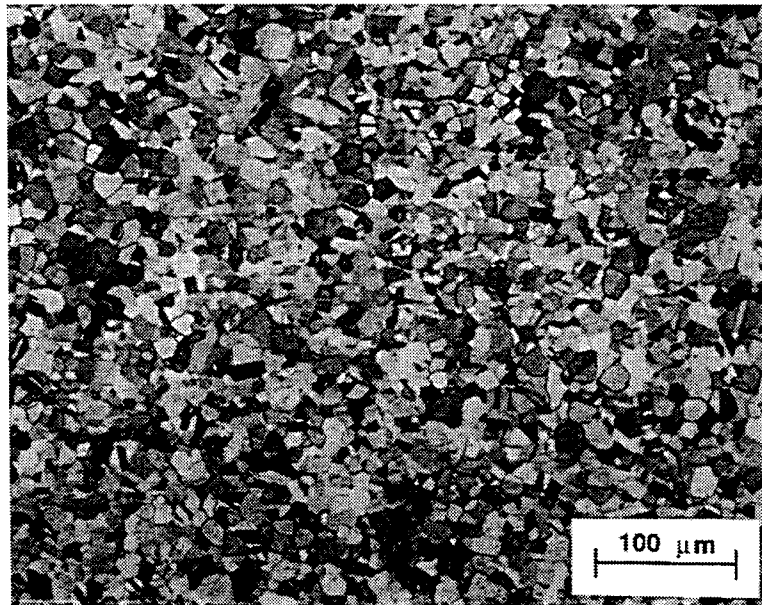
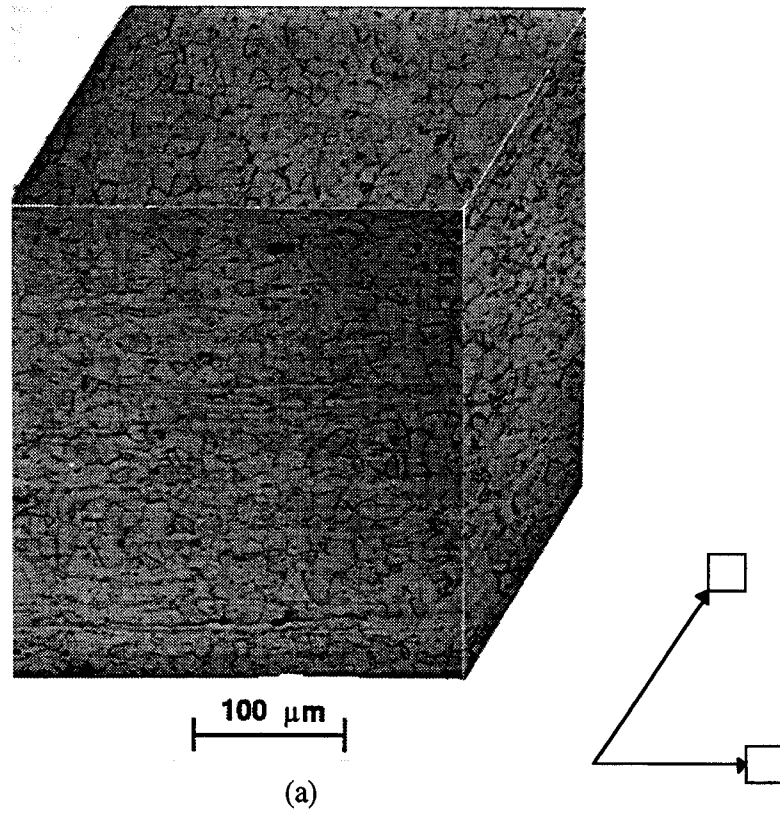


Figure 5. (a) Grain size and orientation of 3.43 mm thick sheet starting material, heat Y9401K, used for the flat plate stress rupture test samples, grain diameter 13 μm , Hardness 266 HVN. (b) Grain size in tested stress rupture sample (650°C/118 hours) grain diameter 14.8 μm , hardness 484 HVN.

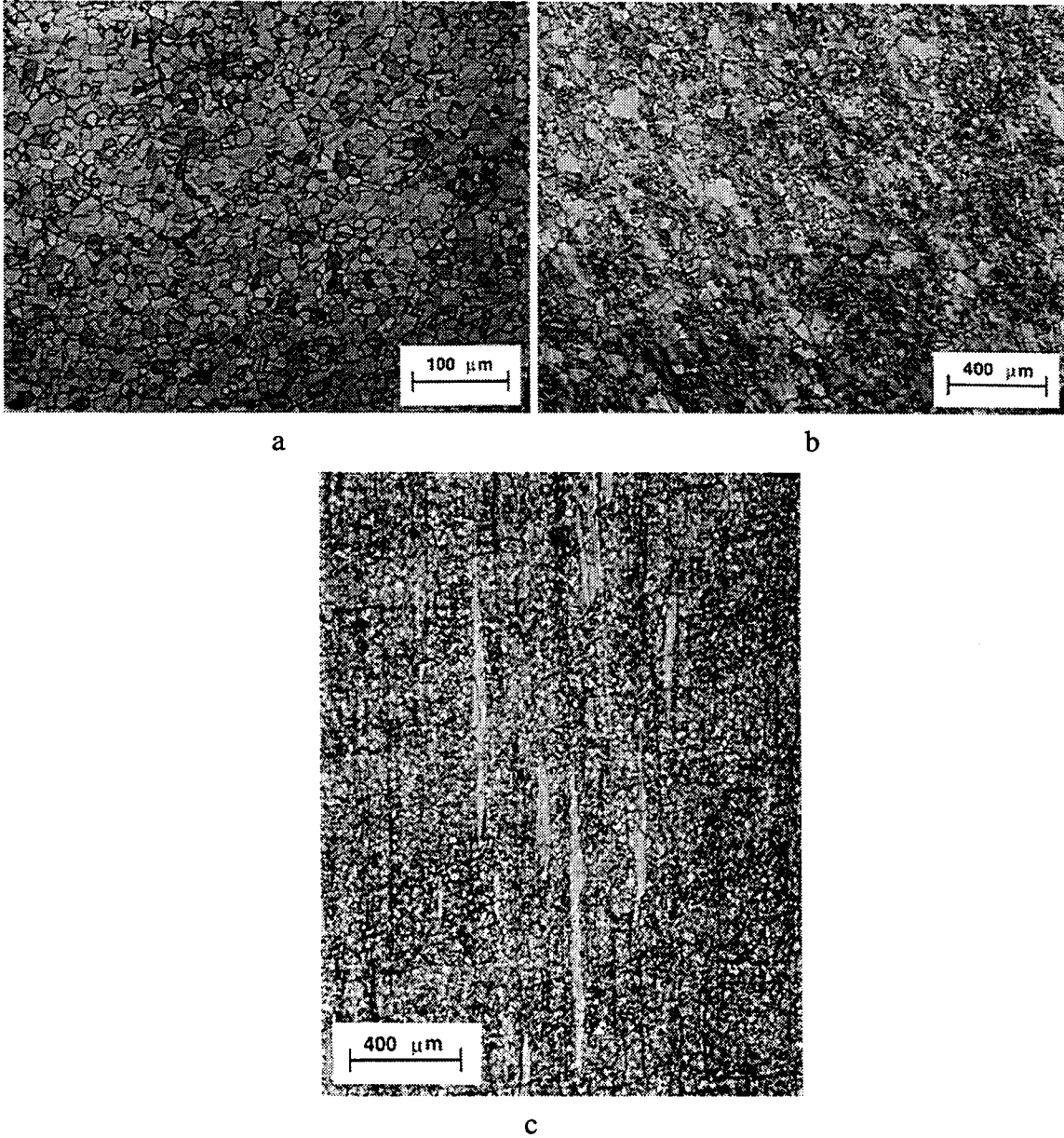


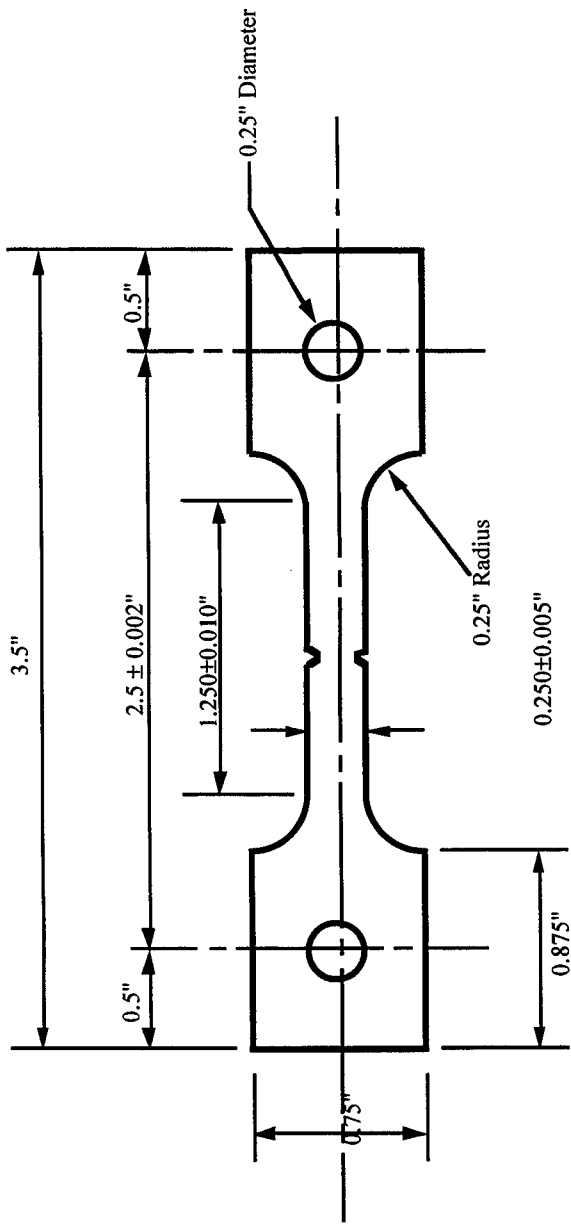
Figure 6. (a) (b) Optical micrographs showing grain size in the flat plate sample (14.2 μm diameter), and round bar (25.2 μm diameter) sample, respectively, that had been vacuum heat treated at 650°C for 200 hours. (c), optical micrograph of elongated grains in 20% cold worked material, heat Y9210.

elongated grains were acicular in shape and had a grain length, based on the c-axis of the grain, of 534 μm , the a-axis was of the same dimensions as that of the surrounding small equiaxed grains. The micrograph shown in Figures 6c, illustrates the elongated grains present in this material heat. The microhardness within any elongated grain was the same as that of the surrounding matrix. An etched metallographic sample of this material was heat treated at 650°C for 200 hours in a 1×10^{-6} Torr vacuum. This procedure was used to determine if the grains were unrecrystallized grains that had been elongated during the cold rolling operation and whether recrystallization would occur during stress rupture testing at 650°C. The elongated grain did not recrystallize during heat treatment. As a microstructural feature these grains will, therefore, not change during stress rupture testing at 650°C.

Stress Rupture Test Procedure

The primary sample type used for argon atmosphere testing was a flat plate (3.15 mm thick) double-edge-notch design, for subsize sheet materials. The specimen geometry was chosen to closely replicate thin wall (< 3 mm) conduit designs. The notch produces an elastic stress-concentration factor (K_t) at the root of the notch of 4.5. A drawing of the specimen design is shown in Figure 7. The samples were machined so that their tensile axes were parallel with the longitudinal direction, with crack growth in the transverse direction, LT orientation. The other sample type utilized is a double-notch-round-bar sample that incorporates the British standard V-notch with a $K_t = 4.1$. [76] This sample design is shown in Figure 8. To study the effect of heat treatment on stress rupture properties, several samples from both designs were heat treated in a 10^{-5} Torr vacuum at 650°C for 200 hours.

The test methodology followed ASTM E292-83 which provides a standard method for conducting time to rupture tensile tests for notched materials. [77] The stress rupture test matrix is shown in Table 2. The matrix was established first around stresses that would neither produce rapid tensile failure nor a stress rupture life in excess of 500 hours, dependent upon sample geometry. Using these stresses, the oxygen concentration and temperature were varied. An Applied Test Systems (ATS) lever arm test frame with auto load leveling and auto loading was used. The system incorporates an Inconel alloy 713 retort that serves as the environmental chamber. The retort is surrounded by a tubular, three zone, electric-resistance furnace with a programmable controller.



1. Low Stress grind gage section.
2. Holes must be on centerline of reduced section within ± 0.002 ".
3. Notches to be centered in gage within ± 0.002 inches.
4. Notches are 0.0375 ± 0.001 " deep.
5. Notch root radius 0.006 ± 0.0005 ".
6. Remove all burrs and sharp edges.
7. Blank dimensions width not less than 0.750".

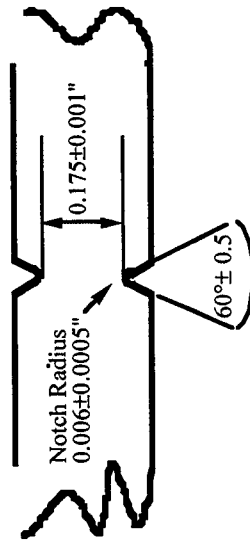


Figure 7 . Double edge notch stress rupture specimen, $K_t = 4.5$.

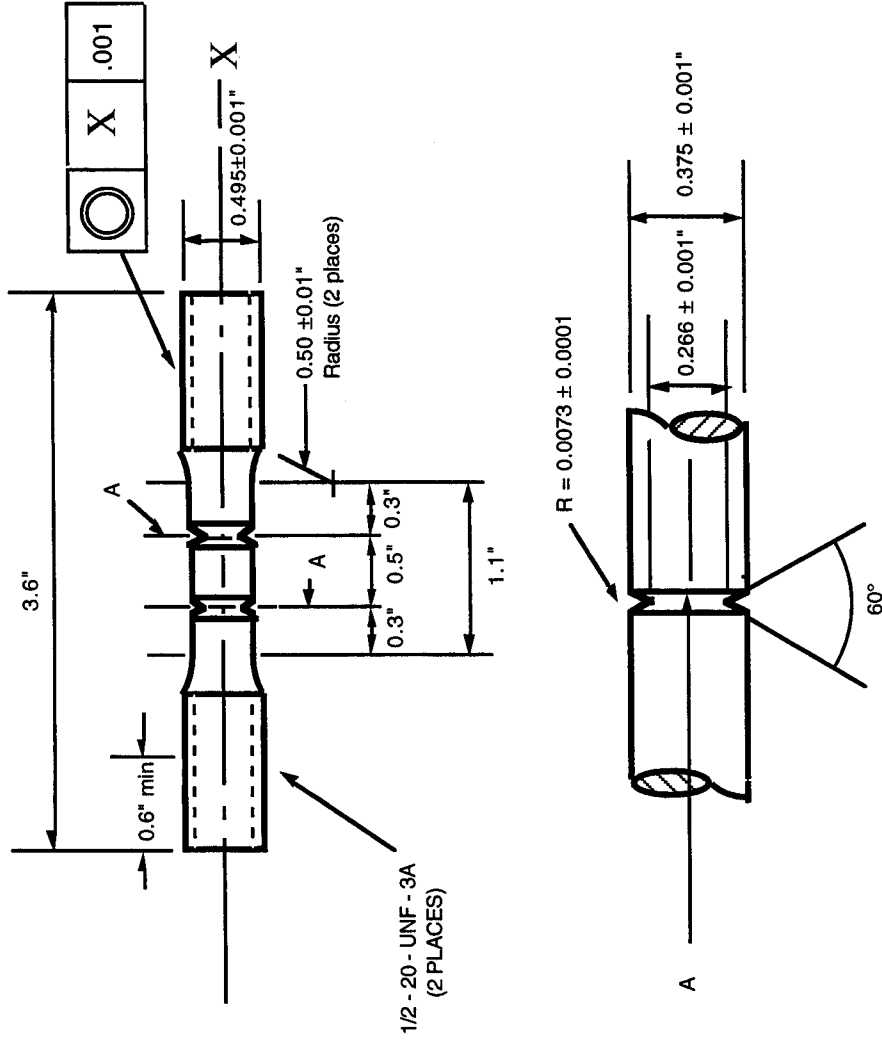


Figure 8. Double notch round bar stress rupture specimen $K_t = 4.1$.

Table 2. Test Matrix Used For Stress Rupture Tests. FP = Flat Plate Specimen(s), RB = Round Bar Specimen(s).

Temperature (°C)	Stress (MPa)				Oxygen (ppm)
	450	550	650	700	
550			√ FP		0.5 - 1
650			√ FP	√ FP	< 0.5
		√ FP	√ FP		0.5 - 1
			√ FP		3 - 6
			√ FP		33 - 53
			√ FP		195
	√ RB/FP		√ RB/FP		1000
700		√ FP	√ FP		0.5 - 1
					195
750	√ FP	√ FP	√ FP		195

Both oxygen and water vapor analyzers were used. A Delta F Corporation electrochemical process oxygen analyzer was used to measure oxygen concentration in gas sampled from the notch region of the test sample. As configured, the analyzer has a detection range of 0.01 to 50 ppm oxygen. This range was selected for sensitivity at low oxygen concentrations. The oxygen concentration in the testing retort was continuously measured by passing the exit gas through the analyzer at a flow rate of $5.66 \times 10^{-2} \text{ m}^3/\text{h}$ with an at gage delivery pressure of 129 Torr. The concentration of water vapor was measured with an EG&G analyzer that utilizes a phosphorus pentoxide electrochemical sensor.

Proper positioning of the two detectors with respect to one another is important. Arrangement in series on the exit gas posed a problem because the oxygen analyzer uses an aqueous electrochemical cell that produces a wet exit gas. Additionally, the water vapor analyzer produces oxygen as a byproduct of its electrochemical reaction. A parallel arrangement on the exit gas line was also ruled out since the oxygen analyzer requires a tight, no leaks, supply to maintain a constant oxygen reading with fluctuations of $\pm 2.8 \times 10^{-2} \text{ m}^3/\text{h}$ in the analyzer gas flow rate. Based on these considerations, the water vapor analyzer was placed in the supply gas line to the retort. This placement was acceptable since water vapor in the supply gas was being measured but not controlled for these tests, and in all cases the water vapor concentration of the supply gas remained constant throughout the test.

The argon gas was supplied to the retort using a high purity two-stage regulator. Either commercial argon gas of different grades or analyzed oxygen-argon mixtures were used to obtain the required oxygen concentration. Each new gas cylinder was sampled for oxygen and water vapor prior to testing. For low oxygen concentration tests (≤ 50 ppm), the standard procedure employed to attain a constant oxygen concentration was to continuously flow supply gas through the retort and supply lines at a 129 Torr regulator gage pressure until the oxygen concentration of the retort exit gas matched the initial cylinder reading. The time required to achieve this depended upon how long the retort and sample load train were exposed to atmosphere. To minimize contamination of other parts of the system, the supply and exit lines were kept shut and under argon during sample loading and cylinder changes. For high oxygen concentration tests (≥ 50 ppm) using pre-analyzed argon-oxygen mixtures, the retort was first purged with inexpensive 99.997 grade argon until the oxygen concentration from the retort matched that of the cylinder. The analyzed mixed gas was then introduced into retort for 30 minutes prior to testing. During the initial heatup of the retort and sample the oxygen concentration generally increased for the first several minutes as trapped oxygen and organics were baked out, but returned to the initial supply gas reading rapidly after that. Initial tests with low oxygen concentrations (<1.0 ppm) showed that the new retort could significantly get oxygen down to 0.01 ppm levels. This necessitated that the oxygen analyzer be placed on the exit gas side.

The samples were cooled in the retort under flowing argon at the completion of each test. This prevented the fresh fracture surfaces from oxidizing. Every sample was examined using scanning electron microscopy (SEM) to establish failure mode and fracture morphology. In the case of the flat plate samples, SEM fractography was performed on one half of the fracture, the other was prepared for metallographic examination. Fractography of the round bar samples was done using SEM on one half of the failed notch, and the unfailed notch was prepared for metallographic examination. Metallographic sections for both sample types were made so that the view was of the plane parallel to the tensile axis. Samples for SEM and energy dispersive x-ray spectroscopy analysis (EDS) were prepared by diamond grinding to 20 μm followed by polishing with diamond suspensions down to a final 3 μm polish. To prevent charging near the mounting resin and at oxides, all the SEM samples were coated by vacuum evaporation of carbon. Samples used for grain size determination were immersed for 30 to 60 seconds in an etchant composed of 15 ml hydrochloric acid, 10 ml acetic acid, 10 ml nitric acid, and 6 drops glycerin.

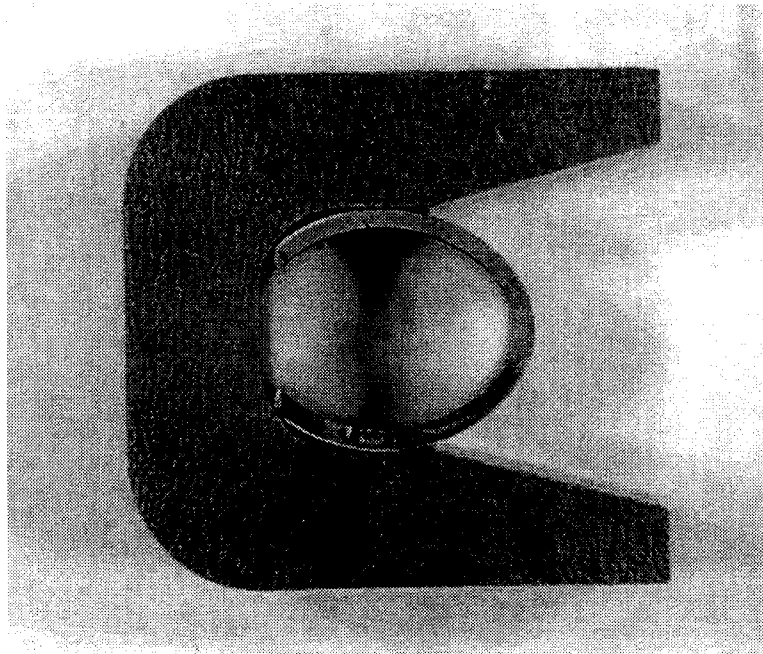
A TOPCON ABT-150 scanning electron microscope equipped with a LaB₆ filament was used for the fractographic, microstructural, and chemical analyses. The ABT-150 is linked with a Noran Pioneer energy dispersive x-ray detector capable of light element detection. Semiquantitative analyses of collected spectra were performed using a Noran Voyager x-ray analyzer and software. Unless otherwise specified, spectra were collected at 15 kV and at a 17 mm working distance. The microscope was operated to give an approximate spot size of between 0.1 and 0.05 μm. [78]

Area measurements on fracture surfaces were performed from SEM micrographs with fractographic features manually traced into a Zeiss image analysis system. Grain diameter measurements were done in a similar fashion.

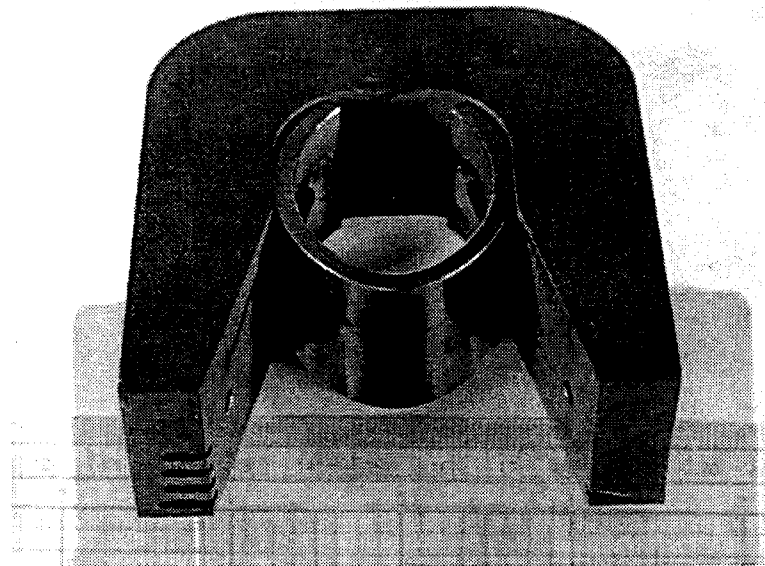
C-Ring Residual Stress Modification Study

A parallel study on the modification of residual stresses was performed. C-ring test samples manufactured from tubing were used. The material had been solution annealed at 980°C for 1 hour in a hydrogen furnace that left it in a bright condition, i.e., it was free of any surface scale or subsurface oxidation. The tube had a radius of 23 mm and a wall thickness of 3 mm. The grain diameter of the starting material was 73 μm. Samples were placed in test fixtures designed to produce $6.0 \pm 0.08\%$ plastic strain at the outer surface of the C-ring. [79] The test fixtures were machined from alloy 908 to eliminate strain relief due to differential thermal expansion between the C-ring and fixture. Macrographs of a test fixture with a C-ring in place are shown in Figures 9a and 9b.

The test samples were divided into three groups; solution annealed (starting condition), stress relieved, and shot peened. The stress relief treatment consisted of heat treating the C-rings, in their test fixtures, in a 1×10^{-6} Torr vacuum at 650°C for 16 hours. The shot peened test samples were first mounted in their fixtures. The samples were then commercially shot peened using 230 mesh (maximum 63 μm diameter) steel shot with 100% coverage of the exposed outer surface of the C-ring obtained. The test environment used to evaluate the samples consisted of a vacuum furnace with a degraded vacuum of 3×10^{-2} to 4×10^{-2} Torr (approximately 11- 8 ppm oxygen), measured by thermocouple gage. Sets, composed of one of each type were heat treated together. Heat treatment cycles were based on inspections for cracking that occurred after exposure intervals of 24, 70, and 200 hours at 650°C.



a



b

Figure 9. (a),(b) C-ring specimen holder designed to maintain a constant plastic strain of 6% during heat treatment.

RESULTS

Stress Rupture

In Figure 10, the stress-rupture data are plotted to show the time to rupture versus stress for all the 650°C solution annealed samples tested in low/controlled O₂ in argon atmospheres. The argon atmosphere data have been grouped by oxygen concentration range for the flat plate samples to maintain plot clarity. These data are compared with air data generated at INCO Alloys International, Huntington, West Virginia for the same material heat but with 5% cold work applied before testing. The shift to increased rupture time for the low O₂ samples compared with the air data is immediately evident. Also evident is the grouping of failed, solution annealed low O₂ samples for stresses in the 651 ± 18 MPa range. The time to rupture in this stress range was approximately 108 ± 36 hours and independent of oxygen concentration. The sample group for the 540 MPa stress range was insufficient (1 sample failed at 452.5 hours) to establish whether this independence of rupture time on oxygen concentration held at lower stresses.

Test results for the round bar material tested at 650°C in low/controlled O₂ in argon atmospheres are compared in Figure 11 with air data obtained for the same material heat by Nicol. [11] This plot shows several trends for this material and sample geometry. There is a significant increase in rupture life with decreasing oxygen concentration. When compared with flat plate sample results, the effect of oxygen concentration on rupture life for the round bar samples is more pronounced, with better time to rupture separation for the 1000, 44, and 3 ppm O₂ samples. The effect of prior processing is also evident in this plot, with the solution annealed sample showing an extended life at 1000 ppm oxygen over the 20% cold work samples. No difference in behavior was observed for the 10% cold work sample tested at 1000 ppm oxygen and 469 MPa, and its time to rupture was within the range of the 20% cold worked samples tested under the same conditions.

Alloy 908 stress rupture data show that the rupture times for the flat plate samples were relatively independent of oxygen concentration for low (≤1000 ppm) concentrations. The variation in rupture time with stress, however, was consistent with expected stress rupture behavior. Double notch round bar data shown in Figure 11 indicated that the rupture times for this sample geometry, with 20% cold work, are more sensitive to oxygen concentration. The long test time, without rupture, seen in the 3 ppm oxygen test for this sample geometry precluded running additional tests to determine if this trend continued at lower (≤3 ppm) oxygen concentrations.

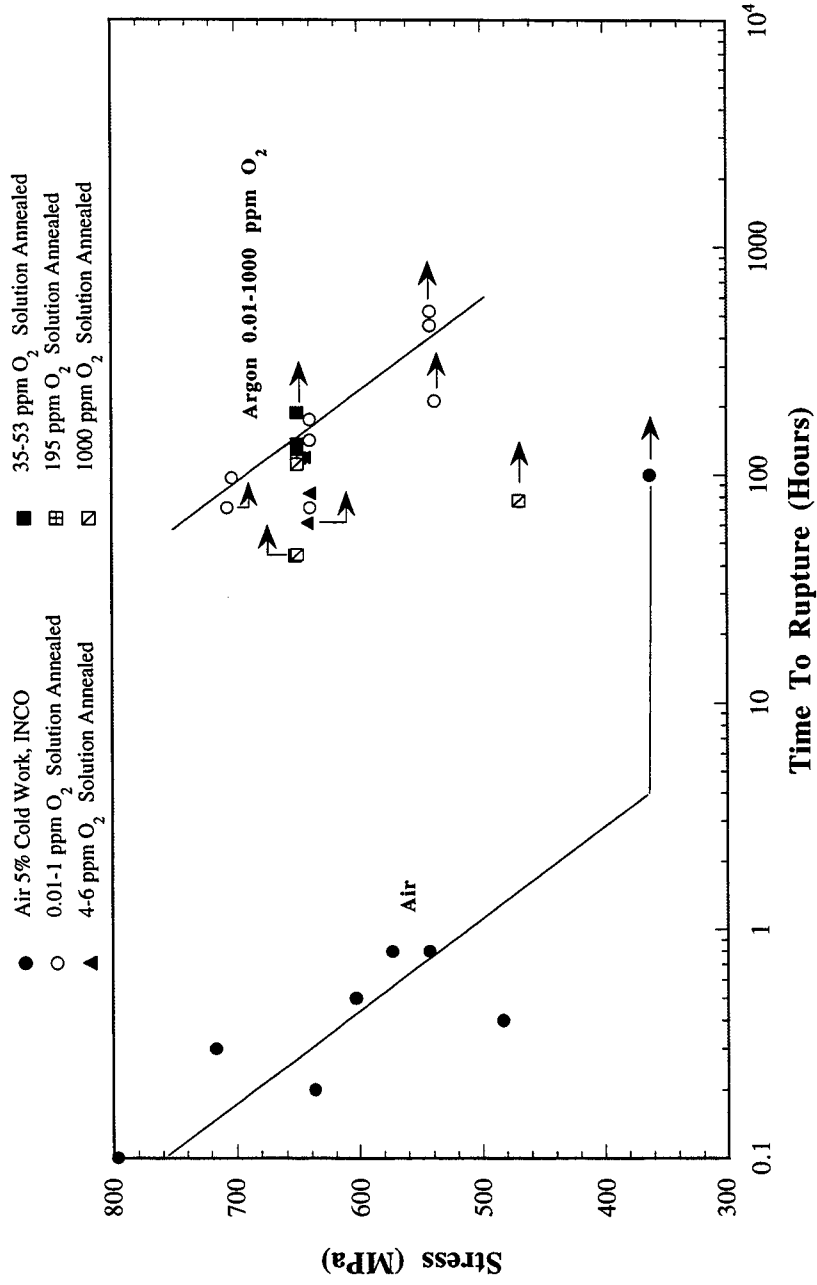


Figure 10. Comparison of 650°C flat plate test sample stress rupture data for alloy 908 in argon with controlled oxygen concentration and the same heat treat of material but with 5% cold work and tested in air by INCO. [75] Arrows indicate specimens that did not fail, test stopped.

Prior vacuum heat treatment resulted in no substantial change in rupture life for either of the sample geometries. The round bar samples, under identical conditions, ruptured within a short time of each other. The effect of prior vacuum heat treatment on time to rupture is shown in Figure 12.

Effect of Oxygen Concentration

Optical and scanning electron fractography of failed and interrupted flat plate samples extended the picture of the influence of oxygen concentration on stress rupture test results. The relationship between oxygen concentration and percent intergranular fracture was first examined for the flat plate test data that formed the bulk of the testing. Failed samples were characterized by two or three distinct fracture morphologies, dependent upon oxygen concentration. Figure 13 illustrates the changes seen in fracture morphology with oxygen concentration. Starting at the bottom figure, with no intergranular fracture originating at the notches, and moving up, with increasing oxygen concentration, the planar intergranular fracture region is seen to penetrate further into the sample from the notches. No evidence of ductility is observed on the intergranular fracture surfaces. The second fracture morphology in this illustration, is the V-shaped region extending into the sample from each notch. These regions are ductile with relatively large microvoids developed by creep cavitation. [80] Creep at the test temperatures employed in this study is possible in alloy 908 given that its' homologous temperature, T_h , at 650°C is 0.56 and 0.5 at 544°C. As illustrated, the V-shaped regions become smaller as the intergranular crack front progresses further into the sample. The semicircular areas in between are the shear lips that formed at final fracture. This illustration shows an increase in the pinned or brittle regions at the notches as the oxygen concentration is increased and a corresponding decrease in the shear lip areas. This observation is consistent with a decreasing percentage of shear lip area corresponding to increasingly brittle behavior. [81] In this case, the percentage of intergranular fracture increases with increasing oxygen concentration.

Micrographs which show the fracture features as a function of oxygen concentration are shown in Figures 14a, 14b, 14c and 14d. For these samples, intergranular cracking proceeds along a flat front that extends in from the notch. Intergranular cracking from the sides was observed, but only in very limited areas and at shallow penetrations (1-10 grains deep) in samples tested at higher oxygen concentration. The "smooth" concave areas in the region between the notches are the shear lips. The shear lips, have a smooth/ductile fracture appearance, and represent the predominant source of reduction in area observed in these samples. The crack paths along the shear lips are oriented 45° with respect to the

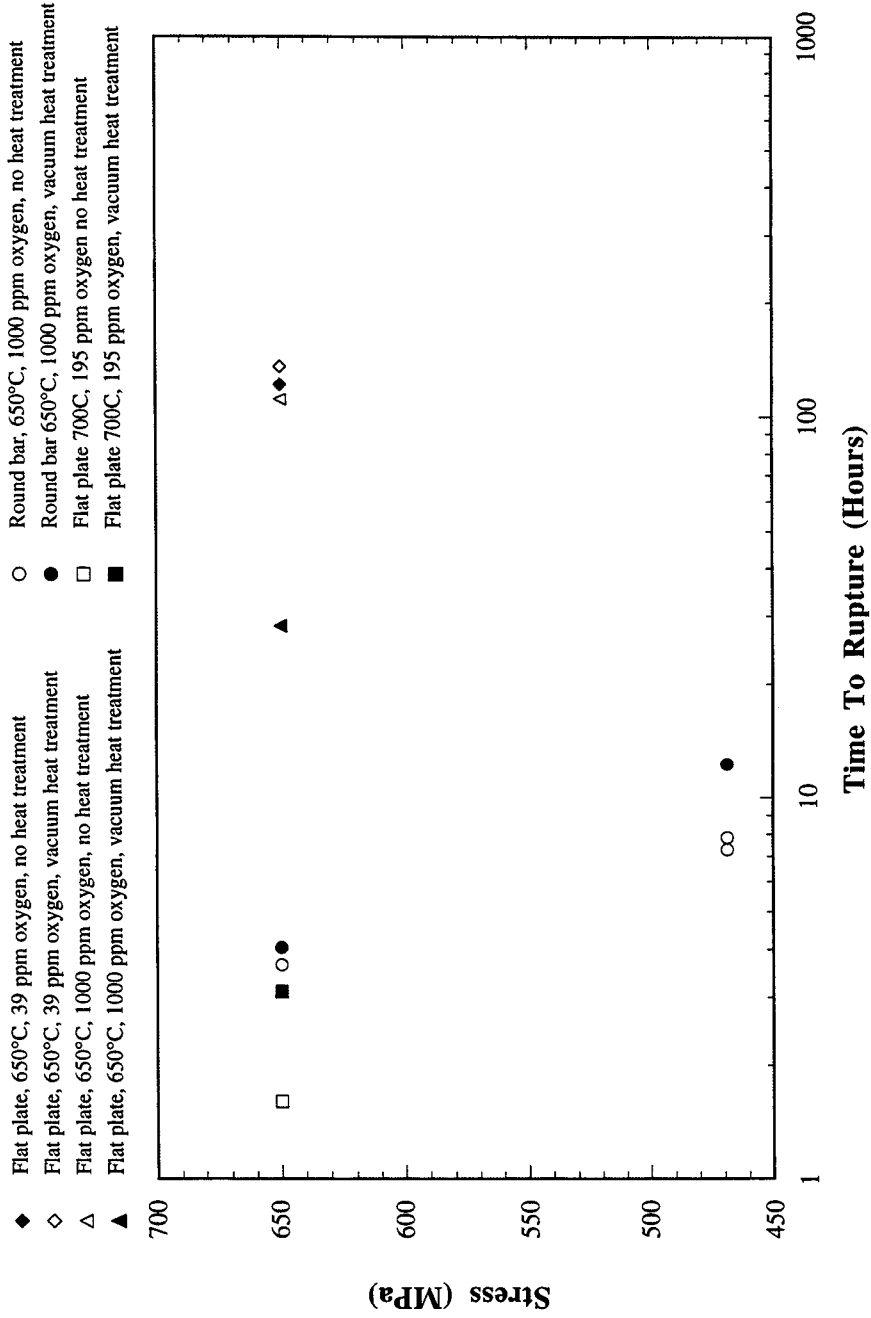


Figure 12. Comparison of time to rupture versus stress for vacuum (1×10^{-5} Torr) heat treated (650°C / 200 hours) then tested samples with samples tested in their as received condition. As received conditions, flat plate solution annealed and round bar 20% cold work.

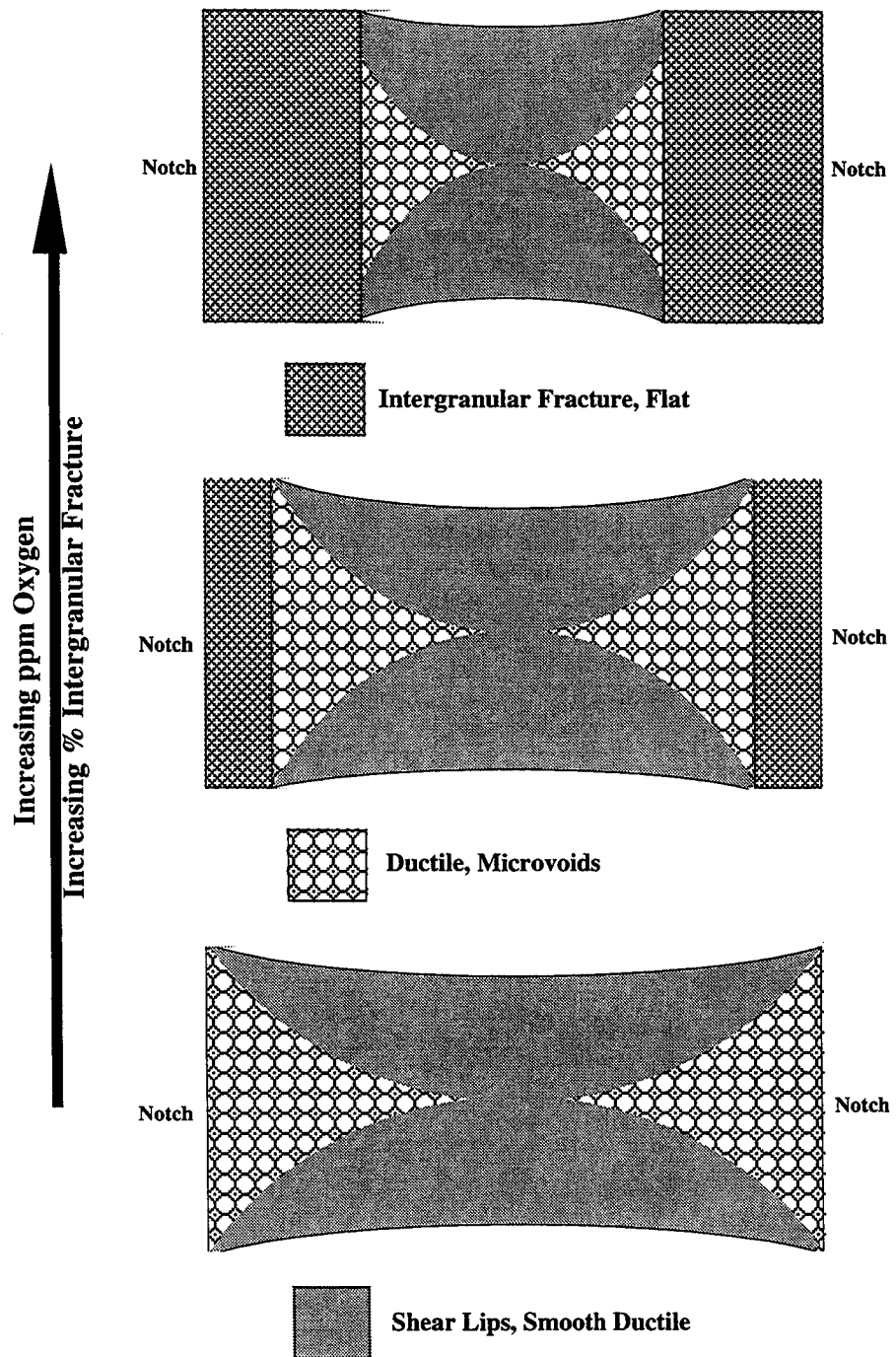
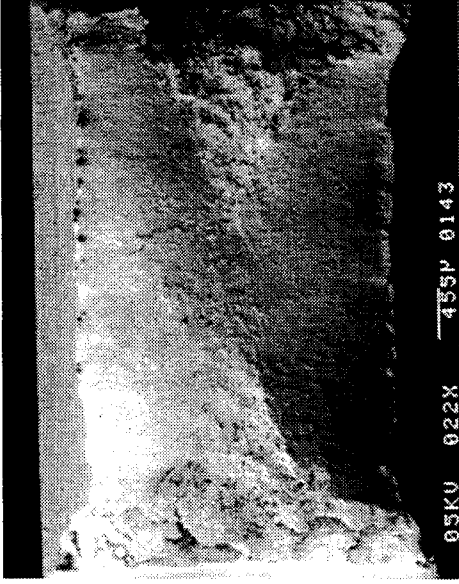
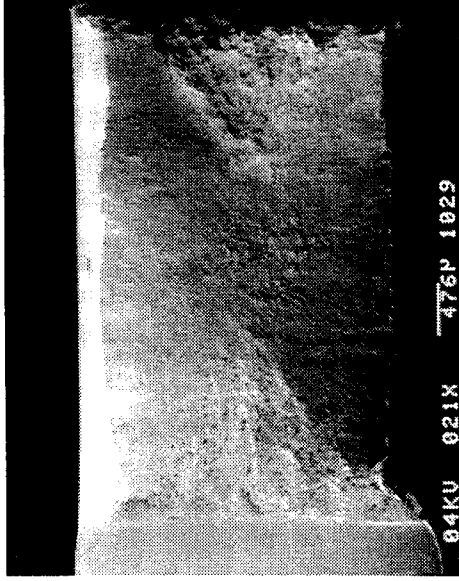


Figure 13. Characteristics of flat plate stress rupture fracture surfaces as a function of oxygen concentration.



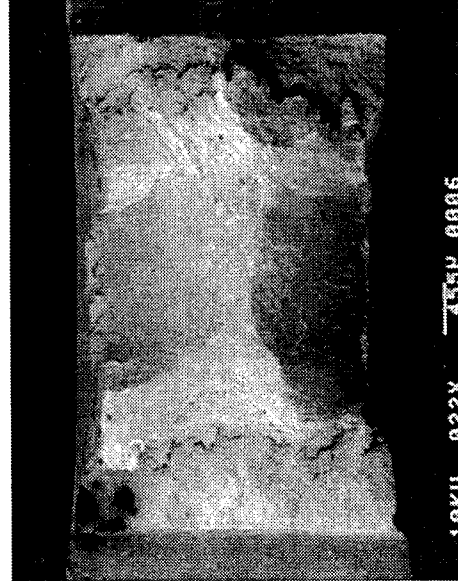
(a) 1 ppm O₂, 8% Intergranular fracture



(b) 6 ppm O₂, 23% Intergranular fracture



(c) 38 ppm O₂, 40.4% Intergranular fracture



(d) 1000 ppm O₂, 58.5% Intergranular fracture

Figure 14. SEM micrographs comparing the intergranular fracture morphology in 650°C/650MPa samples as a function of oxygen concentration (a) 71.7h to failure, 1 ppm O₂, (b) 82.3h to failure, 6 ppm O₂, (c) 122h to failure, 38 ppm O₂, (d) 111.4h to failure, 1000 ppm O₂.

tensile axis. The length of the flat crack front corresponds to the depth of intergranular cracking, beyond which the crack path changes orientation and morphology to smooth/ductile along the shear lips. Based on fracture morphology, a plane stress condition exists for the flat plate samples examined in this study. An approximation of the plastic zone size for the flat plate samples was obtained from microhardness measurements in the vicinity of the notches of failed samples. The large plastic zone, relative to sample thickness ($r_p \geq t$), confirms that these samples were under plane stress conditions during testing and is consistent with the fractographic evidence.

The effect of test temperature, oxygen concentration, and stress for the flat plate samples can be seen in Figure 15. From this plot a general trend of increasing rupture life with decreasing test temperature can be seen and is expected. The mechanical properties of the material decrease and the creep rate increases with increased temperature. [82, 83] The SEM micrographs shown in Figures 16a, 16b, and 16c illustrate the morphology of fracture as a function of test temperature. As the temperature is increased, the rupture time and percent intergranular fracture decrease while the reduction in area increases. Morphologically, the fracture surfaces show more ductile area than the lower temperature samples at similar oxygen concentrations, but with typically shorter rupture lives. This is due to two factors. First, there is an increase in creep rate with increasing temperature. Second, the strength of the material decreases with increasing temperature. [20, 23, 24, 80] These factors are apparent when comparing the times to rupture for the 750°C/650 MPa, 700°C/650MPa, and 650°C/650 MPa tests in 195 ppm oxygen and the corresponding SEM fractographs shown in Figures 16a, 16b, and 16c, respectively.

There was no correspondence between time to failure and increasing percent intergranular fracture. Nor was a trend observed between time to rupture and oxygen concentration. A definite correlation between oxygen concentration and percent intergranular fracture was, however, observed. The data shown in Figure 17 are from flat plate stress rupture tests performed at 650°C and in the stress range 651 ± 18 MPa and at different oxygen concentrations. As can be seen in this figure, the percent intergranular fracture increases as the oxygen concentration or partial pressure increases. Figure 18 shows a plot for all sample types (flat plate and round bar), in four starting conditions: solution annealed, 20% cold work, and either solution annealed or cold worked with the addition of a vacuum (1×10^{-5} Torr) heat treatment of 200 hours at 650°C. As can be seen in this figure, the curve develops a sigmoidal shape, with a low ppm oxygen transition at between 1 and 0.1 ppm oxygen, and a similar plateau as the oxygen concentration approaches that of air (760 Torr). This data is compared with the 650°C slow strain rate

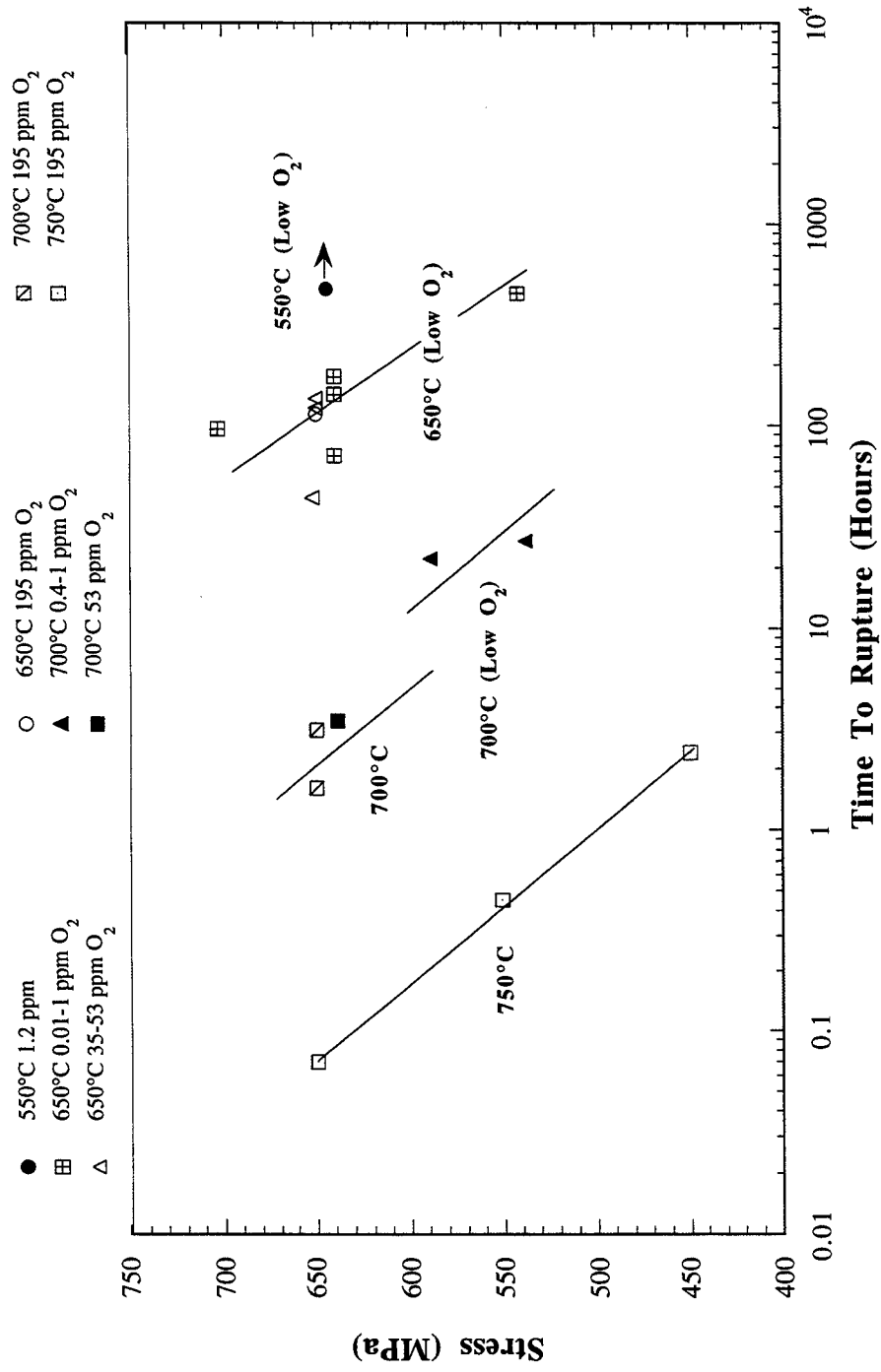
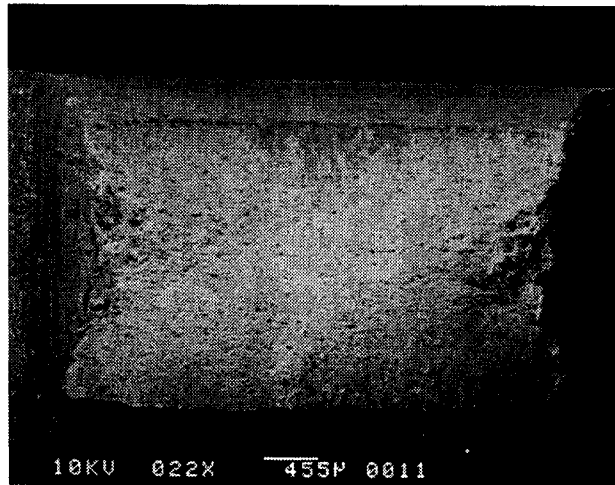
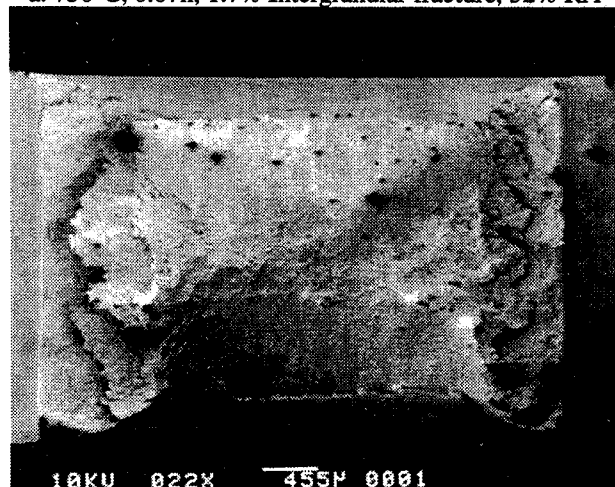


Figure 15. Effect of temperature on time to rupture versus stress for solution annealed flat plate samples at 750, 700 and 550°C for different ranges of oxygen concentration.



a. 750°C, 0.07h, 1.7% Intergranular fracture, 32% RA



b. 700°C, 1.6h, 40% Intergranular fracture, 24.6% RA



c. 650°C, 114.2h, 47.8% Intergranular fracture, 5.1% RA

Figure 16. SEM micrographs showing the effect of temperature on fracture morphology for a stress of 650 MPa and 195 ppm O₂. (a) 750°C (b) 700°C. (c) 650°C.

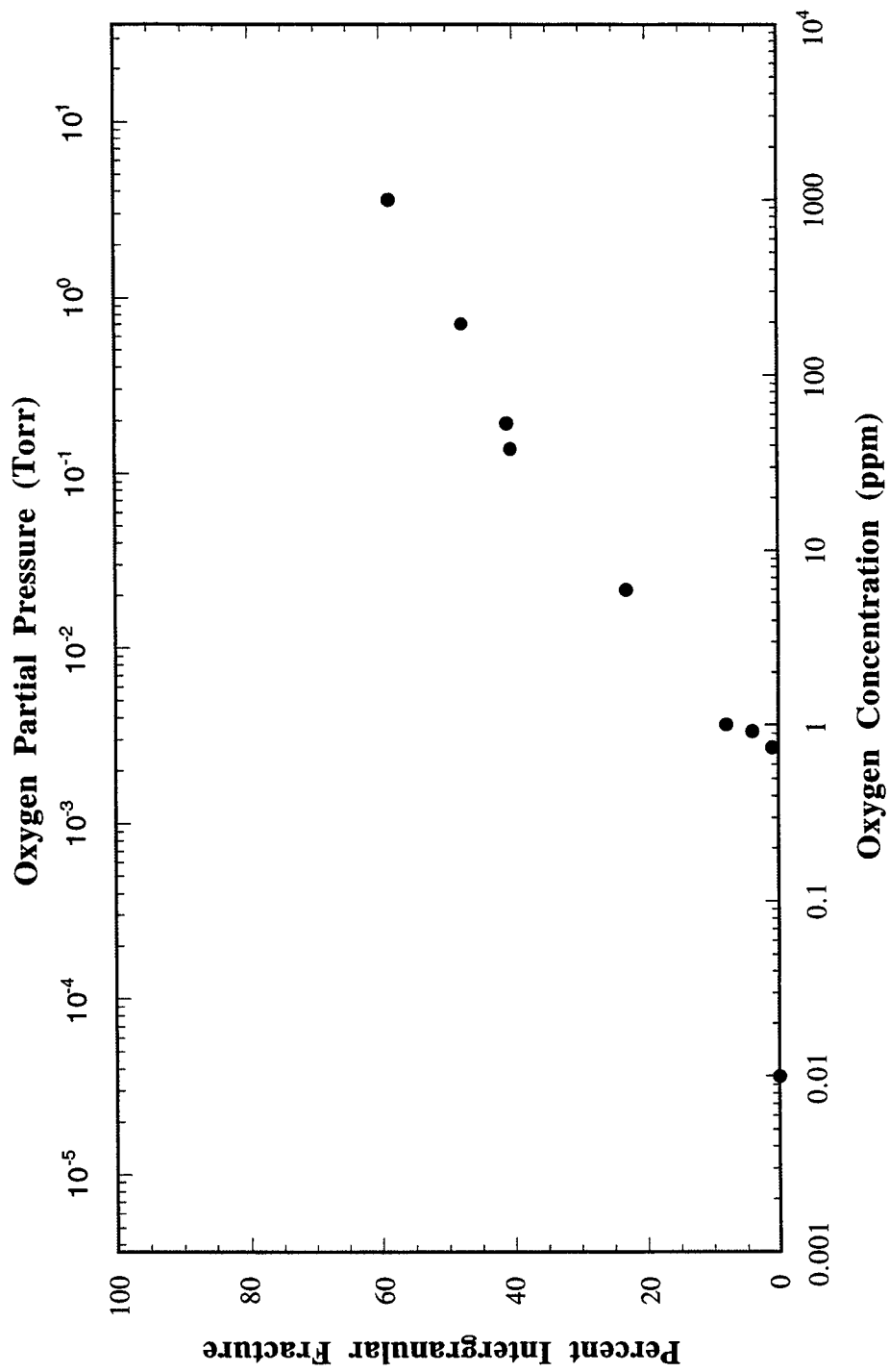


Figure 17. Percent intergranular fracture versus oxygen concentration for 650°C and 651±18 MPa stress range flat plate test samples.

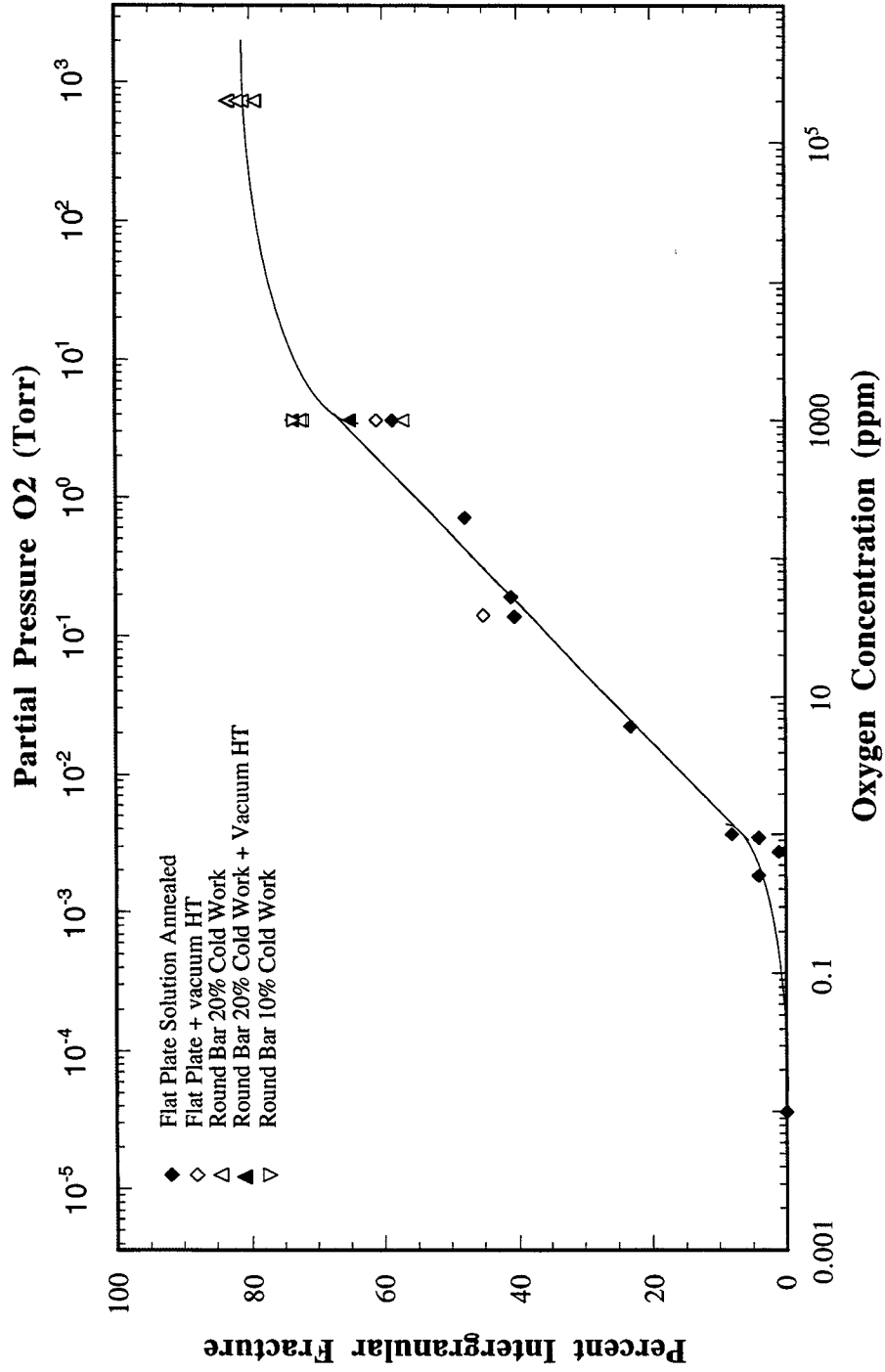


Figure 18. Percent intergranular fracture versus oxygen concentration for all samples, tested at 650°C and for all stress levels tested, range 535 ± 140 MPa.

test results from Andrieu for alloy 718 in Figure 19. [53] As can be seen from this plot, both data sets follow the same trend, with the alloy 908 stress rupture data falling on top of those for alloy 718. With respect to oxygen concentration, the curve shape and transition points seen here also follow those seen in da/dN versus oxygen partial pressure and cycles to failure versus oxygen partial pressure curves for alloy 718. [17]

Interrupted and Non-Loaded Flat Plate Tests

The intergranular fracture surfaces of all of the flat plate test specimens that ruptured had oxidized sufficiently to obscure fine microstructural details. Initially it was thought that this oxidation had occurred during the interim between failure and furnace cool down. The ductile fracture surfaces resulting from final fracture did not, however, show a detectable surface oxidation layer. There was no evidence of oxide free intergranular fracture surfaces or cracks in any of the samples examined. In order to examine how the fracture morphology and oxidation characteristics appeared prior to final fracture, a test was stopped before failure, cooled down, and then fractured in air at 22°C. The transition between intergranular and ductile transgranular fracture was very clear and abrupt in this sample. The ductile transgranular fracture that occurred at room temperature when the sample was loaded to failure was free of oxidation. The presence of oxide free intergranular fracture surfaces at the ductile/brittle interface was expected if it is assumed that intergranular fracture occurs by oxygen embrittlement. If intergranular fracture occurred at temperature during testing, however, then it should show signs of surface oxidation. All the intergranular fracture surfaces were covered with a thin oxide layer. No evidence to suggest that intergranular fracture occurs by oxygen embrittlement, prior to oxidation, was found. [14] This observation indicates that the grain boundaries ahead of the crack are not inherently embrittled by oxygen and that grain boundary oxidation is a required part of the crack growth mechanism. The lack of long range oxygen embrittlement observed in alloy 908 is consistent with that from fatigue crack growth studies in other materials. In these studies, when fatigue specimens are tested sequentially in air then in vacuum the crack growth rate drops from the high rate in air as soon as vacuum is reestablished. [18, 19, 20, 30, 84] In the fatigue crack growth situation this indicates that the crack growth rates are dependent only upon the existing environment. Also the effect is limited to the crack tip region and is not dependent upon the long range diffusion and embrittlement by oxygen of grain boundaries ahead of the crack. [30, 34]

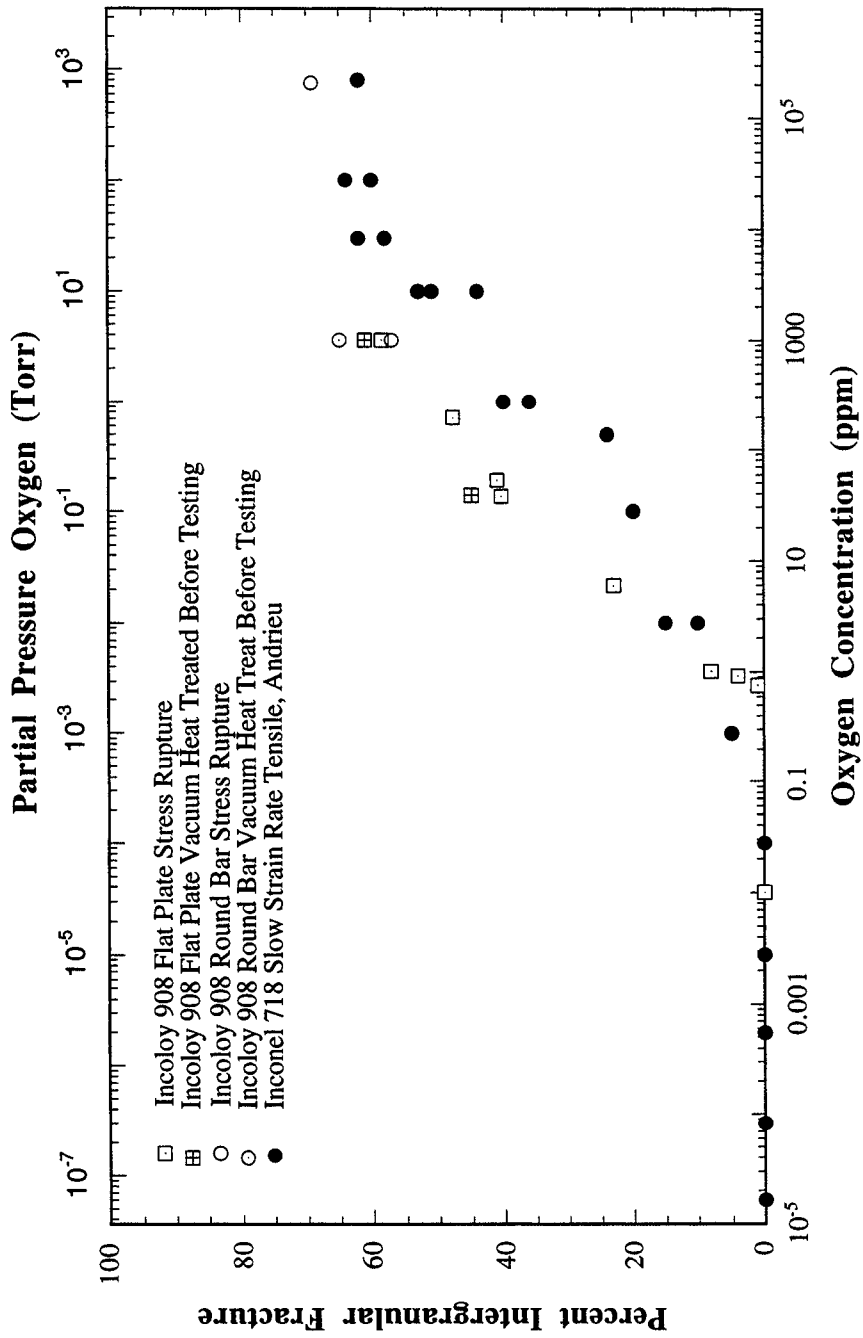


Figure 19. Comparison of 650°C Inconel 718 slow strain rate (8.3×10^{-4} mm/s) tensile data from Andrieu [53] with 650°C notched stress rupture data from alloy 908 in the 649 ± 18 MPa stress range.

A related investigation involved placing companion, not loaded, (dummy) flat plate notched test specimens in the retort with the loaded test specimens. [14] At the conclusion of the test the dummy test samples were removed from the retort and fractured in air at 22°C. This test procedure was performed at 650°C and 700°C in 1 and 0.95 ppm oxygen environments, respectively. The loaded test sample exhibited intergranular cracking extending in from the root of the notch, with no grain deformation in the intergranular fracture region. When fractured the dummy test specimens show elongation of the notch section before failure and no intergranular cracking. Similar results were obtained for the 700°C dummy sample. These results clearly indicate that the intergranular oxidation and fracture observed in this material requires a stress component and is not due solely to intergranular oxidation.

Tensile samples that were placed, unloaded, in the same environment and then tested in air showed no change in properties when compared with tensile samples heat treated in vacuum (1×10^{-5} Torr) for similar times. The solution annealed (980°C/1 hour) samples exposed in the retort at 650°C for 188 hours in 35.5 ppm oxygen, along with the stress rupture sample, showed a yield strength of 1050 ± 70 MPa, ultimate strength of 1445 ± 7 MPa, and an elongation of $17.5 \pm 0.7\%$. This compares with a yield strength of 1075 MPa, ultimate strength of 1433 MPa, and an elongation of 16.5% for solution annealed alloy 908 heat treated at 650°C for 200 hours in vacuum. [79]

Round Bar Microstructure and Fractography

To obtain an intact notch at failure for microstructural and chemical studies double notch round bar test samples were utilized. Thus, the test atmospheres used were limited to a relatively high oxygen (1000 ppm) environment to produce rapid fractures with high percentages of intergranular failure, but without the gross oxidation of the fracture surfaces that limits detailed SEM and EDS analysis of material tested in air. The grain structure of this material, consisting of elongated grains with their c-axis parallel to the rolling direction of the plate (as seen in Figure 6c), apparently had little influence on crack propagation. This is because the intergranular regions associated with these grains failed in the same manner as the equiaxed grains observed in the flat plate test samples. In the micrograph shown in Figure 20, an elongated grain can be seen at the root of the unfailed notch in a round bar sample tested at 650°C in 1000 ppm oxygen. As can be seen in this figure, the crack has started at the surface of the elongated grain and has propagated around it into the equiaxed grains behind it. From that point the crack propagates into the sample in two branches separated by approximately 90°. Scanning electron micrographs of the fracture

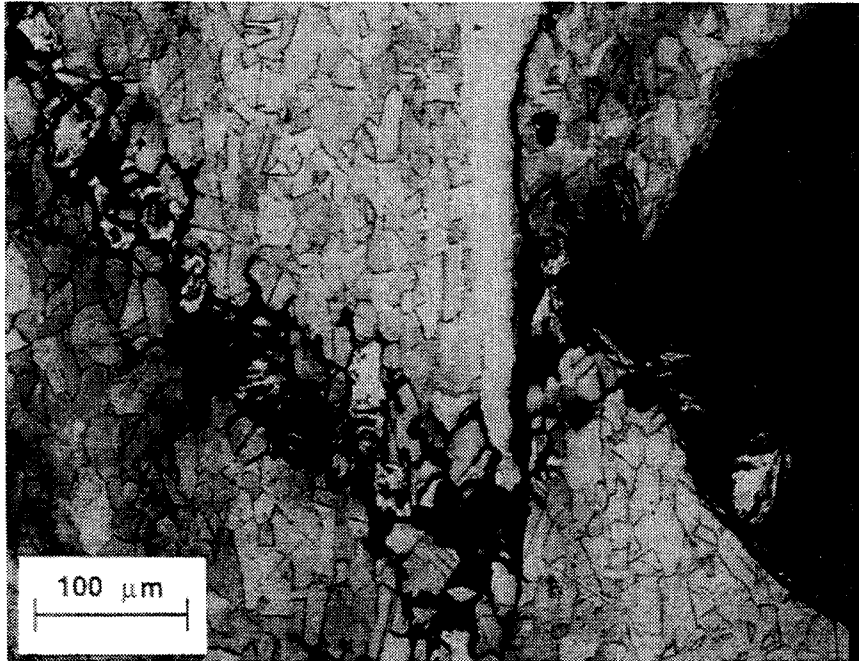


Figure 20. 20% cold-worked 650°C round bar test sample (469 MPa, 7.3 h, 1000 ppm O₂). Cross-section near unfailed notch showing elongated grain at the notch and crack path.

surfaces from the 20% cold worked material show a texture corresponding to the orientation of the elongated grains. Scanning electron micrographs of the fracture surfaces from samples manufactured from the 20% cold worked material without elongated grains (heat HV 5107) are planar. This is attributed to the absence of the large, elongated grains around which they must propagate. Comparing the two materials demonstrates that the texture seen in fractures of the 20% cold worked material is due to the elongated grains.

For materials that exhibit stress assisted intergranular oxidation, stress rupture data can be viewed from the perspective of a competition between creep and intergranular oxidation. Damage caused by intergranular oxidation, for example, can accelerate the creep rate and reduce ductility and life. This is because intergranular oxidation reduces the cross section over which the load is carried. [80] Similar observations were drawn from the alloy 908 stress rupture tests. When the creep rate was high, as it is at high temperatures and/or high loads, creep rupture predominated over the entire sample cross section. If the creep rate is lowered by lowering the temperature and/or load, intergranular oxidation will overtake creep initially. Then, when the sample cross section decreased sufficiently, rapid failure by ductile rupture occurs. The result is a decrease in total rupture life. The change in sample cross section, as indicated by the ratio of ductile fracture area to total fracture area, with increasing oxygen concentration, is shown in Figure 21.

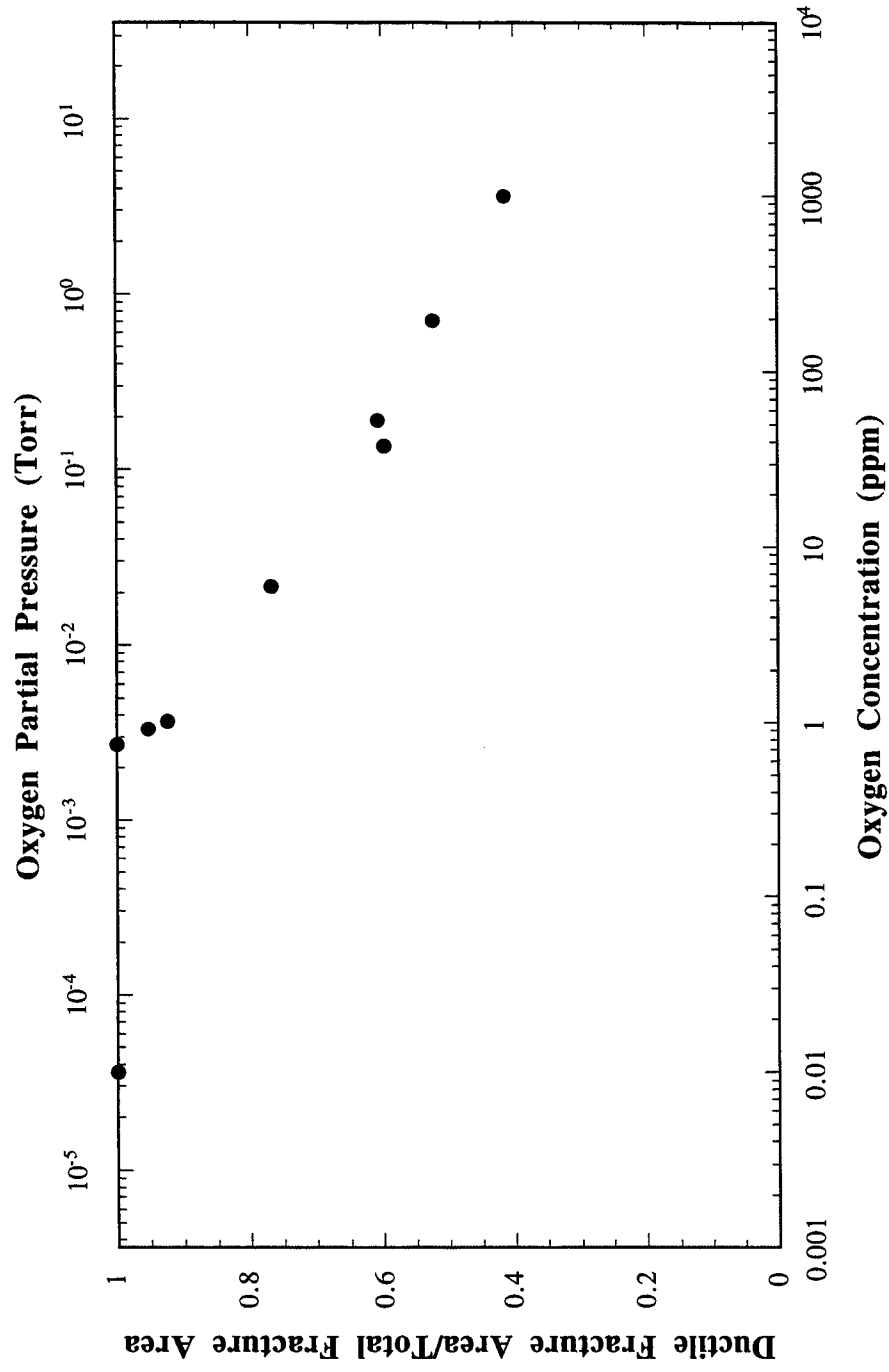


Figure 21. Ratio of ductile fracture area to total fracture area versus oxygen concentration for flat plate samples at 650°C and 651.5 ± 18 MPa stress range.

The establishment of a threshold oxygen concentration for oxygen assisted intergranular cracking based on percent intergranular fracture, with zero percent indicating that intergranular cracking will not occur, is a more appropriate way to utilize the stress rupture test results. The oxygen threshold values that other researchers have reported for a range of nickel-iron based superalloys, stainless steels and other fcc metals generally fall within a fairly narrow range. These researchers have determined this threshold using dynamic test methods. The value determined for alloy 908 based on percent intergranular fracture falls well within this range.

In order to further evaluate the predictive ability of the stress rupture data for alloy 908 to the CICC magnet application, it is necessary to examine the data using a time-temperature parametric relationship. In applying this relationship it must be remembered that intergranular oxidation damage is contributing to the stress/time/temperature behavior of this material and is a function of oxygen concentration.

The stress rupture data as presented in Figures 10 and 11, cover relatively small time, temperature, and stress regimes for a given oxygen concentration. In most cases, creep rupture data are presented using a time-temperature parameter that correlates time, temperature, and stress, allowing the data to be extrapolated. [83, 85, 86] One example of this is the extrapolation of stress rupture data to long times for components that will be in service for years or decades. Many time-temperature parameters have been developed to this end. [85, 86] The Larson-Miller parameter is the most commonly encountered of these. Since creep is a thermally activated process, the parameter was derived from the Arrhenius equation. The final form of the Larson-Miller relationship is expressed as

$$\frac{\Delta H}{R} = T(C + \log(t)) \quad (1)$$

where ΔH is the activation energy for creep, R is the gas constant, T is absolute temperature, t is time, and C is a material constant. In most cases the time is in hours. For nickel-iron base superalloys the material constant C is assumed to be 20.

A semilogarithmic plot of stress versus the Larson-Miller parameter [$T(C+\log t)$], using $C=20$, that compares flat plate air data with the low ppm oxygen data is shown in Figure 22. The position of the air data on the plot stems from rapid failure that is the result of a large loss (70-80% in air) in cross-sectional area due to intergranular oxidation. Because the flat plate stress rupture times were found to be relatively independent of oxygen concentration, the data in this plot have been grouped by oxygen concentration range. A similar plot for the round bar test data in air and at low oxygen concentrations is shown in Figure 23. This data shows better delineation with changing oxygen concentration. A

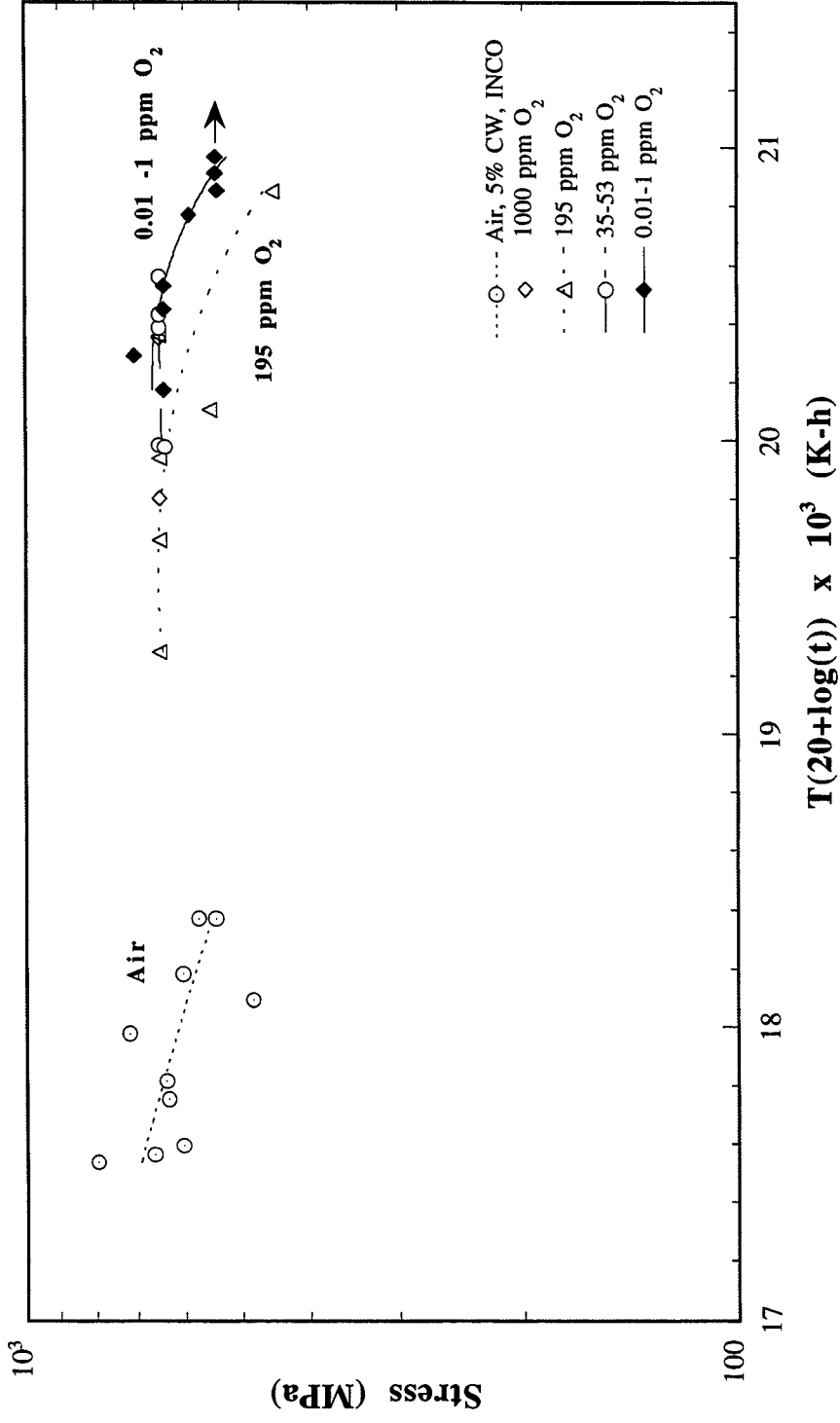


Figure 22. Larson-Miller parameter plot of low oxygen concentration flat plate test data compared with 5% cold work flat plate test data from INCO. [75]

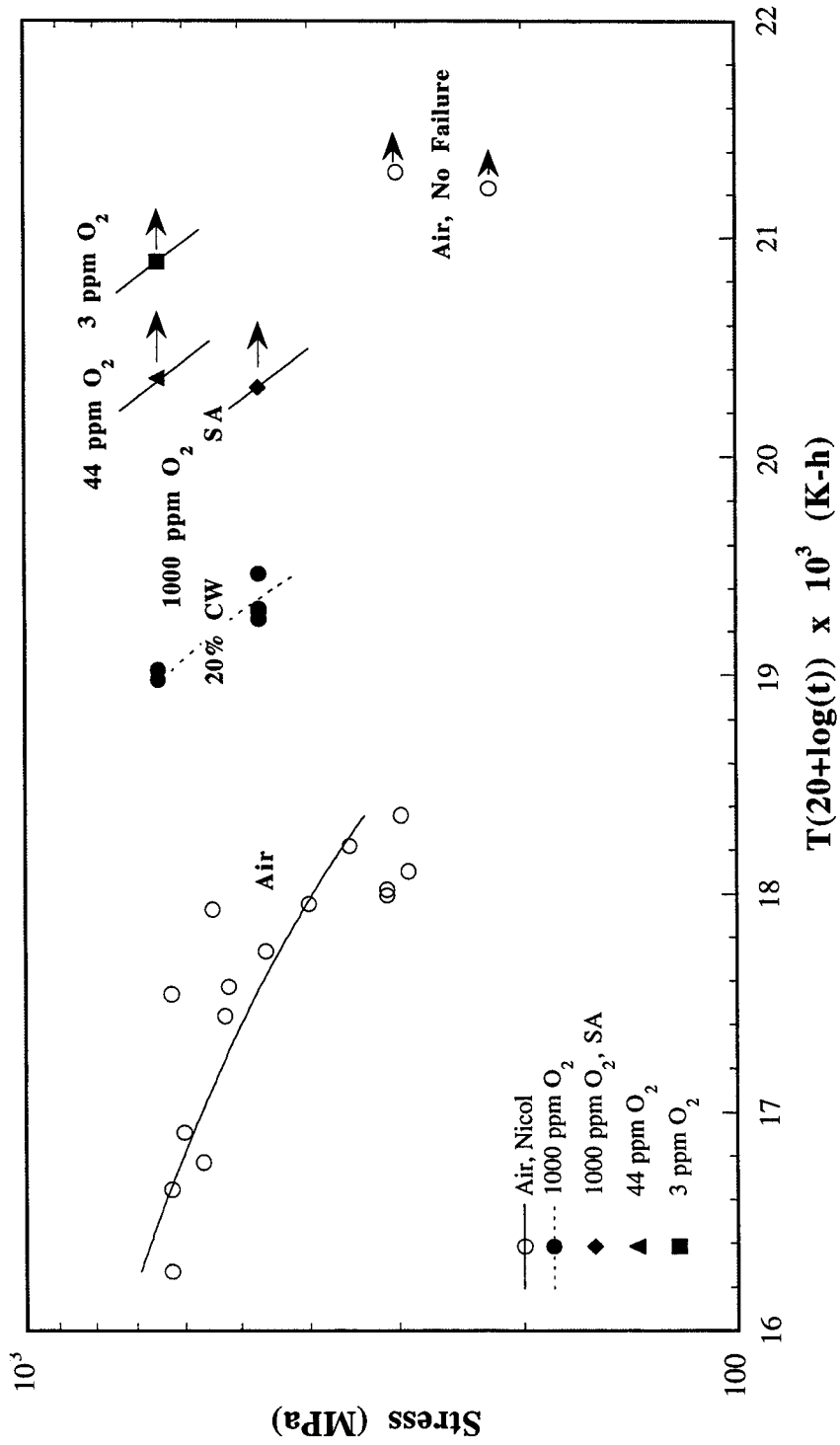


Figure 23. Larson-Miller parameter plot of round bar low oxygen concentration data for 20% cold work and solution annealed (SA, 980°C/1h) conditions compared with round bar data for 20% cold work material in air from Nicol. [11]

transition in the round bar air data occurs between 200 and 300 MPa, at which air test samples can show rupture lives in excess of 1000 hours. The scatter in the rupture life in this range, however, is extreme, with some failures occurring in less than 1 hour for stresses below 300 MPa.[11] More test data in excess of 1000 hours would be required to verify this transition.

Branching or divergence can be seen in Figure 22 for the 195 ppm oxygen range. Woodford examined divergence between air and argon (low ppm oxygen) stress rupture data and found it to be an environmental effect, related to the greater loss of sample cross section in air by oxidation. [87] For the flat plate samples, branching was found to be a function of stress, temperature, and oxygen concentration, and reflects an increase in rupture life with decreasing stress for a given test temperature and oxygen concentration. The 195 ppm oxygen data, for example, show divergence primarily because some of these data were generated at 750°C and, for a given stress, increasing the test temperature produces rapid failure with less intergranular fracture. This is the general result of decreased tensile strength and increased ductility with increased temperature that has been experimentally verified for alloy 908. [79] This is illustrated in the micrographs shown in Figures 16a through 16c for 750, 700 and 650°C tests at 650 MPa, respectively. As a result, the 750°C test samples fail in tension before the lower temperature samples and exhibit less intergranular fracture at comparable oxygen concentrations and stresses. This is apparent when comparing the times to rupture for the 650°C/650 MPa and 750°C/650 MPa data points in 195 ppm oxygen, 114.2 versus 0.06 hours, respectively, in Figure 15.

One problem with the presentation of published stress rupture data is that the mode of failure (transgranular versus intergranular) is not always given. In many cases, fractographic examination of the samples has not been performed. In air tests of nickel and nickel-iron base superalloys, intergranular crack propagation due to oxygen may account for most of the time to rupture, with final transgranular rupture occurring rapidly in the remaining cross section area. [49, 50] As discussed above, oxygen's most immediate effect on stress rupture data is to reduce the effective cross sectional area through intergranular oxidation. Woodford has suggested that the departure between air and argon data may be accounted for by correcting the Larson-Miller material constant, C , for loss of sample cross-section due to oxidation. [87]

The alloy 908 data were examined using the graphical creep-rupture correlation that uses the convergence of isostress lines on a plot of $\log(t)$ versus $1/T$ to determine a value for the material constant C . [82, 86] It was found that if each set of stress-temperature data was grouped by percent intergranular fracture, a correlation did exist. The rationale behind this approach assumes that, for notched stress rupture samples, the time to rupture

is close to the time to initiate a crack. [32] This assumption has been validated for both round bar and flat plate samples of alloy 908 tested in air by Nicol and Sizek, respectively. [11, 75] Also, if the data are grouped by percent intergranular fracture, it can be assumed that, for the same load and temperature, the stress on the remaining ductile area at failure was equivalent.

The data groupings for the 650 and 540 MPa isostress lines and their least squares fits are shown in Figure 24. The average of the intercepts for the isostress lines was used to obtain a value of 30 for the material constant C . The low ppm oxygen flat plate data were replotted using the new Larson-Miller parameter, $T(30+\log t)$, and are shown in Figure 25. Comparison with Figure 81 shows the improved data fit using $C = 30$. By entering a time and temperature into the Larson-Miller parameter, the rupture stress can be read from the “master curve” shown in Figure 88. Alternately, if the stress and temperature are known, a time to rupture can be calculated. The time to rupture values obtained using $C = 30$ show good correspondence to the experimental values for the flat plate samples. The time to rupture for flat plate samples at 650°C and 650 MPa, for example, is predicted to be 117 hours from the curve. From the experiments, the mean time to rupture at 650°C is 108.3 ± 36 hours at 651 ± 18 MPa. In using this “master curve” it must be noted that it is applicable only to the midsection (0.1-1000 ppm oxygen) of the sigmoidal curve shown in Figure 18. In the plateau below 0.1 ppm oxygen, environmental effects are absent and pure creep rupture is controlling. The second plateau, above 1000 ppm oxygen, represents the regime where the rupture life is primarily controlled by a reduction in sample cross section (70-80%) due to intergranular oxidation. While this result can be used to obtain a time to rupture as a function of stress and temperature, in actuality some intergranular cracking will have occurred before final failure. The depth or amount of intergranular fracture will be determined by the oxygen concentration.

Grain Boundary Analysis

Round bar test samples are preferred for grain boundary analyses. The intact notch they provide is desirable not only because it preserves pre-failure microstructural features, but also, for the purposes of this study, intact grain boundaries. Grain boundaries that have not cracked open provide evidence of pre-failure chemistry and intergranular oxidation, if present, without having direct exposure to the environment. In cases where intact notches were not available, i.e. flat plate samples, intact grain boundaries that branched off the main crack were selected for analysis.

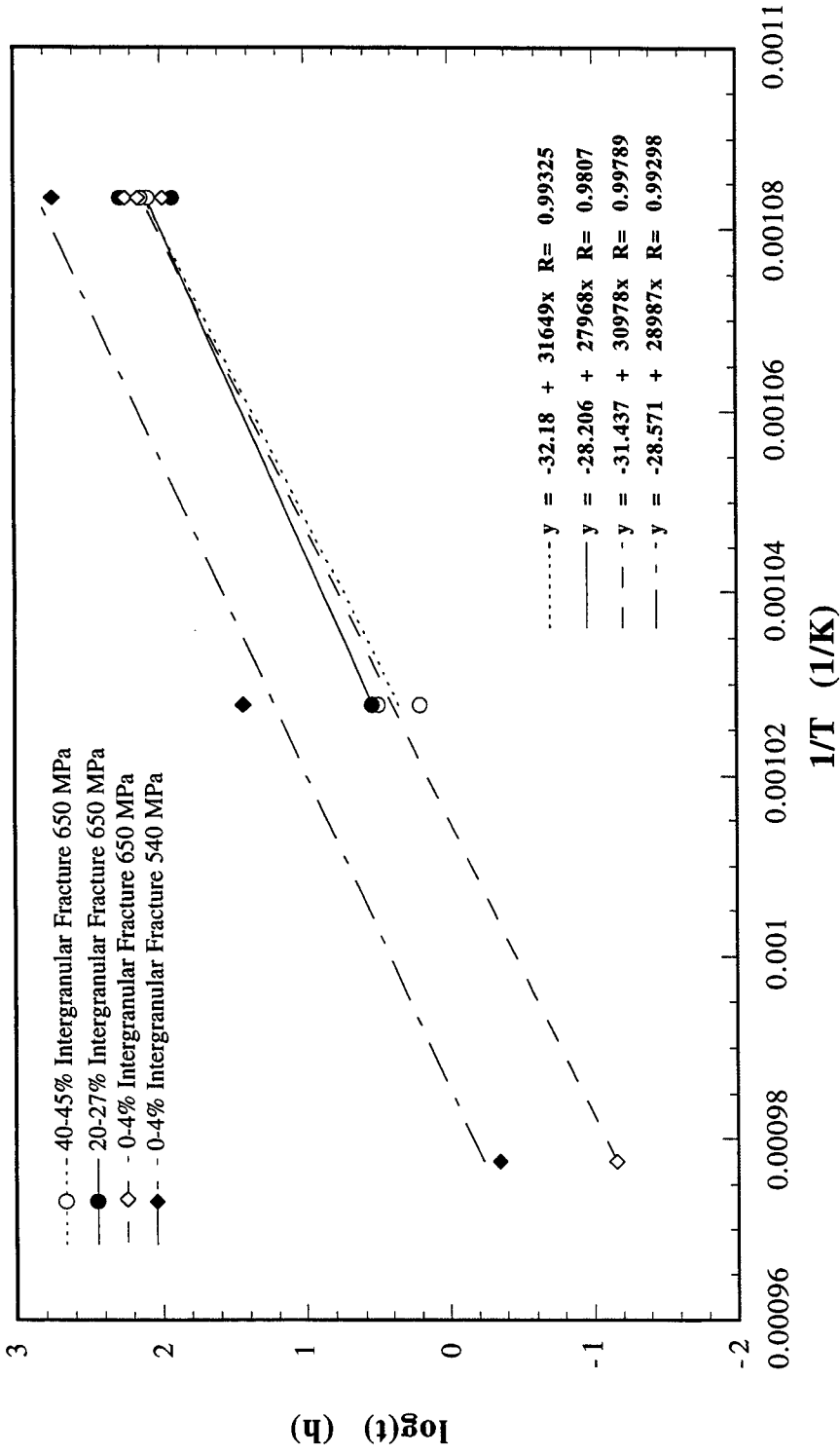


Figure 24. Plot of isostress lines and least squares fits for 650 and 540 MPa stresses. Least squares fits for 650 MPa data have been grouped by percent intergranular fracture.

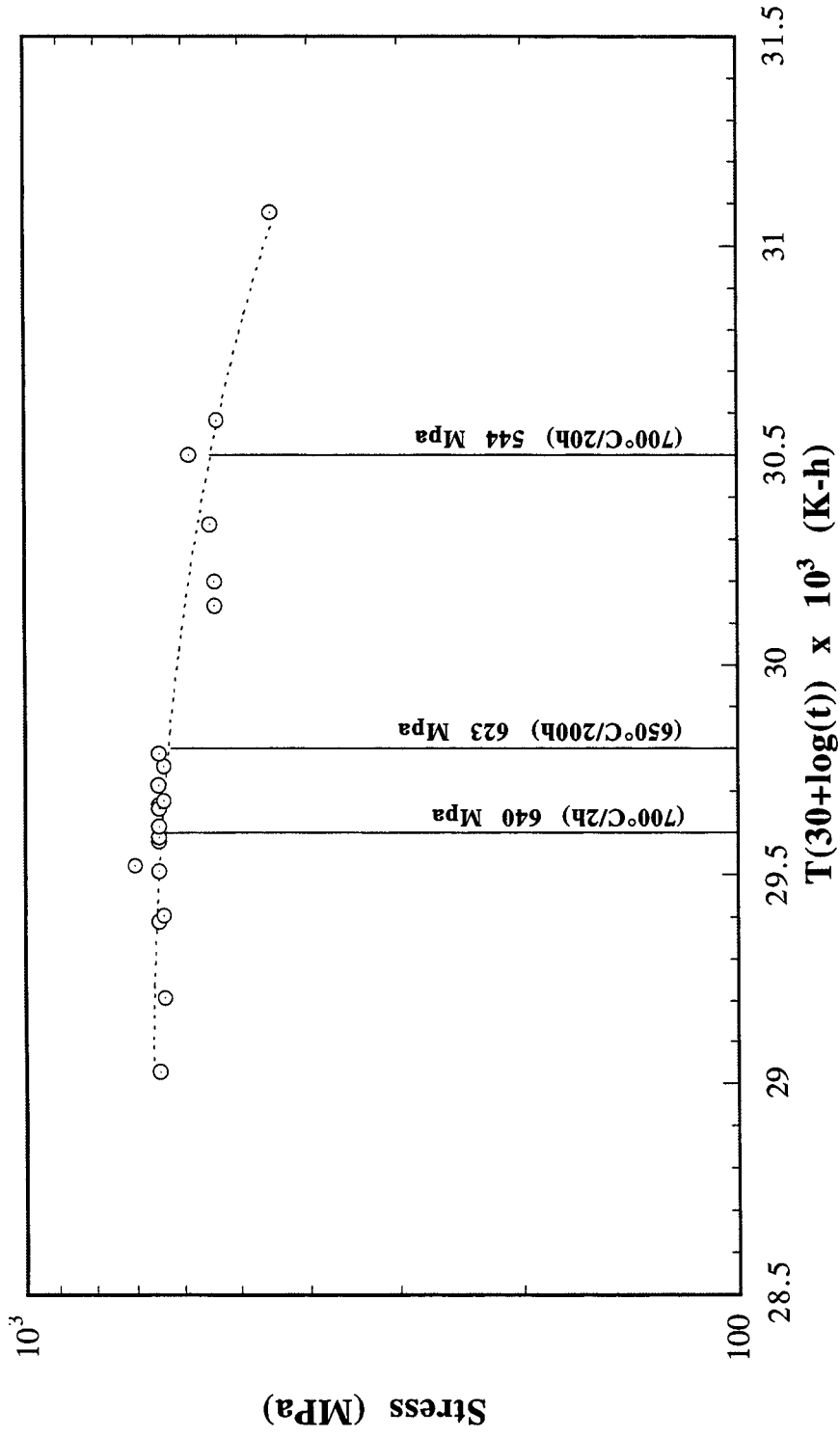


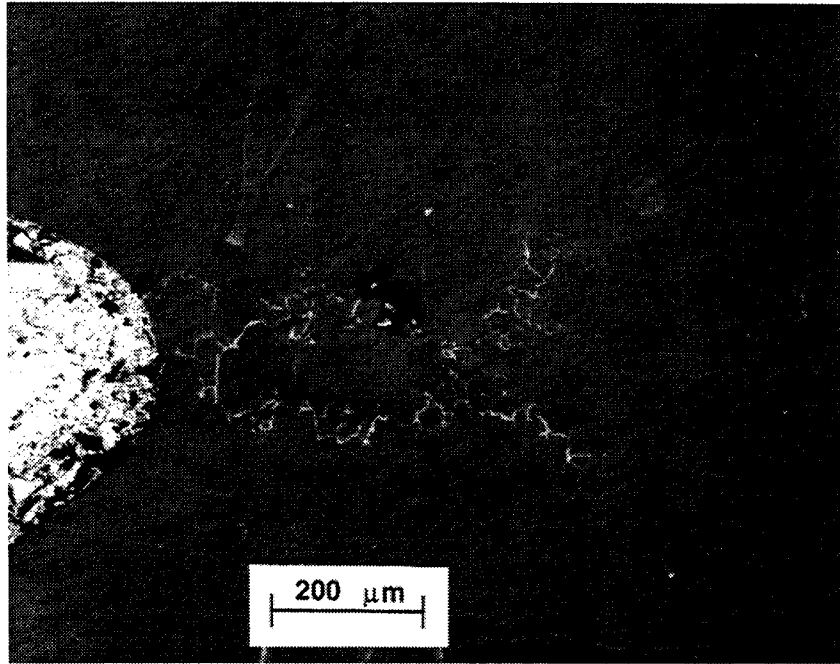
Figure 25. "Master curve" for solution annealed flat plate stress rupture data based on new material constant $C = 30$.

In general, the cracks in the unfailed notches were closed with an intact oxide along the intergranular boundaries. An example of an intact notch with oxidized grain boundaries is shown in Figure 26a. When examined using SEM, the oxidized grain boundaries appear as shown in Figure 26b. In this micrograph the oxidized grain boundaries appear dark. This is due to the deeper penetration and therefore greater capture of secondary electrons, used for imaging in the SEM, into the low molecular weight oxide relative to the surrounding metal matrix.

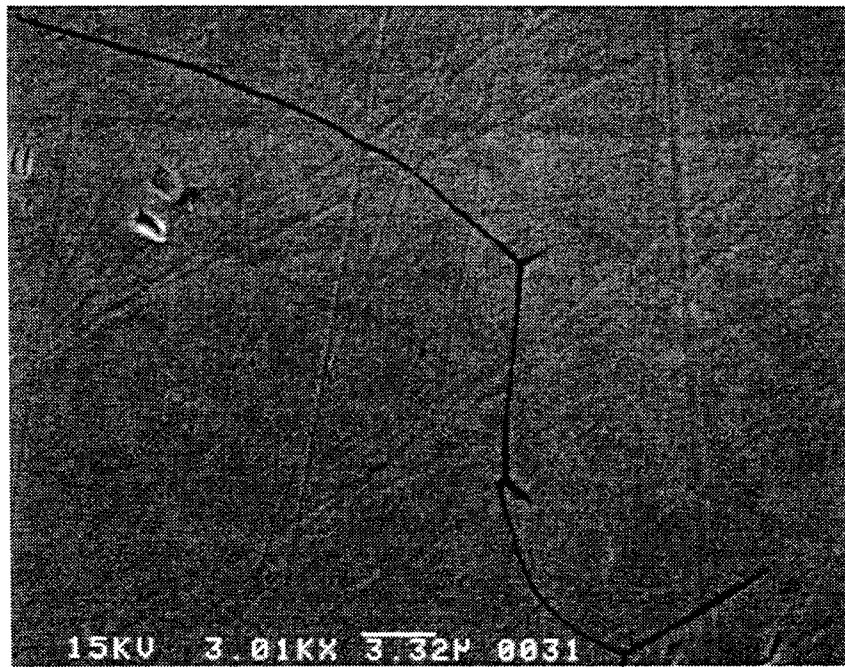
In order to establish which elements were predominant at the affected grain boundaries, an initial chemical analysis was performed by EDS using elemental x-ray mapping of the grain boundaries. As shown in the SEM micrograph in Figure 27a and the EDS x-ray map in Figure 27b, oxygen is segregated at the grain boundaries, which are roughly outlined in the x-ray map. Elemental maps for the other elements present in this analysis are shown in Figure 28. From this it can be seen that oxygen is the only element that is concentrated at the grain boundaries, indicating oxidation. There is no segregation of chromium, titanium or aluminum to the grain boundaries. A reduction in nickel is evident. Iron is present at the boundaries and, in combination with nickel and oxygen, may indicate that a nickel-iron oxide has formed there.

Electron beam spot analyses were performed at high magnifications across affected grain boundaries to detect compositional differences at grain boundaries. A 100 second analysis time was used for each spot to insure a good statistical ratio of x-ray counts for each element peak above background.

An analysis was performed across the grain boundary shown in Figure 29. The white spots present in this micrograph are electron beam contamination spots that mark the points at which compositions were determined. The resulting composition profile is shown in Figure 30. From this composition profile it is evident that oxygen is present on the grain boundary. Nickel and iron show some reduction at the boundary. A reduction in the weight percent of these elements at the grain boundary indicates that they have oxidized. Reaction with oxygen reduces their relative weight percents in the formation of oxide to levels below those of the matrix. In most cases, the composition profiles acquired across grain boundaries in the 650°C, 1000 ppm oxygen, round bar samples did not show segregation of Cr, Ti, Al, or Nb. This can be attributed to a combination of factors, one of which is the relatively small sample volume being analyzed. Oxidized grain boundary widths at these magnifications ranged from 0.1 to 0.5 microns. Another is that the electron beam spot size is of the same magnitude relative to the grain boundary width, one limitation of EDS analyses in the SEM even at their smallest spot size condition. Lastly, these elements may not be segregated at the grain boundaries in sufficient quantities to

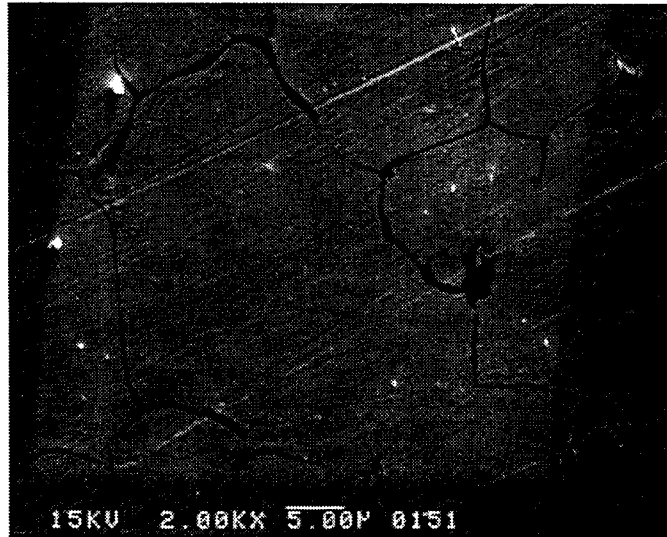


a

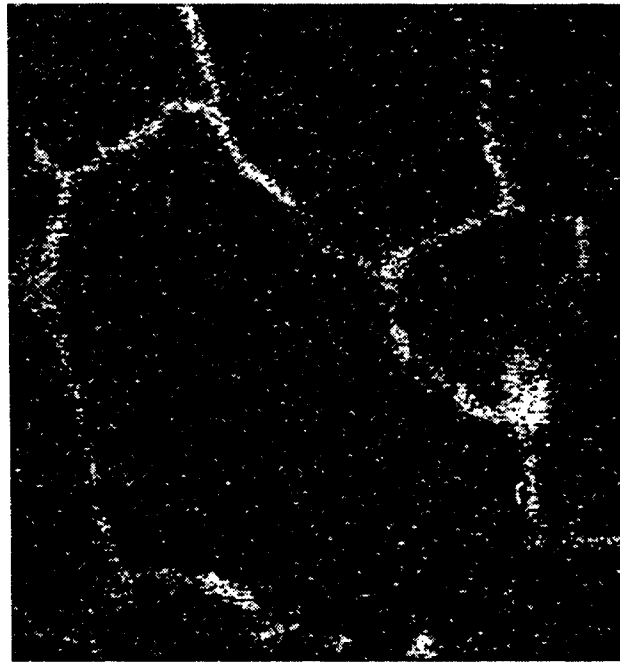


b

Figure 26. (a) Normarski optical micrograph of the crack path at the unfailed notch in a 650°C round bar sample (469 MPa, 8.2 h, 1000 ppm O₂), sample coated with evaporated carbon to highlight oxidized crack. (b) SEM micrograph of affected grain boundaries in a 650°C round bar sample (1000 ppm O₂, 650 MPa, 4 hours to failure).



a



b

Figure 27. (a) SEM micrograph and (b) oxygen x-ray map of grain boundaries in a 650°C sample (10% cold, work 1000 ppm O₂, 469 MPa) 8.2 hours to failure.

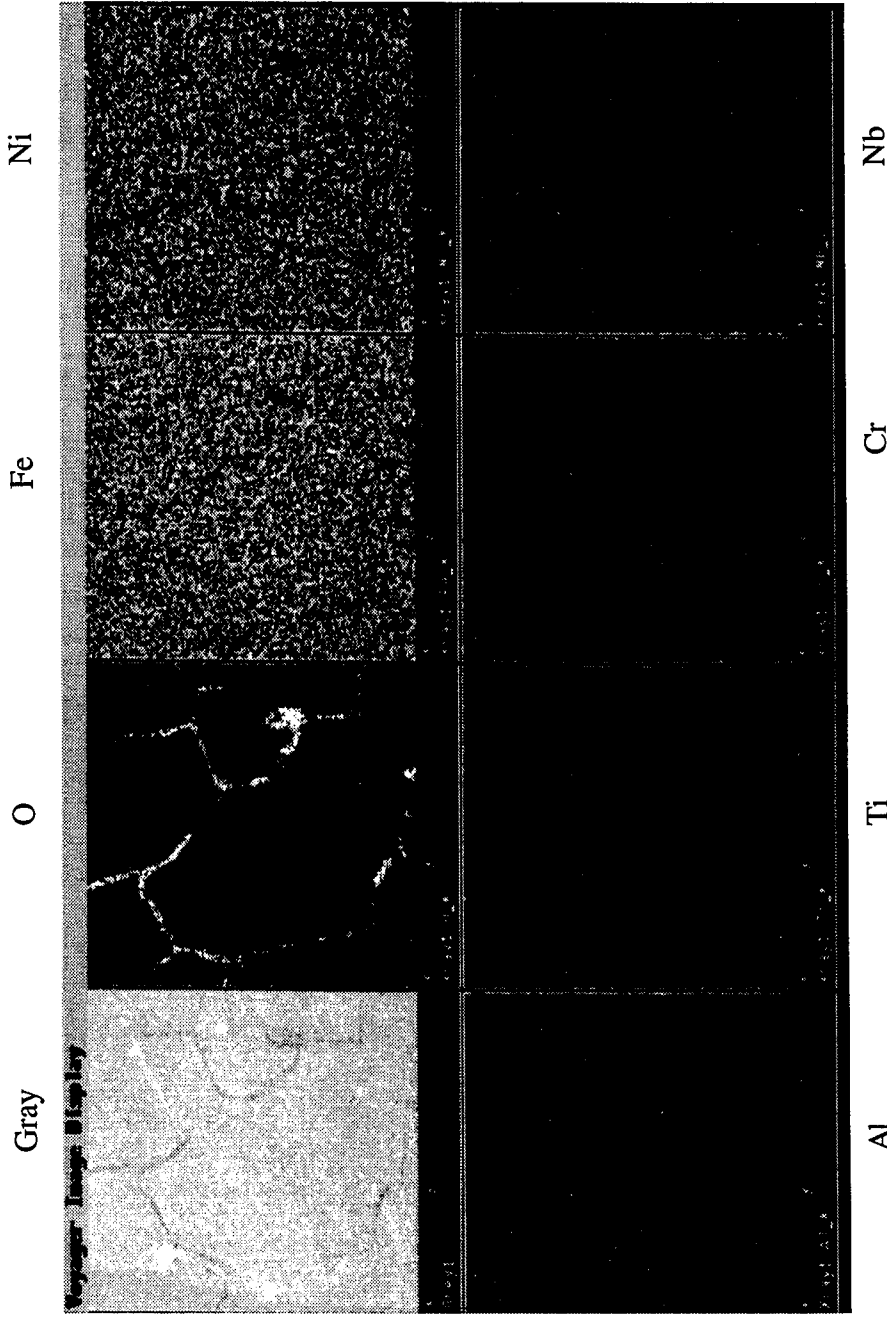


Figure 28. EDS X-ray map of elements present along grain boundaries at the unfailed notch of a round bar sample tested at 650°C, 469 MPa, and 1000 ppm O₂. An SEM micrograph of the selected region is shown in Figure 27a.

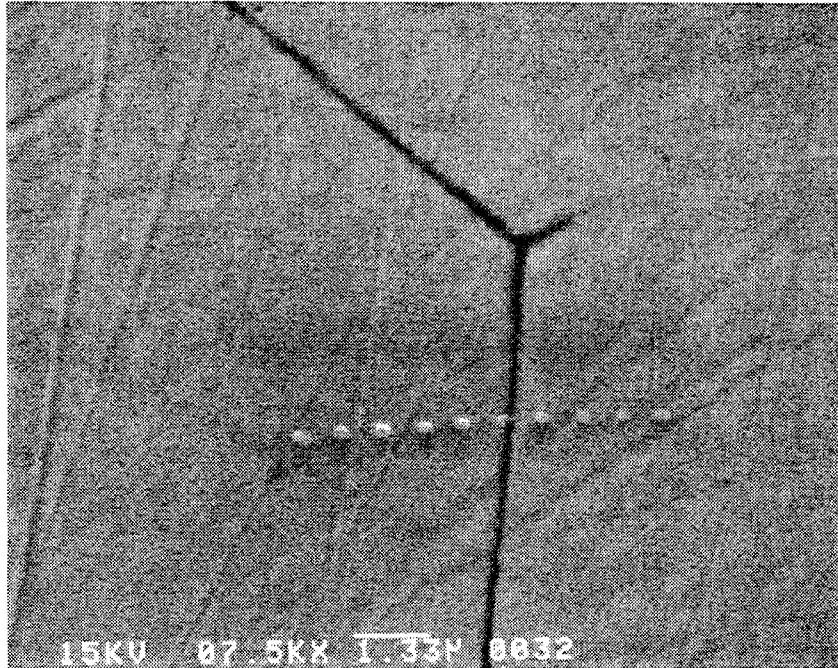


Figure 29. Grain boundary at triple point, from 650°C sample round bar sample (1000 ppm O₂, 650 MPa, 4 hours to failure), selected for EDS composition profile.

distinguish them from the matrix. Generally, a ± 0.5 weight percent difference is required. Analyses at random locations along oxidized grain boundaries yielded similar results for the round bar samples. One difference in composition was, however, noted at the very terminus of oxidized grain boundaries. Here a slight increase in chromium was evident. The terminus of intergranular oxidation is fairly difficult to resolve and analyze in the SEM given the small volume of oxide present. One profile, taken across the terminus of an oxidized grain boundary was obtained at high magnification (20,000x) and is shown in Figure 31. A 2 to 2.5 weight percent increase in chromium can be seen at the grain boundary in this profile. This result suggests agreement with Andrieu's hypothesis that intergranular oxidation continues until intergranular oxygen diffusion is arrested by the precipitation of chromium-rich oxides. The terminus of the oxidized grain boundary corresponding to the point at which the arrest occurred. As such, the stress rupture test samples provided a frozen picture of the chemical history of the oxidized grain boundary before final failure.

It was necessary to test the hypothesis that the concentration of chromium present in the intergranular oxide would increase at the terminus of intergranular oxidation. To do this a series of composition profiles were obtained from EDS spot analyses along, rather than across, grain boundaries. One such profile was obtained from the oxidized grain boundary

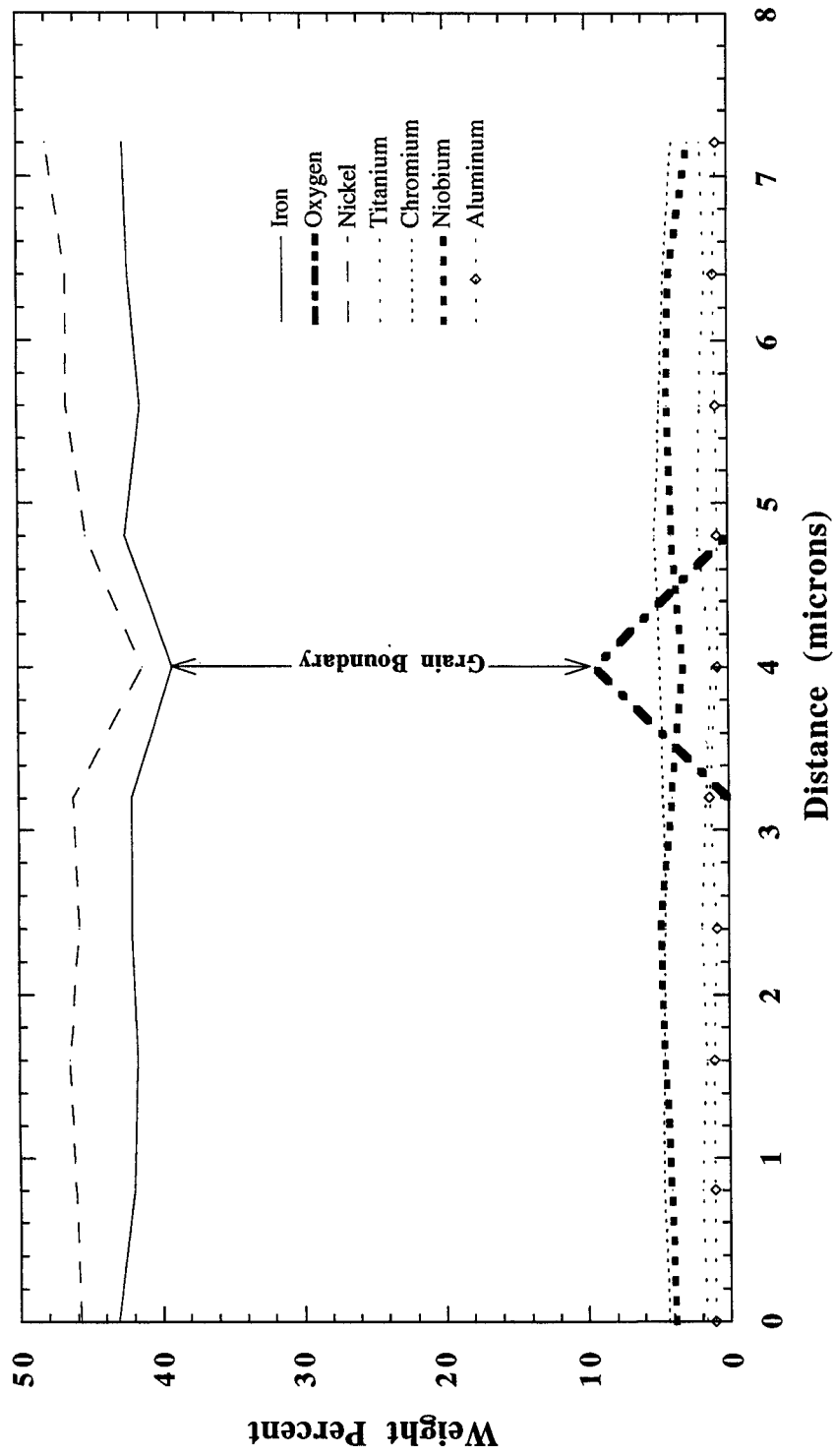


Figure 30. EDS composition profile across a grain boundary in a 650°C round bar sample (650 MPa, 1000 ppm O₂, 4 hours to failure). Profile generated at 7,500x and 15 kV. An SEM micrograph of the grain boundary used is shown in Figure 29.

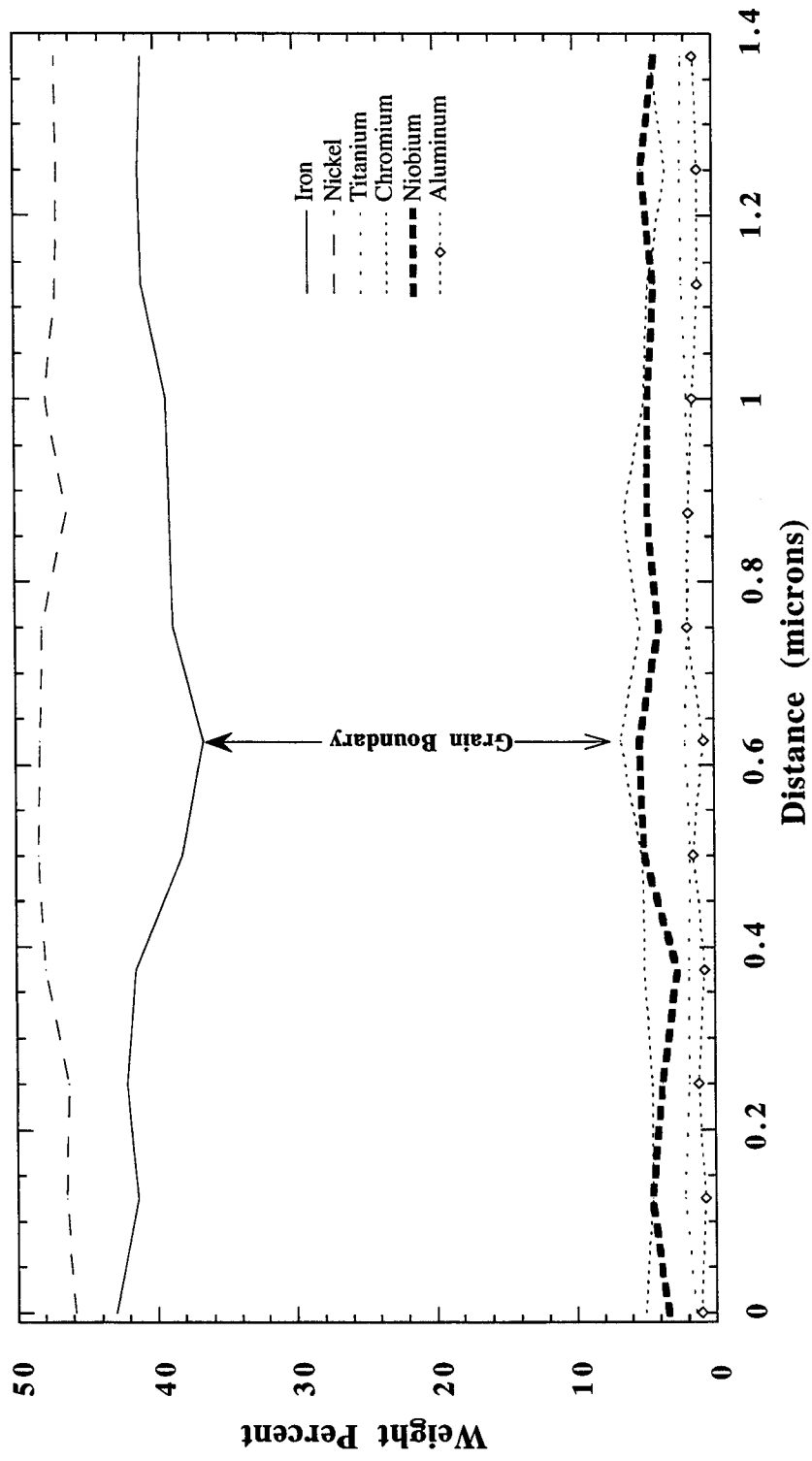
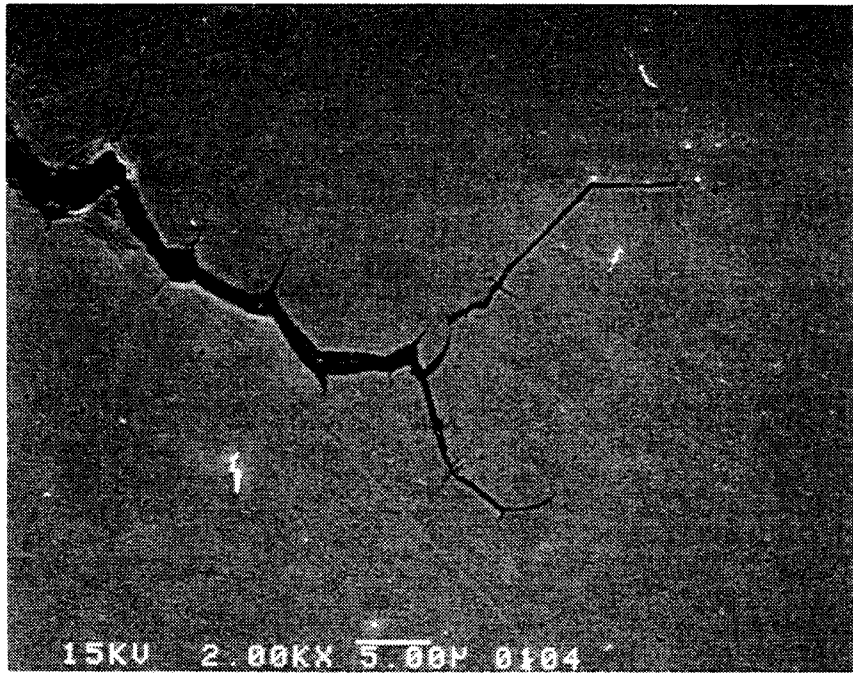


Figure 31. EDS composition profile across an affect grain boundary in a 650°C round bar sample (469 MPa, 1000 ppm O₂, 12.3 hours to failure). Profile generated at 20,000x and 15 kV.

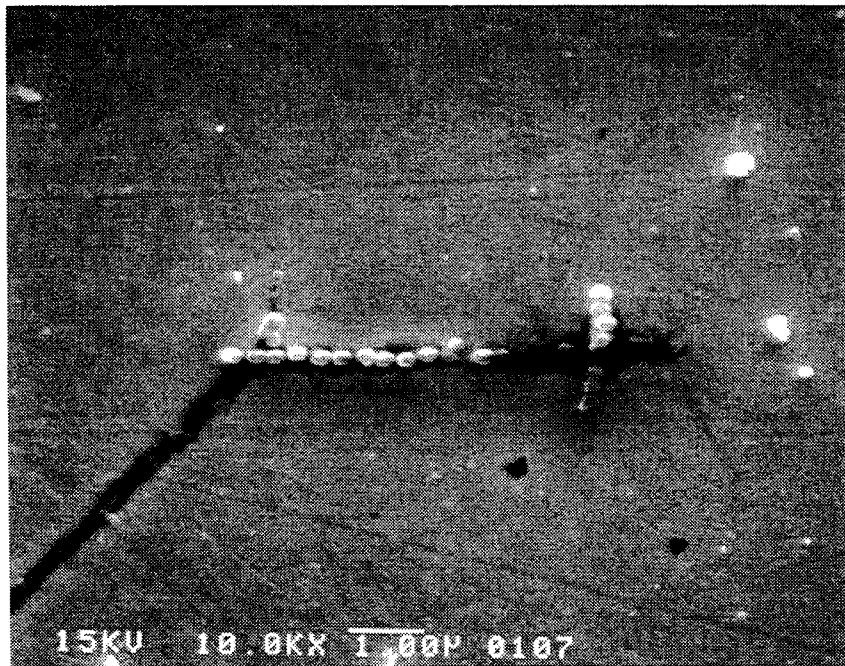
shown in Figure 32a. The spots marking the points chosen for analysis are shown in Figure 32b. Composition profiles taken from points extending along and across the terminus of this grain boundary are shown in Figures 34 and 35, respectively. As seen in Figure 33, oxygen is present along the entire length of the grain boundary. As the grain boundary terminus is approached from the matrix, however, it is apparent that the concentration of chromium increases. A similar but less pronounced increase in niobium can also be seen. From the grain boundary orientation in the micrograph (left to right) in Figure 61b, the matrix point used is closer to a branch of the main crack and the environment. Higher oxygen and iron levels are present along the segment of boundary closest to the main crack and the environment, while the chromium concentration increases away from the main crack. Andrieu reported similar findings in alloy 718 and attributed them to the formation of chromium rich oxides in low oxygen potential environments found at the tip of cracks. [53, 55] The companion composition profile, taken across the terminus of the oxidized grain boundary is shown in Figure 34 and confirms the concentration increase.

An analysis was performed on a round bar sample tested at 650°C in 1000 ppm oxygen (3.65 hours). The second notch in this sample had opened during testing and is shown in Figure 35a. The grain boundary selected for compositional analysis is shown in Figure 35b. From the profile for this boundary, shown in Figure 36, it is apparent that in this sample there is no significant increase in the chromium concentration along the boundary. The profile does, however, show oxygen present along the boundary. The results from this round bar sample are consistent with the previously reported findings based on x-ray maps and line profiles of affected grain boundaries in the other round bar samples tested at 650°C in 1000 ppm oxygen. With the exception of small increases at the very terminus of the oxidized boundaries, as was previously shown, significant segregation of chromium to the grain boundaries in round bar samples was not evident. Chromium enrichment is, however, evident along grain boundaries in comparable 650°C flat plate samples that were also tested in 1000 ppm oxygen. Aside from geometry, the main distinction between these two samples types is the time to failure, with the flat plate samples failing at longer times than equivalent round bar samples. Flat plate samples tested at lower oxygen concentrations also exhibited chromium concentrations at their grain boundaries that were from 2 to 10 weight percent above matrix levels. Chromium concentration was a function of position along the affected boundary, with the highest levels closest to the terminus.

The factors affecting the transition between internal/intergranular oxidation and external oxidation are the oxygen partial pressure and the concentration of the oxidizable solute. In Ni-Cr alloys and Ni-Fe base superalloys the external, passivating, oxide is either Cr_2O_3 or



a



b

Figure 32. (a) SEM micrographs of oxidized grain boundaries in a 650°C flat plate sample (650 MPa, 38 ppm O₂, 122 hours to rupture). (b) Micrograph of grain boundary selected for compositional analysis by EDS.

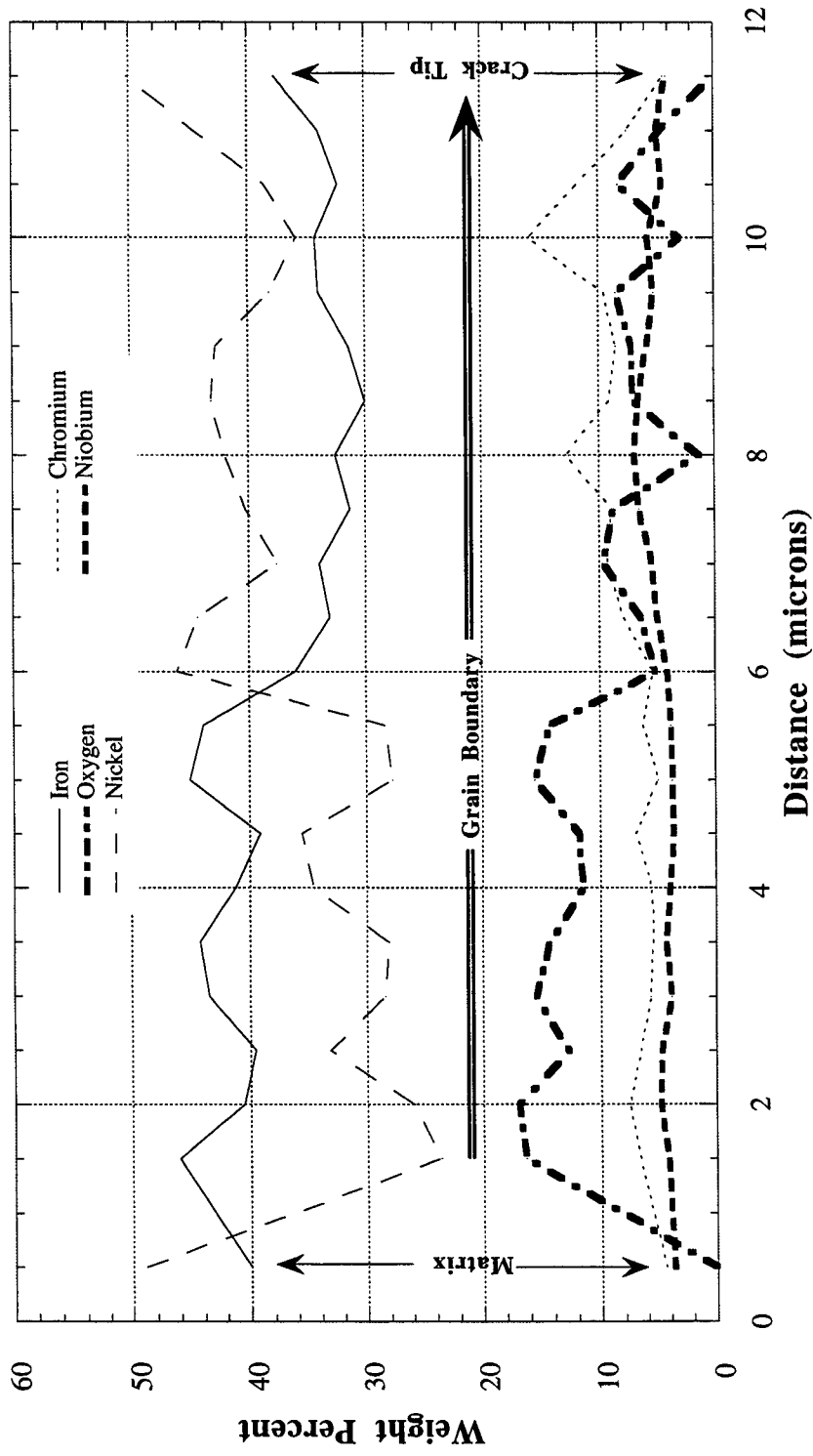


Figure 33. EDS composition profile along grain boundary extending to terminus in a 650°C flat plate sample (650 MPa, 38 ppm O₂, 122 hours to failure). Obtained at 10,000x and 15 kV. Si, Ti, and Al did not show any variation in this profile and were removed for plot clarity.

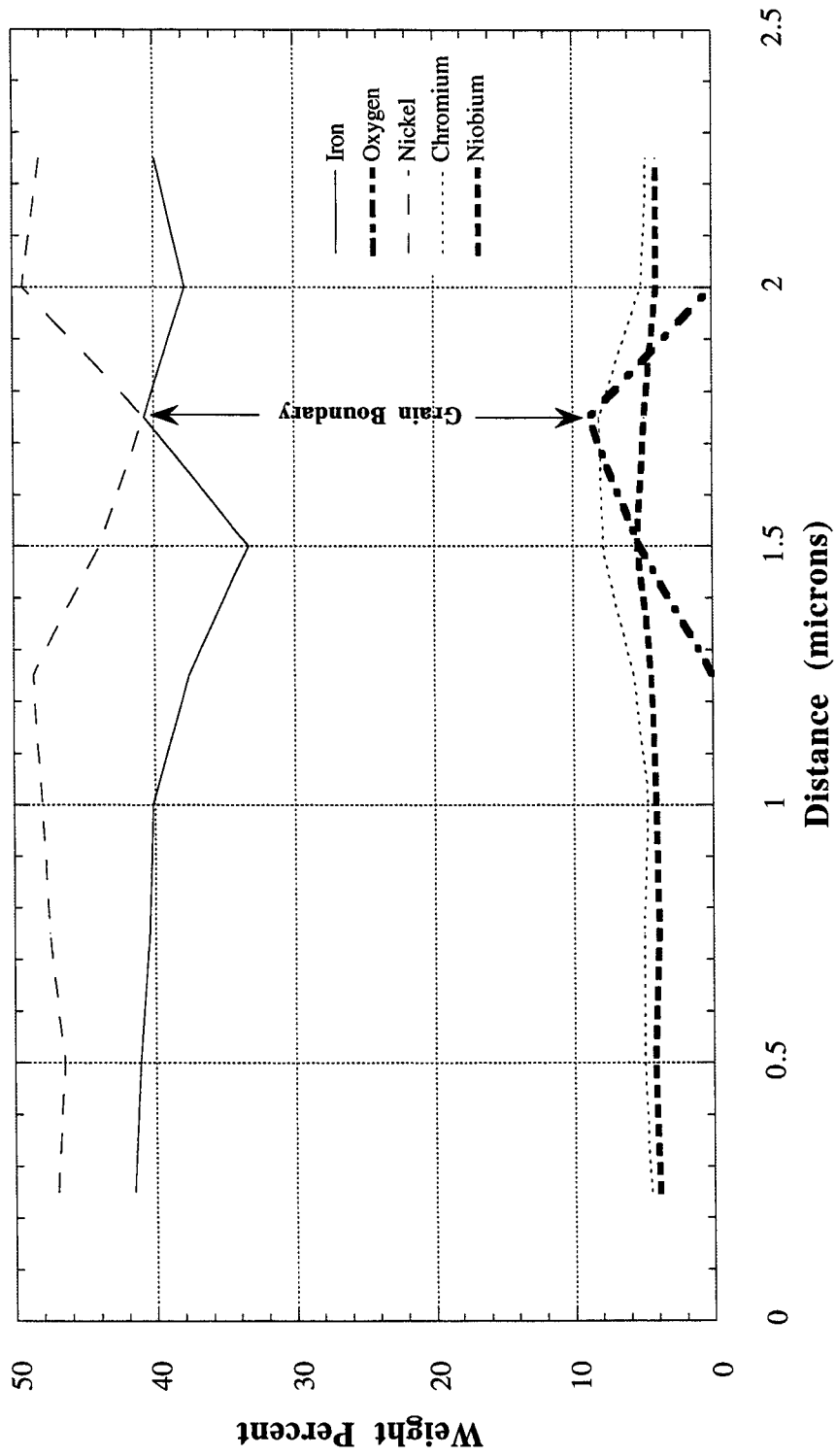
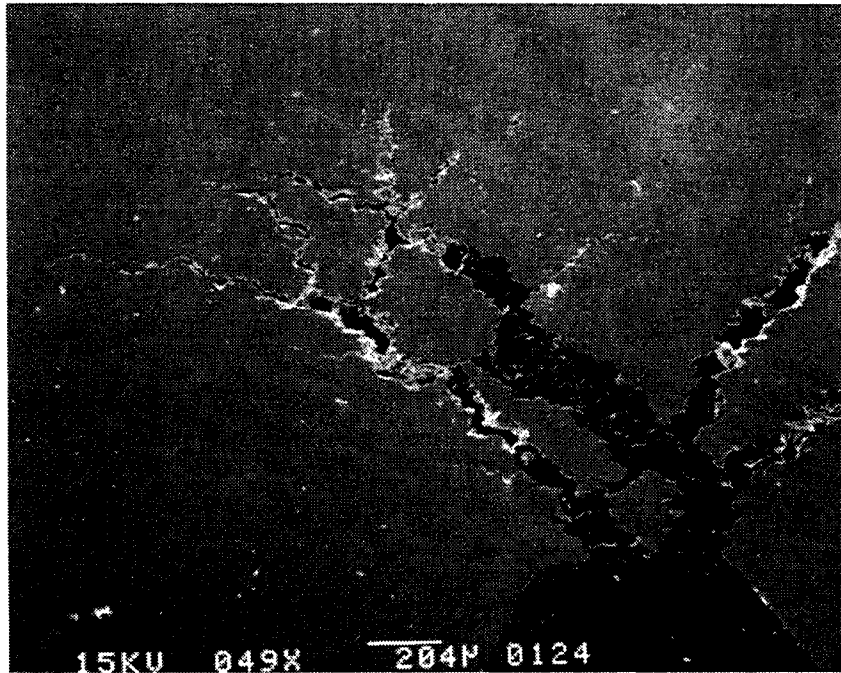


Figure 34. EDS composition profile across grain boundary in a 650°C flat plate sample (650 MPa, 38 ppm O₂, 122 hours to failure). Obtained at 10,000x and 15 kV. Si, Ti, and Al did not show any variation in this profile and were removed for plot clarity.



a



b

Figure 35. (a) SEM micrograph of crack at notch in a round bar sample (650 MPa, 1000 ppm O₂, 3.65 hours to failure). (b) SEM micrograph of grain boundary at the farthest distance from notch used for compositional analysis.

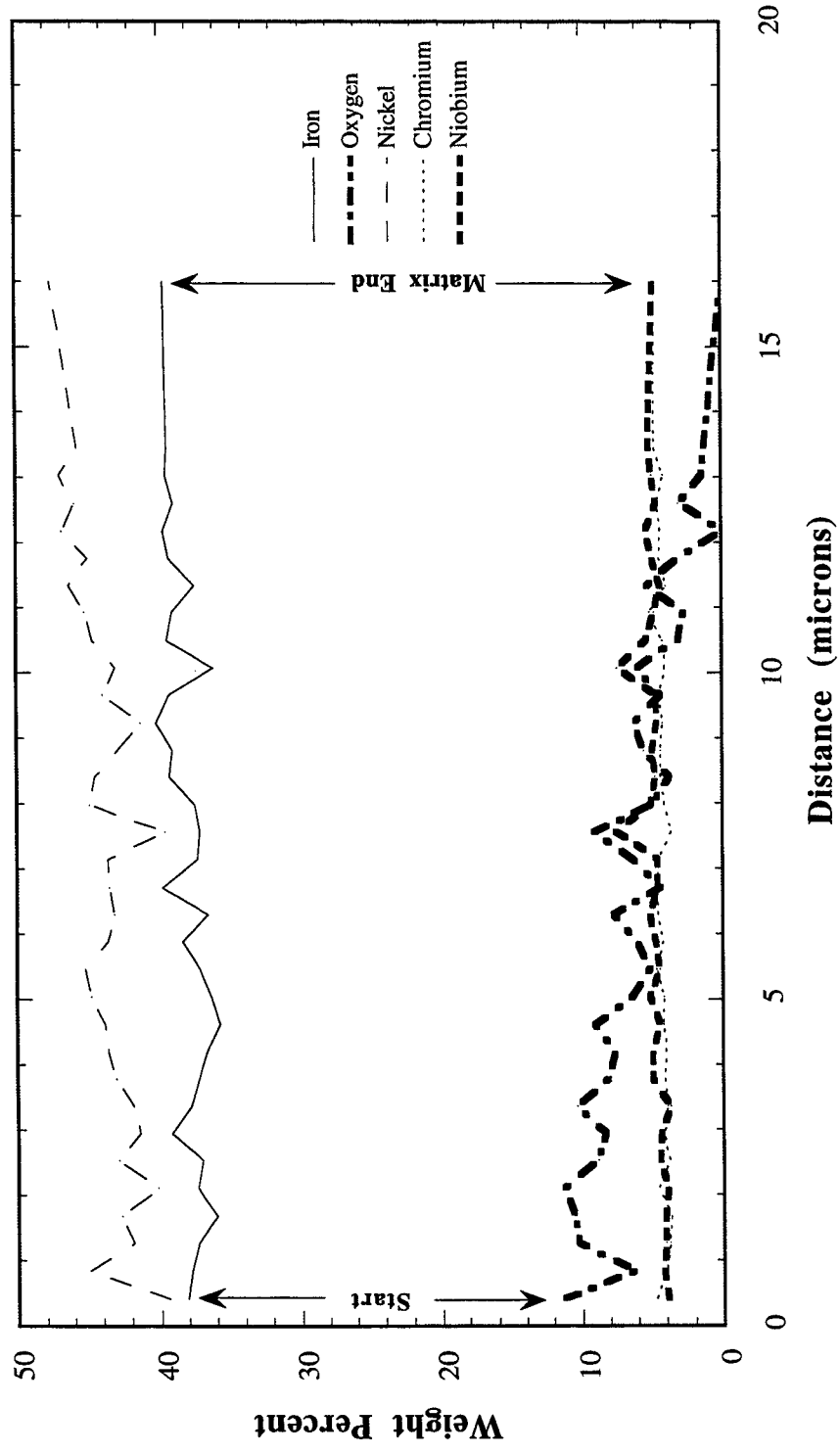


Figure 36. EDS composition profile along grain boundary in a 650°C round bar sample (650 MPa, 1000 ppm O₂, 3.65 hours to failure). Obtained at 12,000x and 15 kV. Si, Ti, and Al did not show any variation in this profile and were removed for plot clarity.

NiCr_2O_4 . [59] This transition in mode of oxidation appears correlate with the oxygen concentration dependence observed for intergranular oxidation in alloy 908. Of particular significance is the existence of a transition time to achieve a given depth of internal/intergranular oxidation. In matrix internal oxidation this time is linked to the nucleation and growth of oxide particles within the internal oxide zone. As the oxide particles in this zone coarsen, they act to block the diffusion paths for oxygen into the alloy. [59, 61] Oxygen diffusion into the alloy is effectively shut off once these oxide particles reach some critical volume fraction. [59, 61] The time required to reach this critical volume fraction determines the depth of internal oxidation. In an analogous manner, this work suggests that intergranular oxidation occurs within a subsurface zone. The depth of this zone is controlled by the oxygen concentration at the surface of the alloy. As with internal oxidation, the formation of intergranular oxides is required to block the intergranular diffusion of oxygen. The intergranular oxide formed in Ni-high Cr alloys is typically Cr_2O_3 . [72] Dilute (1-5 wt.% Cr) Ni-Cr alloys form varying proportions of Cr_2O_3 and NiCr_2O_4 intergranularly. [67] The predominant intergranular oxide deeper within the zone of internal/intergranular oxidation is Cr_2O_3 . [67]

The above observations explain why chromium was present in the intergranular oxide at the terminus of oxidized grain boundaries in the long-time flat plate material. The round bar test samples formed only (Ni,Fe)-type intergranular oxides. These samples failed too rapidly to develop chromium-rich intergranular oxides. This is based on the internal oxidation model for the time required to form an oxide that can effectively block oxygen diffusion.

The grain boundary oxide EDS compositions are shown along with their corresponding matrix EDS compositions in Table 3 for some of the stress rupture samples. It should be noted that the oxygen potentials at the sample surface for all the tests done in this study are above the oxygen potentials for formation of most of the metallic oxides at 650°C , based on the Ellingham diagram. [88] The reported oxygen potentials, however, do not indicate the oxygen potential below the surface oxide layer or along the grain boundaries. At these locations the oxygen potential is determined by the kinetics of oxygen diffusion through the external scale and along the grain boundaries. [62] When comparing these compositions it must be remembered that these were insitu analyses taken from metallographic cross sections and should be compared on a relative basis to the material heat composition also shown in the table. This is because these analyses incorporate some of the matrix elements due to subsurface scattering of the SEM electron beam during EDS. From the surface oxide analyses shown in this table, it can be seen that the low oxygen potential test samples, below -12.7 kcal/mole (650°C , 1000 ppm oxygen), were enriched with respect to

Table 3. Compositions of Surface and Grain Boundary Oxides From Alloy 908 Stress Rupture Samples.

Oxide Location	Sample Type	Sample	O ₂ Potential (kcal/mole)	Time (h)	T (°C)	Composition (weight percent)*															
						Ni	Fe	Cr	Nb	Ti	Al	Si									
	Heat	Y9401K				49.3	40.8	3.99	3.04	1.55	1.01	0.16									
Surface	Flat	38P	-26.6	522	650	9.8	8.7	11.2	17.7	5.2	4.2	2.9									
Surface	Flat	8P	-25.5	211	650	16.9	20.8	15.2	6.7	7.0	3.3	1.7									
Surface	Flat	66T	-22.0	61.5	650	2.0	2.4	1.6	46.7	0.7	-	-									
Surface	Flat	62P	-18.67	122	650	24.0	28.0	5.9	6.1	3.6	1.4	-									
Surface	Flat	23P	-12.7	77	650	9.2	31.3	9.2	2.0	1.6	3.1	3.3									
Grain Boundary	Flat	62P	-18.7	122	650	37.2±7.7	37.5±5.1	7.8±2.9	4.8±2.9	1.9±0.4	1.3±0.2	0.4±0.1									
		Matrix				47.2±0.6	40.8±0.7	4.8±0.2	4.0±0.1	1.6±0.1	1.2±0.1	0.3±0.1									
Grain Boundary	Flat	49P	-12.7	28.3	650	45.6±8.0	27.2±6.9	8.1±4.0	5.9±1.2	2.6±0.1	1.8±0.4	0.6±0.2									
		Matrix				46.4±0.3	41.3±0.2	4.7±0.3	4.2±0.3	1.7±0.2	1.3±0.1	0.4±0.1									
Grain Boundary	Round	20cw31	-12.7	7.3	650	40.2	46.5	5.1	3.0	1.5	1.6	-									
		Matrix				46.3±0.9	41.2±1.0	4.7±0.3	4.6±0.4	1.9±0.2	1.2±0.1	-									
(Nb,Ti)C	Round	10cw2	-12.7	8.2	650	39.8	26.3	4.4	16.4	2.4	1	-									
Grain Boundary	Round	10cw2	-12.7	8.2	650	40.6	39.1	4.5	4.4	1.9	1.3	-									
		Matrix				41.1±0.7	46.9±0.8	4.7±0.3	4.2±0.4	1.8±0.3	1.2±0.3	-									
Grain Boundary	Round	1A	-12.7	12.3	650	40	38	4.6	4.3	1.6	1.4	-									
		Matrix				46±0.4	42±0.6	4.5±0.6	4.2±0.6	2.1±0.6	1.3±0.2	-									
Grain Boundary	Round	1B	-12.7	4.0	650	41.3	39.2	4.8	3.2	1.2	0.8	-									
		Matrix				46.1±0.3	42.2±0.5	4.6±0.1	4.2±0.4	1.8±0.2	1.1±0.2	-									
Grain Boundary	Flat	21P	-17.4	2.4	750	70.4±3.6	24.1±4.0	2.7±0.5	1.1±0.3	0.8±0.2	-	-									

*Balance Oxygen in Oxide Analyses

niobium and chromium. Enrichment in the other thermodynamically stable elements (Al, Ti, and Si) can also be seen in some of these samples. The sample tested at an oxygen potential of -12.7 kcal/mole shows enrichment of chromium but not niobium.

As seen in Table 3, the grain boundary oxide formed in the -18.7 kcal/mole oxygen potential (650°C, 38 ppm oxygen) flat plate sample is enriched in chromium, relative to the matrix. When comparing the matrix and grain boundary compositions, the elements nickel and iron will appear diluted compared to their matrix compositions. This is because, by combining with oxygen to form oxides, the relative weight percents of these elements at the grain boundaries has decreased. The higher oxygen potential sample, -12.7 kcal/mole, is somewhat enriched in chromium and titanium, but also contains a high nickel content, indicating that the oxide contains a combination of nickel, chromium and titanium. In contrast, the intergranular oxides found in the round bar samples, show no enrichment of chromium relative to the matrix composition. This difference between the two sample geometries may not be related to oxygen concentration. Comparison of equivalent oxygen potentials, -12.7 kcal/mole, still shows more chromium in the flat plate sample. It is more likely that the longer life of the flat plate sample, 28.3 hours versus that of the round bars, allowed Cr_2O_3 , NiCr_2O_4 and/or $\text{Ni}(\text{FeCr})_2\text{O}_4$ to form on the grain boundary. This same time dependency will be shown for the C-ring samples. The presence of an oxidized primary (Nb,Ti)C carbide, at the grain boundary in a round bar sample, can be seen in Table 3. The niobium, and, to a lesser extent, titanium enrichment in this analysis, along with the presence of oxygen, confirms this. The composition of the intergranular oxide found in a 750°C flat plate sample is also shown in Table 3. At this temperature and oxygen potential (195 ppm oxygen), this sample shows predominately nickel enrichment, indicating the formation of a nickel-rich oxide such as NiO under these test conditions.

An activation energy for intergranular oxidation in air was calculated for alloy 908. This calculation was based on measurements of intergranular oxidation depth obtained from round bar test samples used in a prior study. [11] An Arrhenius plot for the air stress rupture data is shown in Figure 37. An activation energy for intergranular oxidation, Q_{gb} , of 202 kJ/mole (48.2 kcal/mole) in air, was calculated from this plot. [14] The value of 908 can be compared with air Q_{gb} values of 280 kJ/mole for Rene'80 by Chang, 274 kJ/mole for Ni 270 by Iacocca, 287 kJ/mole in alloy 718 by Gao, and 335 kJ/mole for a 20Cr-25Ni-Nb stainless steel obtained by Emsley. [33, 38, 89, 90] The lower activation energy obtained for alloy 908 is related to the greater susceptibility of this material to intergranular oxidation in air. A similar analysis was carried out on the flat plate material tested at low oxygen concentrations. [14] The Q_{gb} was calculated to be 492 kJ/mole (118 kcal/mole) in 195 ppm oxygen. A Q_{gb} of 537 kJ/mole (128 kcal/mole) was determined for

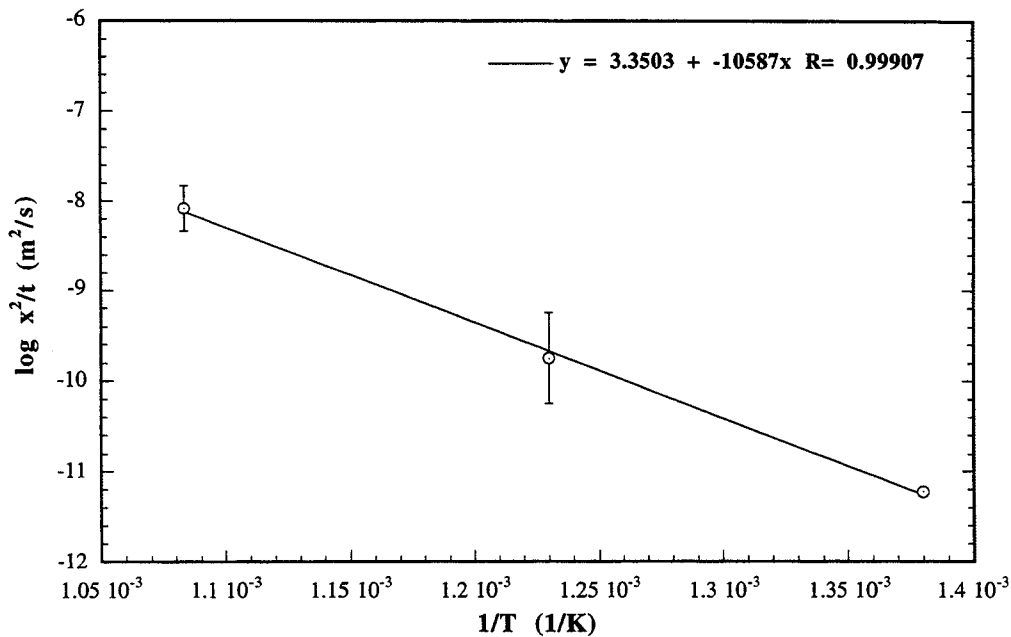


Figure 37. Arrhenius activation energy, Q_{gb} plot for intergranular oxidation in alloy 908 in air. Based on round bar stress rupture data. $Q_{gb} = 202$ kJ/mole (48.2 kcal/mole).

all the flat plate samples in the 38-195 ppm oxygen range. These high values reflect a number of factors. One is that the activation energy for intergranular oxidation at low oxygen concentrations is higher. This is reflected in the longer times required to achieve a given depth of internal/intergranular oxidation as the oxygen concentration is decreased. Another factor is that the flat plate rupture times were relatively constant for all oxygen concentrations. Thus the Arrhenius plots may not reflect the actual time for intergranular oxidation to occur. The time may instead represent a combination of intergranular oxidation and plastic flow by creep.

Modification of Residual Stresses in C-Ring Test Samples

A compilation of the C-ring test results can be seen in Table 4. In this table, failure denotes intergranular cracking through the thickness of the ring. There were no failures among the six shot peened samples tested. Of the four stress relieved samples, none failed, and of the eight solution annealed samples tested, six, or 75%, failed. The crack extends across the width of the C-ring at the apex of its ellipse. When the failed samples are broken open, the cracks can be seen to extend through the entire wall thickness.

Table 4. Alloy 908 C-Ring Test Results at 650°C, 6% Plastic Strain.

Sample Condition	Sample ID	Vacuum (Torr)	Exposure Time (hours)	Failure
Solution Anneal + Bend	S29	3×10^{-2}	24	yes
Solution Anneal + Bend	S37	3×10^{-2}	24	yes
Solution Anneal + Bend + Stress Relieve	S48	4×10^{-2}	24	no
Solution Anneal + Bend + Stress Relieve	S49	4×10^{-2}	24	no
Solution Anneal + Bend + Shot Peen	S13	4×10^{-2}	24	no
Solution Anneal + Bend + Shot Peen	S20	4×10^{-2}	24	no
Solution Anneal + Bend	S26	3×10^{-2}	72	yes
Solution Anneal + Bend	S27	3×10^{-2}	72	yes
Solution Anneal + Bend + Stress Relieve	S47	4×10^{-2}	70	no
Solution Anneal + Bend + Stress Relieve	S50	4×10^{-2}	70	no
Solution Anneal + Bend + Shot Peen	S22	4×10^{-2}	70	no
Solution Anneal + Bend + Shot Peen	S18	4×10^{-2}	70	no
Solution Anneal + Bend	S28	3×10^{-2}	120	yes
Solution Anneal + Bend	S38	3×10^{-2}	120	no
Solution Anneal + Bend	S1	4×10^{-2}	200	yes
Solution Anneal + Bend	S2	4×10^{-2}	200	no
Solution Anneal + Bend + Shot Peen	S16	4×10^{-2}	200	no
Solution Anneal + Bend + Shot Peen	S19	4×10^{-2}	200	no

Shot peening produces a thin layer of compressive residual stress to a depth of about one quarter to one half the shot diameter. [82] No cracking was observed in any of the shot peened samples tested. A comparison of surface cross sections from the three sample types was obtained from metallographic sections taken near the apex of the C-rings. In cross section, the shot peened surface shows a deformed layer of material at the surface (indicated by slip lines within the grains), as can be seen in Figure 38. The deformed surface layer in the shot peened samples did not recrystallize at 650°C. The shot peen size used in this experiment was 63 μm in diameter. The depth of the deformed layer at the surface of these samples was estimated from micrographs of surface cross sections to be 20

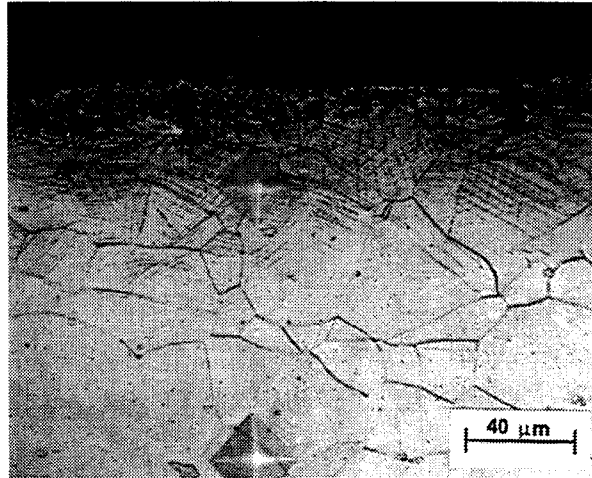
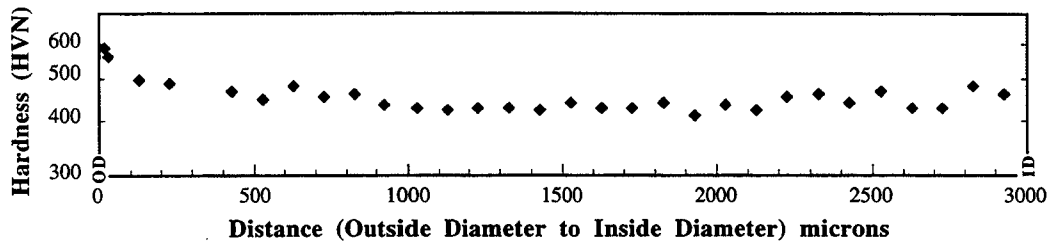


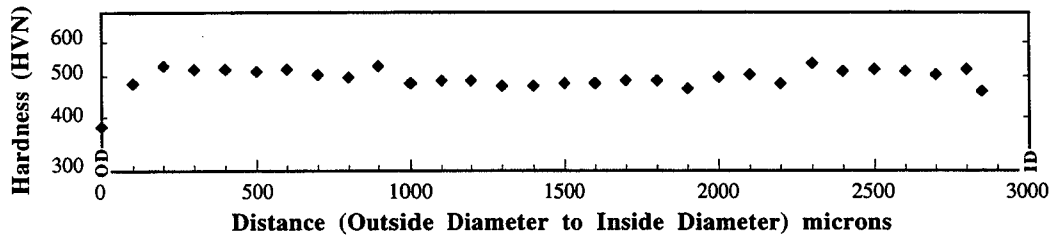
Figure 38. Optical micrograph showing cross section of the outer surface of shot peened sample S13, no failure, showing the 30 μm deep deformed layer caused by shot peening.

to 30 μm deep, approximately one third to one half the shot peen diameter. The maximum compressive stress that can be obtained by shot peening is approximately one-half the material's yield strength. [82] For alloy 908 in the solution annealed condition this value would be approximately -200 MPa.

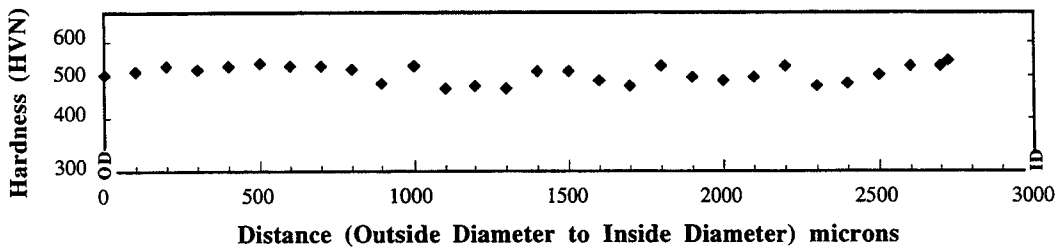
Microhardness traces extending across the entire cross sections of these samples were also obtained and can be seen in Figures 39a, 39b, and 39c. As can be seen from in Figure 39a, the microhardness trace across a shot peened sample shows an increase in hardness in the deformed layer at the surface. The stress relieved sample's microhardness decreases at the surface, shown in Figure 39b, and is consistent with stress relief occurring there. A material can be stress relieved by heating it to a temperature where the yield strength of the material is the same or less than the value of the residual stress.[91] For alloy 908 in the solution annealed condition, this value is approximately 400 MPa at 650°C. At this temperature the material can deform and relieve the stress through creep. It is important to note that the samples used in this study were cooled very slowly after the 650°C/16 hour stress relief heat treatment, and furnace cooling occurred under vacuum. Slow cooling is important so as not to reintroduce residual stresses. The microhardness trace across the solution annealed and failed sample is shown in Figure 39c and shows no change in subsurface hardness. The results of the C-ring tests indicate that the elimination or reduction of the tensile residual stress component contributing to intergranular oxidation was responsible for preventing intergranular cracking.



a. Shot Peened



b. Stress Relieved



c. Solution Annealed

Figure 39. Microhardness profiles across thicknesses of C-ring samples (a) S13 shot peened, (b) S49 stress relieved, and (c) failed solution annealed C-ring S37.

Another factor, that can explain these results exists. Researchers have observed that changes in the surface stress state can alter the type of oxide formed. Shot peening produces chromium rich spinels versus (Fe,Ni)O type oxides. [17, 53, 54, 92] Improved oxidation resistance of shot peened materials has also been observed. [92] Surface deformation was reported to enhance Cr₂O₃ formation in Ni-Cr alloys containing between 10 and 30 wt.% chromium. [85] Giggins, et al., attributed this to the fine grain size produced by recrystallization of deformed surface layers at 900 and 1100°C. [85] Finer grain size produces more grain boundary/surface intersections from which Cr₂O₃ can spread, as illustrated in Figure 4. Reports of enhanced chromium-rich oxide formation that occurs in superalloys and stainless steels after shot peening appear to support this conclusion. [53, 92] To determine whether this had occurred in the shot peened material, chemical analyses were conducted on oxides electrolytically extracted from the surfaces of the C-rings. Shot peened, stress relieved, failed solution annealed and intact solution annealed samples were analyzed. The results of these analyses are shown in the plot seen in Figure 40. The bars indicate the ratio of the atomic percent of a particular element to the other elements in the extracted oxide.

The ratio of chromium present in the surface oxide extracted from the shot peened samples increased after 70 hours of exposure time. The ratio of aluminum present in the oxide also increased after 70 hours. At 24 hours, iron and nickel are the primary constituents in the oxides extracted from the shot peened and stress relieved samples. This is consistent with the rapid kinetics of (Ni,Fe)O oxide formation as opposed to that of Cr₂O₃ and its spinels. The oxide formed on the stress relieved sample after a 70 hour exposure showed higher ratios of aluminum and silicon in its oxide than did the oxide from the stress relieved material after a 24 hour exposure. The relative ratios of chromium present remained the same for both exposures. From these analyses it appears that the oxide(s) formed on the shot peened samples do become enriched in chromium, but only after a 70 hour exposure. No chromium enrichment was observed in the sample exposed for 24 hours. Neither stress relieved oxide exhibited chromium enrichment. It was initially thought that the stress relieved samples may have formed a chromium-rich oxide during their high vacuum heat treatment. And that this contributed to the fracture resistance seen in these samples. This supposition is not confirmed by these results. In fact, both the shot peened and stress relieved samples, exposed for 24 hours, developed oxides with very similar compositions.

In contrast, the oxide from one of the failed 24 hour samples consisted primarily of aluminum, with lesser but nearly equivalent ratios of niobium, chromium, and titanium. Interestingly, the oxide extracted from the solution annealed sample exposed for 200 hours

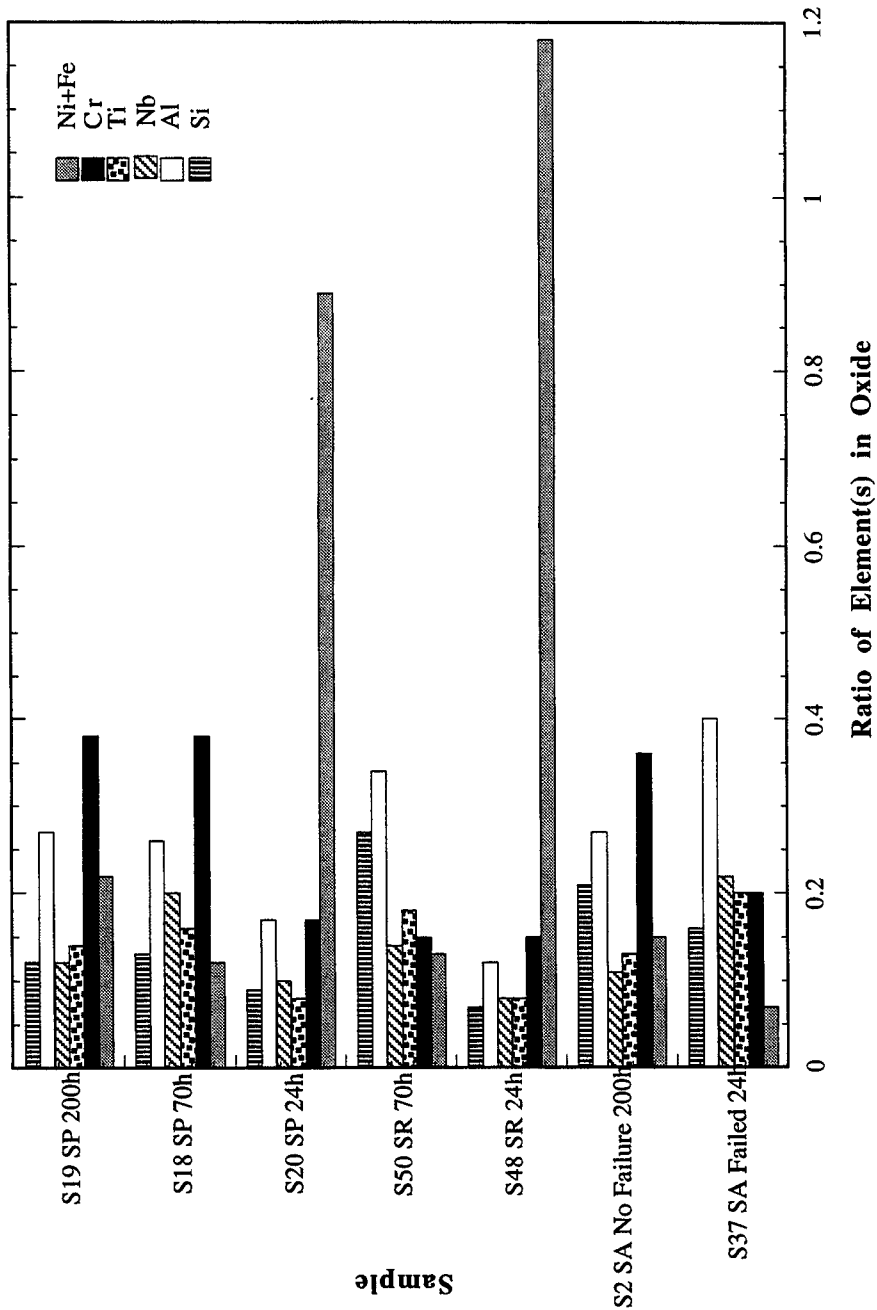
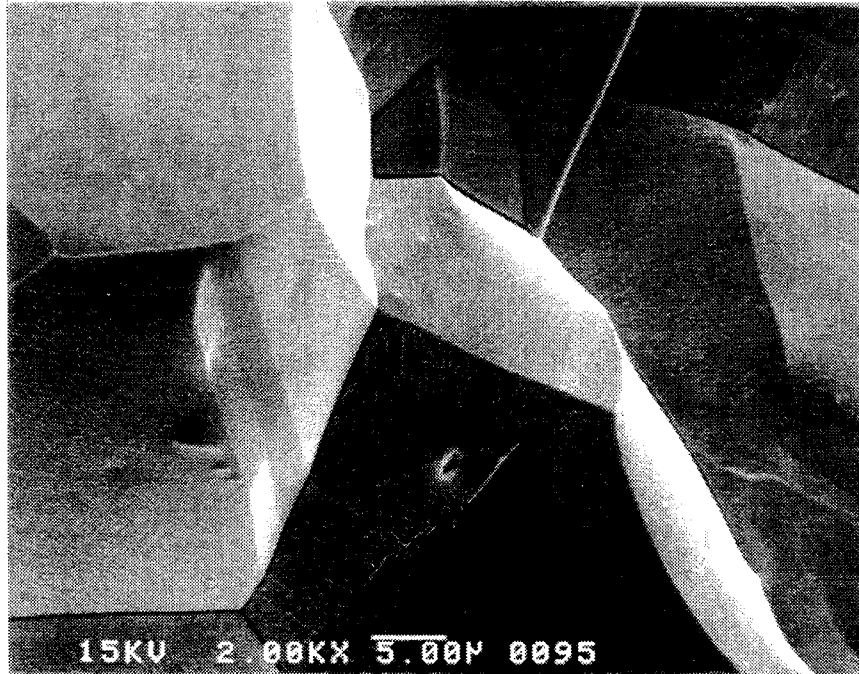


Figure 40. Ratios of elements present (balance oxygen) in oxides electrolytically extracted from the surfaces of C-ring s that were heat treated under degraded vacuum conditions (10^{-2} Torr range). SA = Solution Annealed, SR = Stress Relieved, and SP = Shot Peened.

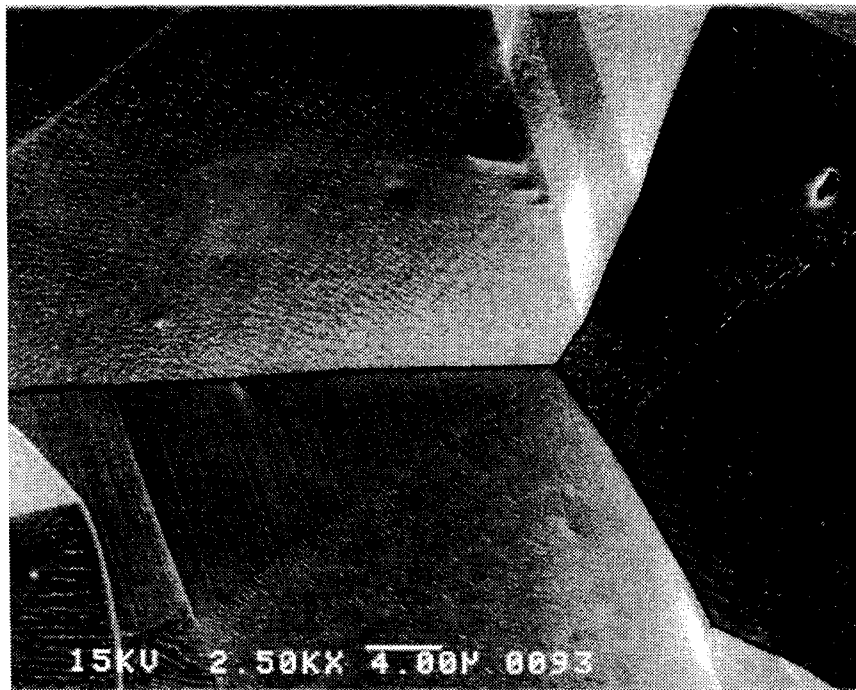
that did not fail had chromium and aluminum ratios that were similar to the long time exposure shot peened samples. The oxides formed on the shot peened surfaces, after 70 and 200 hour exposures, had relatively high ratios of chromium. The oxide formed on the shot peened material exposed for 24 hours did not, however, contain significantly more chromium than either the stress relieved or the failed solution annealed materials. Based on these results, the oxides present on the stress relieved and shot peened material are not sufficiently enriched in chromium after 24 hours to have provided any significant protection against stress assisted intergranular oxidation. This is when compared to the failed solution annealed material. Solution annealed samples that did not fail, and were exposed for long times (200 hours) showed similar increases in the ratio of chromium in their surface oxides.

For the shot peened and stress relieved samples it is more plausible that the elimination or reduction in residual surface tensile stresses acts directly to prevent failure. This is because the beneficial effect of shot peening came in the short term (24 hour exposure), where no substantial chromium enrichment was observed.

Examination of the fracture surfaces from the failed C-ring revealed fine structure in the SEM that was obscured by oxidation in the stress rupture samples. Higher magnification micrographs show the intergranular fracture surface to be brittle in character, with no evidence of ductility on the surfaces of the exposed grain boundaries, as shown in Figures 41a and 41b. Slip lines and twin boundaries can be seen very clearly on the grain surfaces in these micrographs. Their appearance is enhanced due their decoration by small white particles. At high magnification in the SEM, there was no variation in the density of these particles or fracture surface oxidation between the outside diameter and inside diameter of the sample. These particles and their association with slip lines in the material can be seen in Figures 42a and 42b. The high magnification micrograph seen in Figure 42b clearly shows the decoration of slip lines by these particles. In situ EDS analyses showed oxygen present in the particles but the concentrations of the other elements were at matrix levels. This result suggests that the particles have compositions that contain the two major matrix elements, i.e., nickel and iron, and have a stoichiometry close to the proportion of these elements in the matrix. The tenacity of these oxide particles precluded their removal by mechanical extraction using polymeric microscopy replicating film for ex-situ EDS analysis. C-ring experiments similar to these had been previously performed in commercial grade argon, and the fracture surfaces from these samples had shown fracture morphologies with similar decoration of slip lines as the degraded vacuum samples used in this study. The particles present on the argon tested samples were coarser, however, and could be extracted from the surface using polymeric surface replicating film. Semi-

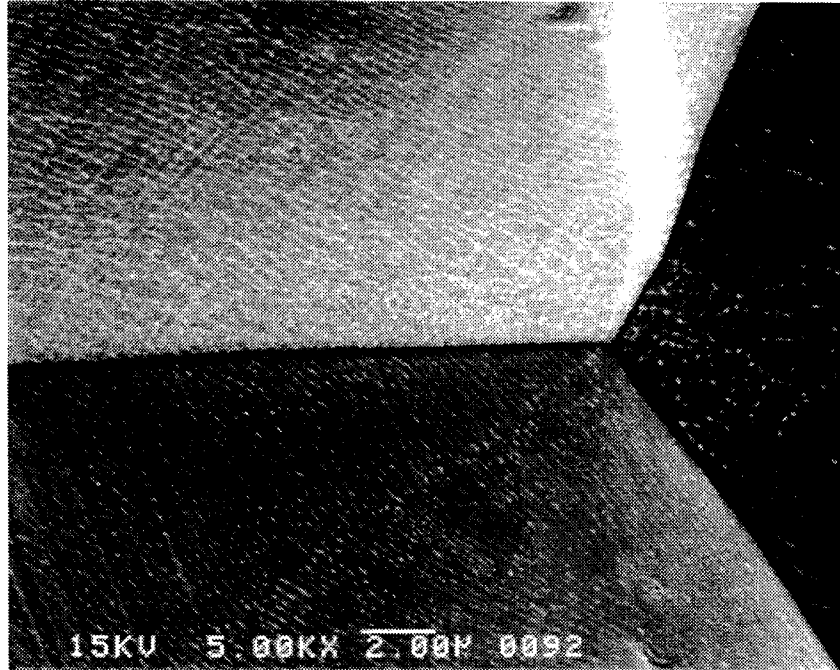


a

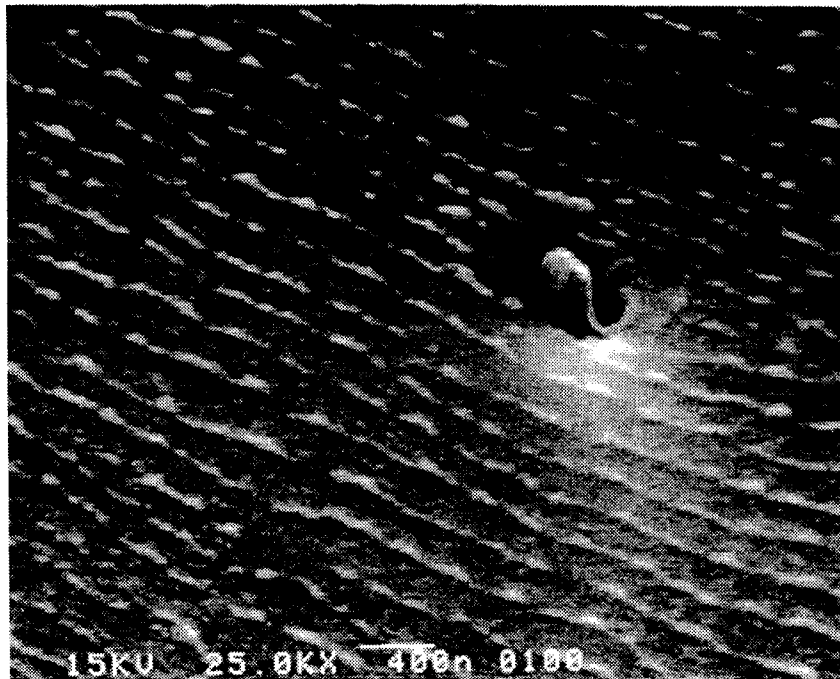


b

Figure 41. High magnification SEM micrographs taken near the inside diameter of the cracked cross section of C-ring S37 after failing within 24 hours at 650°C in a 4×10^{-2} Torr vacuum.



a



b

Figure 42. High magnification SEM micrographs taken along the cracked cross section of C-ring S37 after failing within 24 hours at 650°C in a 4×10^{-2} Torr vacuum. (a) Near inside diameter. (b) Near outside diameter.

quantitative EDS analyses were obtained from multiple extracted particles. The resulting composition, in weight percent, was determined to be $38.7 \pm 5\%$ Fe, $39 \pm 5.8\%$ Ni, and $21 \pm 6\%$ O. To determine an approximate stoichiometry the atomic percent of these elements was $26 \pm 5\%$ Fe, $25 \pm 6\%$ Ni, and $47.7 \pm 9.9\%$ O, giving a compound with the formula (Ni,Fe)O. Interestingly this is the same oxide stoichiometry reported by Andrieu to be present in the intergranular cracking regime of alloy 718. [53, 54, 55]

SUMMARY OF RESULTS

- Stress is a required component for intergranular oxidation under the temperature/oxygen conditions examined.
- Time to failure generated by stress rupture testing is not a reliable indicator of intergranular oxidation cracking.
- While a significant increase in rupture life is evident between air and low ppm oxygen atmospheres, less significant divisions in rupture life occur within the low oxygen concentration data.
- Changes in the depth of intergranular oxidation can be correlated with changes in oxygen concentration.
- The oxygen concentration threshold for intergranular oxidation is 0.1 ppm, based on the percentage of intergranular fracture versus oxygen concentration results.
- The initial (< 24 hours) oxides present on the intergranular fracture surfaces are (Ni,Fe)O type.
- The amount of chromium present in the intergranular oxide increases as the terminus of the depth of intergranular oxidation is approached.
- Placing the surface in a compressive state of stress, or relieving tensile stresses mitigates the effect of oxygen on intergranular oxidation.
- Intergranular oxidation proceeds to a depth that is a function of the exposure time and oxygen concentration. For the stress rupture test, the exposure time (rupture life) is a combined function of both creep and intergranular oxidation cracking.

ANALYSIS OF STRESS ACCELERATED GRAIN BOUNDARY OXIDATION

The transition from external to internal oxidation is of relevance to this study since it links the effects of changes in oxygen partial pressure to intergranular oxidation. According to Rapp, the transition from internal to external oxidation is a passivation process. [59] In the case of internal/intergranular oxidation, the reaction proceeds until sufficient intergranular oxide precipitates form to block further reaction between oxygen atoms and solute atoms. [59] Rapp demonstrated the effect of oxygen partial pressure on the external to internal oxidation transition in his experiments on Ag-In alloys. [59] In these experiments he varied both the concentration of the internal oxidant indium and the partial pressure of oxygen. His results are shown in Figure 43. The effect of decreasing the partial pressure of oxygen and increasing the mole fraction of internal oxidant can be seen in this figure as promoting external oxidation or passivation. Based on these results Rapp suggested that preheat treatment of structural alloys at reduced oxygen partial pressures will produce a passivating external scale. [59] These results have been applied to Ni-Cr alloys. Wood, et. al., found that Ni-Cr alloys with higher chromium contents underwent a more rapid transition from internal/intergranular oxidation to external oxidation. [67] The oxygen partial pressure at the surface is also important. As the concentration of oxygen is decreased, a critical value is reached at which a transition from internal to external oxidation occurs. [67]

It is proposed that stress accelerated grain boundary oxidation can be described using Rapp's internal oxidation model. In stress accelerated grain boundary oxidation, low temperatures ($<800^{\circ}\text{C}$) and application of tensile stress, favor grain boundary diffusion over lattice diffusion. The result is internal/intergranular oxidation that follows the internal/matrix oxidation model. The assumptions that serve as the basis of this proposed mechanism are:

- Intergranular oxidation in stress rupture samples continues until the sample fails, i.e., until final fast ductile fracture. [14]
- At low temperatures ($< 800^{\circ}\text{C}$), and under an applied tensile stress, grain boundary diffusion is greater than lattice diffusion ($D_{\text{lattice}} \lll D_{\text{gb}}$).
- At low temperatures and under tensile stress the intergranular oxidation zone penetrates to the same depth as predicted for internal oxidation. Because $D_{\text{lattice}} \lll D_{\text{gb}}$, no internal (matrix) oxidation occurs.

- Analogous to internal (matrix) oxidation, the transition from internal to external oxidation is promoted by lowering the surface oxygen concentration and/or increasing the chromium concentration in the alloy.
- Also analogous to internal oxidation in Ni-Cr alloys, the nucleation and growth of intergranular Cr_2O_3 and NiCr_2O_4 type oxides precipitate and serve to block the diffusion path for oxygen.
- The external oxide layer formed at the low oxygen concentrations (≤ 1000 ppm) used in these experiments was thin ($< 0.2 \mu\text{m}$) or incomplete. Also, tensile loading will rupture this external oxide layer. Based on these observations, it can be assumed that diffusion through the external scale is not rate limiting. This allows the problem to be treated as internal oxidation in the absence of an external scale.

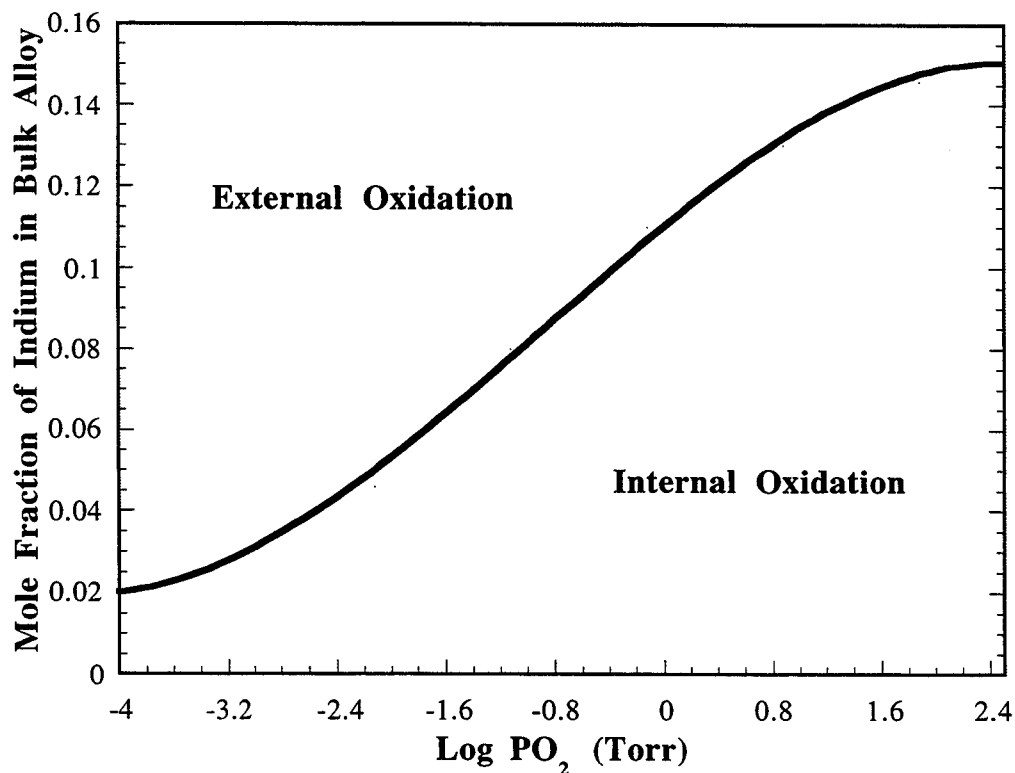


Figure 43. Transition from internal to external oxidation for Ag-In alloys at 550°C. From Rapp. [59]

Definition of terms:

- $N_{cr}^{(0)}$ is the mole fraction of chromium in the alloy.
- $N_o^{(s)}$ is the mole fraction of oxygen at the surface.
- N_o is the mole fraction oxygen in the base metal.
- N_{Cr} is the mole fraction of chromium.
- D_o is the diffusion coefficient for oxygen.
- D_{cr} is the diffusion coefficient for chromium.
- D_{gb}^o is the grain boundary diffusion coefficient for oxygen.
- D_{gb}^{Cr} is the grain boundary diffusion coefficient for chromium.
- v is the stoichiometric ratio of oxygen to metal atoms in the oxide precipitate.
- ξ is the depth of the zone of internal oxidation.
- x is the distance from the outer surface.
- t is the reaction time required to form an internal oxide zone of depth ξ .
- γ is a time-independent dimensionless parameter, for isothermal oxidation at constant oxygen pressure.

The following derivation for the depth of internal oxidation follows that of Rapp. [59] Under diffusion control and in the absence of an external scale, the depth of the internal oxidation zone is a parabolic function of time, is given by,

$$\xi = 2\gamma(D_o t)^{1/2}. \quad [59] \quad (2)$$

Rapp has solved the one-dimensional diffusion equations for oxygen and for some oxidizable alloying element, in this case chromium. For oxygen,

$$\frac{\partial N_o}{\partial t} = D_o \frac{\partial^2 N_o}{\partial x^2} \quad (3)$$

the boundary conditions used are

$$\begin{aligned} N_o &= N_o^{(s)} & \text{for } x = 0, t > 0 \\ N_o &= 0 & \text{for } x \geq \xi, t > 0. \end{aligned}$$

For chromium the diffusion equation is,

$$\frac{\partial N_{Cr}}{\partial t} = D_{Cr} \frac{\partial^2 N_{Cr}}{\partial x^2} \quad (4)$$

and the boundary conditions applied are

$$\begin{aligned} N_{Cr} &= N_{Cr}^{(0)} & \text{for } x > 0, t = 0 \\ N_{Cr} &= 0 & \text{for } x \leq \xi, t > 0. \end{aligned}$$

The solutions obtained by Rapp are

$$N_O = N_O^{(S)} \left\{ 1 - \frac{\text{erf}[x/2] (D_O t)^{1/2}}{\text{erf } \gamma} \right\} \quad (5)$$

$$N_{Cr} = N_{Cr}^{(0)} \left\{ 1 - \frac{\text{erfc}[x/2] (D_{Cr} t)^{1/2}}{\text{erf } \gamma \phi^{1/2}} \right\}. \quad (6)$$

In these equations $\phi = D_O/D_{Cr}$.

If an insoluble and stoichiometric oxide precipitates at the front of the zone of internal oxidation, the flux of oxygen atoms arriving from the surface must be equivalent to the flux of chromium arriving from the bulk alloy and,

$$\lim_{\epsilon \rightarrow 0} \left[-D_O \left(\frac{\partial N_O}{\partial x} \right)_{x=\xi-\epsilon} = -v D_{Cr} \left(\frac{\partial N_{Cr}}{\partial x} \right)_{x=\xi+\epsilon} \right]. \quad (7)$$

Substituting equations (5) and (6) into equation 11 gives

$$\frac{\partial N_O}{\partial t} = \frac{\exp(\gamma^2) \text{erf } \gamma}{\phi^{1/2} \exp(\gamma^2 \phi) \text{erfc}(\gamma \phi^{1/2})}. \quad (8)$$

Rapp obtained a solution for γ for the case where,

$$\frac{D_{Cr}}{D_O} \ll \frac{N_O^{(S)}}{N_{Cr}^{(0)}} \ll 1 \quad (9)$$

which is shown graphically in Figure 44. [59] This simplifies equation (8) to

$$\gamma \cong \left[\frac{N_O^{(S)}}{2 v N_{Cr}^{(0)}} \right]^{1/2}. \quad (10)$$

Finally, substituting the expression for γ into equation (2) gives an expression for the depth of internal oxidation,

$$\xi \cong \left[\frac{2 N_O^{(S)} D_O t}{v N_{Cr}^{(0)}} \right]^{1/2}. \quad (11)$$

The validity of the condition stated in equation (9) and illustrated in Figure 44 can be verified for the formation of an intergranular oxidation zone of depth ξ . The micrograph shown in Figure 45 is from a cross section near the surface of a heat treated alloy 905

sample. This material has no chromium and low aluminum concentration. The intergranular and surface oxides that form in this material have been identified as Nb₂O₅. [1] Extended time heat treatments rapidly overage the γ' (bct Ni₃Nb) precipitate in this material. [1] This and the prevalence of niobium in this phase, lends itself to using the γ' as a marker for niobium distribution using SEM. Coarse platelets of γ' can be seen in the lower portion of the micrograph and oxide precipitates can be seen along the grain boundaries. As the surface oxide develops, the intergranular oxidation zone extends into the alloy and the depletion of niobium from the matrix can be seen as a zone denuded of coarse γ' . As illustrated, the intergranular oxidation zone penetrates to the same depth as the solute depleted zone in this material. At low temperatures (< 800°C), the chromium concentration at the front of internal oxidation in Ni-Cr alloys has been shown to behave similarly. [67]

For the conditions used in these experiments, the mole fraction of chromium, $N_{cr}^{(o)}$, is fixed at 0.045. The concentration of oxygen at the surface of the stress rupture samples was measured and, from Sievert's law, $N_o^{(s)} \propto (P_{O_2})^{1/2}$. For Cr₂O₃ forming as an intergranular oxide $\nu = 3/2$. If grain boundary diffusion dominates under conditions at which stress accelerated grain boundary oxidation occurs, then equation (11) becomes

$$\xi \cong [29.6 N_o^{(s)} D_{gb}^o t]^{1/2} \quad (12)$$

A value for the grain boundary diffusion of oxygen, D_{gb}^o , can be estimated for alloy 908 from

$$D_{gb} = 1.0 \exp\left(-9.35 \frac{T_m}{T}\right) \text{cm}^2\text{s}^{-1}; 1.0 < T_m/T < 2.4. \quad [65] \quad (13)$$

For alloy 908 at 650°C, $T_m/T = 1.77$, and $D_{gb} = 6.5 \times 10^{-8} \text{cm}^2\text{s}^{-1}$. The depth of intergranular oxidation in the flat plate material was calculated as a function of surface oxygen concentration and experimental test time using equation (12). Intergranular oxidation depths for the round bar material were calculated using an analogous equation derived for cylindrical samples

$$\frac{(r_1)^2}{2} - (r_2)^2 \ln\left(\frac{r_1}{r_2}\right) + \frac{1}{2} = \frac{2N_o^{(s)} D_{gb}^o}{\nu N_{Cr}^o} t \quad (14)$$

where r_1 is the sample radius and r_2 is the un-oxidized core radius. [69] The values

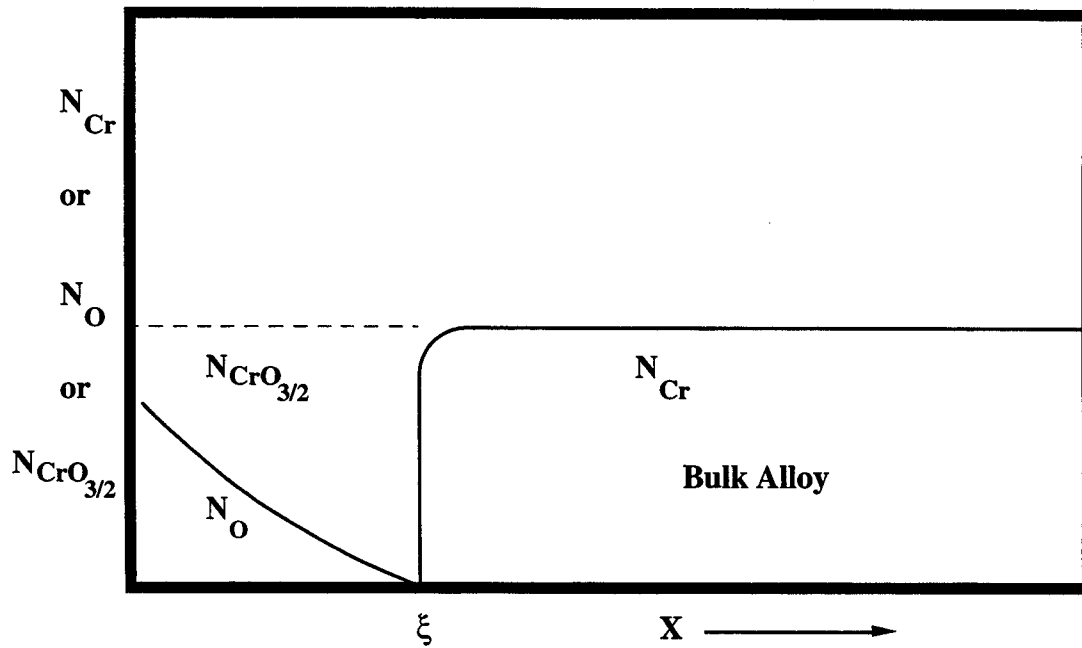


Figure 44. Concentration profile for the exclusive internal oxidation of alloys for the case

where $\frac{D_{Cr}}{D_O} \ll \frac{N_O^{(s)}}{N_{Cr}^{(s)}} \ll 1$. From Rapp. [59]

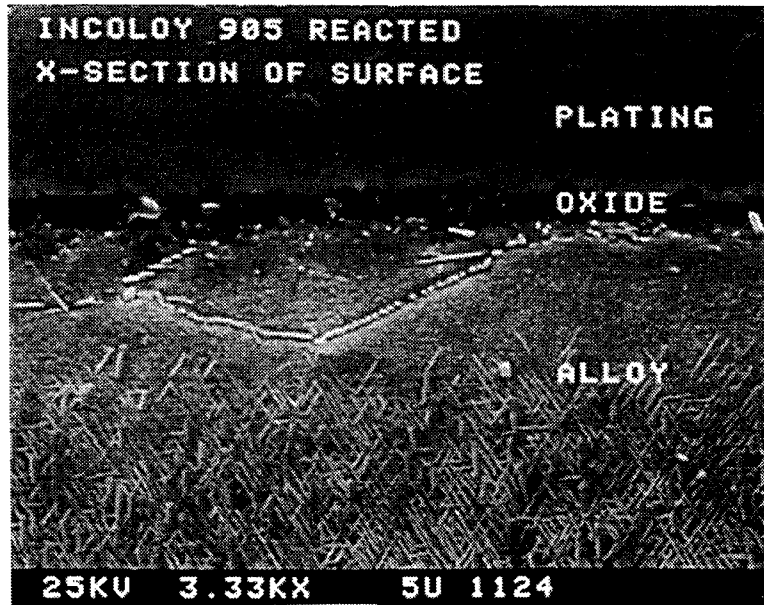


Figure 45. SEM micrograph showing cross section through the oxidized surface of heat treated alloy 905.

obtained were plotted with the experimental measurements of intergranular oxidation depth and are shown in Figure 46. The calculated values follow the trend of the experimental values. At low oxygen concentrations the depth of intergranular oxidation is at or near zero. This is the point at which the external/intergranular transition occurs. The depth of intergranular oxidation then increases as the concentration of oxygen at the surface increases. Above 1000 ppm oxygen the assumption that an external oxide layer is not present is no longer valid and diffusion through the external oxide is rate limiting. Under these conditions the second plateau in the sigmoidal curve develops. A schematic of the intergranular oxidation zone, of depth ξ , developed under tensile loading, is shown in Figure 47. Following internal oxidation theory, the intergranular oxidation zone stops at depth ξ after sufficient oxide (Cr_2O_3 or NiCr_2O_4) has precipitated to block further diffusion of oxygen. The time required to produce a 0.5 mm deep zone of intergranular oxidation in alloys 718, 908, and 903, as a function of oxygen concentration, are compared in Figure 48. As evident in this figure, increasing $N_{\text{cr}}^{(o)}$ increases the time required to attain the same depth of intergranular oxidation. The higher activation energy calculated for intergranular oxidation at low oxygen concentrations is reflected in Figure 48. The time required to form a 0.5 mm zone of intergranular oxidation is longer at low oxygen concentrations than in air. This indicates that a greater barrier to intergranular oxidation exists under low oxygen conditions. As discussed above, the barrier to intergranular oxidation below 1 ppm oxygen is related to the transition from intergranular to external oxidation. A comparison to Figure 48 shows why the percent intergranular fracture in alloy 908 lies above the alloy 718 data. It is expected that under equivalent loading conditions, alloy 908 will show greater a intergranular oxidation depth (and percent intergranular fracture) than alloy 718.

Translated to fatigue loading, for a fixed oxygen concentration, da/dN will be greater in the lower $N_{\text{cr}}^{(o)}$ alloys. This is because the depth of intergranular oxidation developed ahead of the crack tip will be greater. As the grain boundary area increases the effects of intergranular oxidation on da/dN should also increase. The increase in da/dN in alloy 718, under intergranular oxidation conditions, with decreasing grain size has been demonstrated in alloy 718. [24] Due to rupture of the external scale during crack advance the assumption that an external oxide is absent exists during fatigue loading.

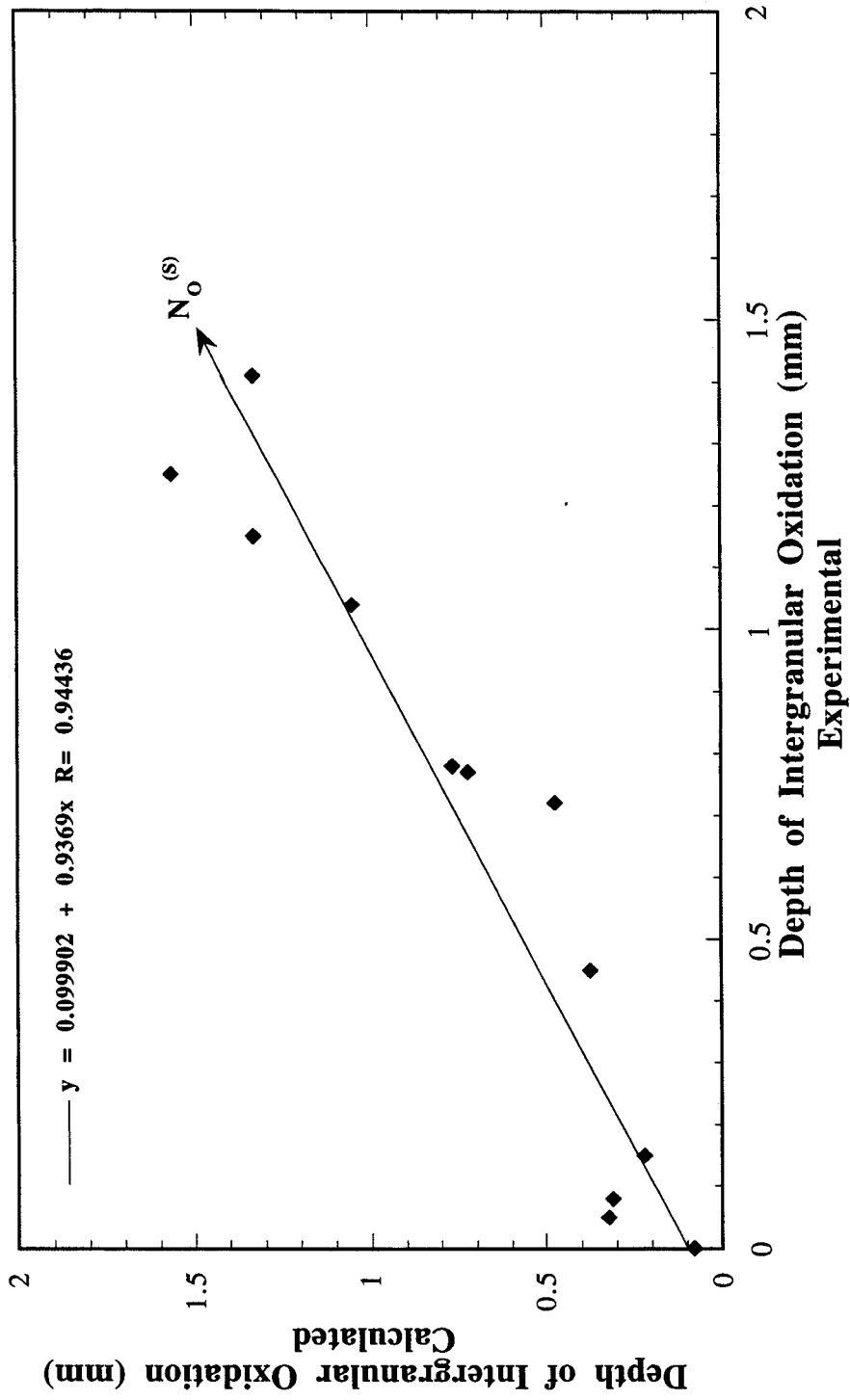


Figure 46. Comparison of experimental and calculated intergranular oxidation depths as a function of surface oxygen concentration at 650°C and 650 MPa. Based on experimental time to failure of stress rupture samples.

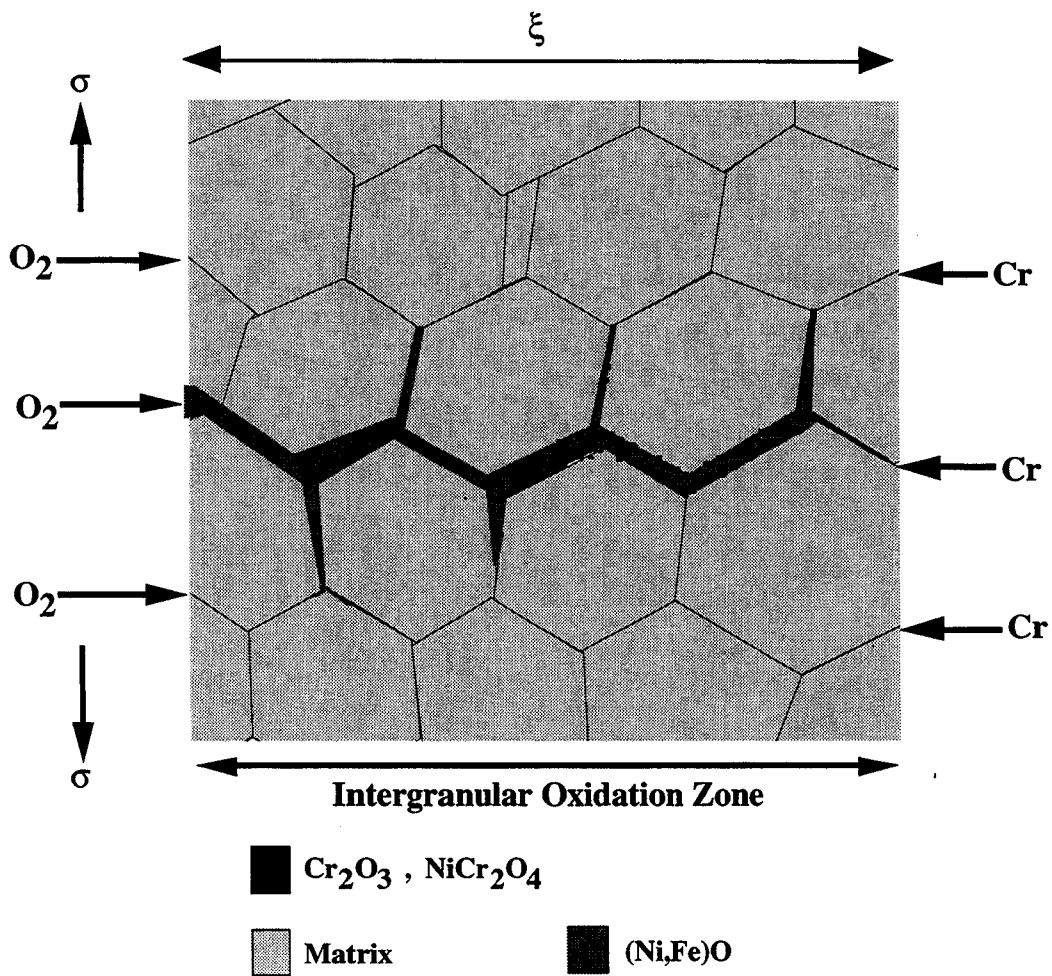


Figure 47. Intergranular oxidation zone (of depth ξ) developed under tensile loading.

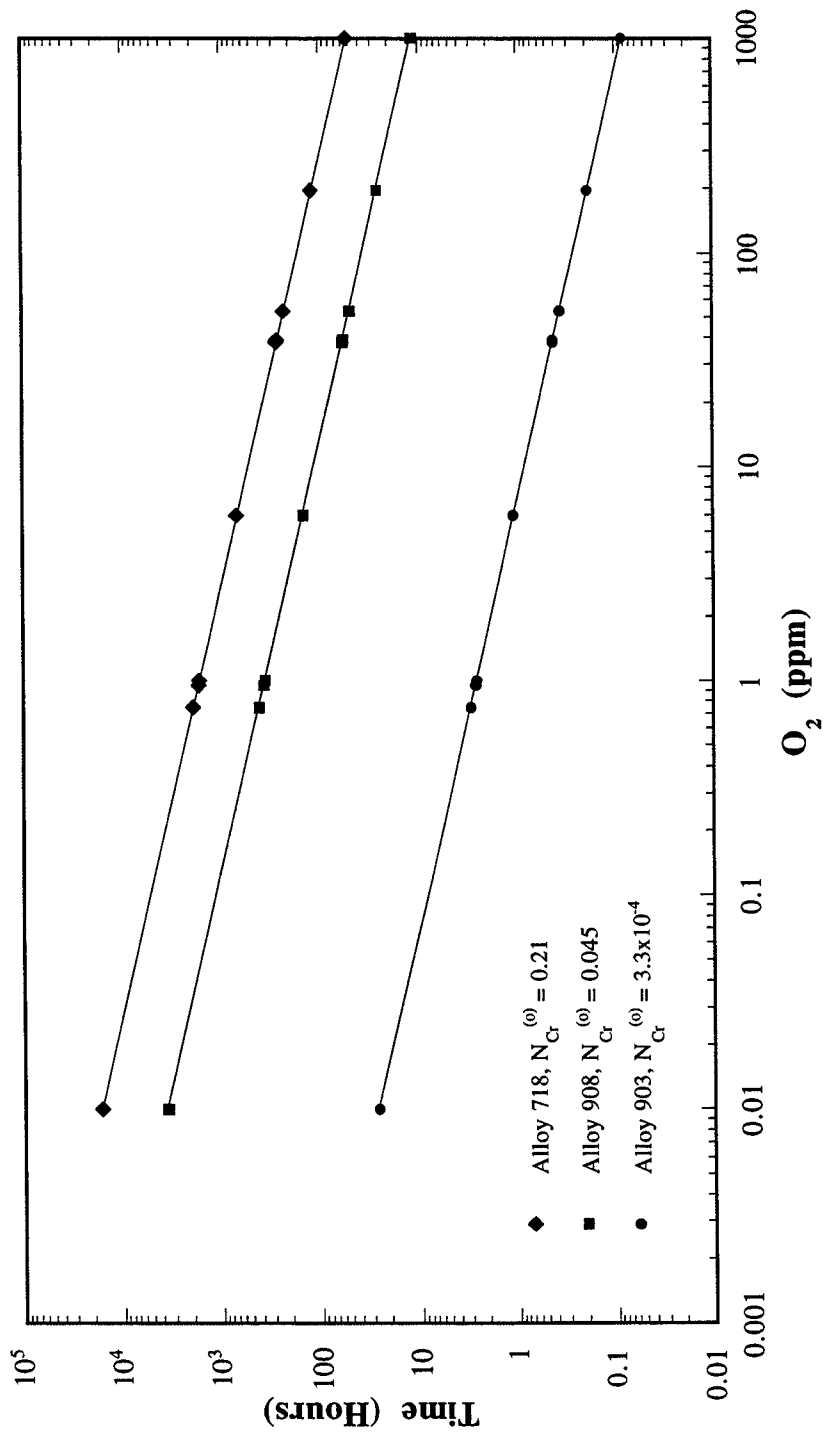


Figure 48. Time to develop a 0.5 mm deep zone of internal oxidation in three alloys at 650°C as a function of oxygen concentration and mole fraction Cr.

CONCLUSIONS

Stress Accelerated Grain Boundary Oxidation As Internal Oxidation

- The mechanism for high temperature intergranular fracture in alloy 908 is stress assisted intergranular oxidation.
- Intergranular oxidation in alloy 908, at low temperatures (550 - 800°C), requires an applied or residual tensile stress to occur.
- Long range, intergranular oxygen embrittlement is not present in alloy 908.
- The fact that non-stressed material used in these experiments did not exhibit intergranular oxidation supports the proposal that tensile stresses are required for intergranular oxidation.
- Under an applied or residual tensile stress, the depth of intergranular oxidation in alloy 908 increases with increasing oxygen concentration.
- The intergranular oxidation zone penetrates to the same depth as calculated for internal oxidation with $D = D_{gb}^0$. Because $D_{lattice} \lll D_{gb}$, no internal (matrix) oxidation occurs.
- The transition from internal to external oxidation is promoted by lowering the surface oxygen concentration and/or increasing the chromium concentration in the alloy.
- Analogous to internal oxidation in Ni-Cr alloys, the nucleation and growth of intergranular Cr_2O_3 and $NiCr_2O_4$ precipitates serves to block the diffusion path for oxygen.
- This result can be correlated to that observed in other Ni-Fe and Ni base superalloys and is controlled both by the concentration of oxygen in the environment and the concentration of chromium in the alloy.
- The internal oxidation model for high temperature intergranular cracking can be applied to other metals that exhibit a similar dependency on oxygen concentration.
- This failure mechanism's dependence on alloy chromium concentration is similar that of stress corrosion cracking encountered in aqueous environments.

Stress Accelerated Grain Boundary Oxidation Applied

- Control of furnace atmosphere chemistry during heat treatment is essential to the successful heat treatment of alloy 908.
- An oxygen concentration of **below 0.1 ppm** is required to heat treat alloy 908 **under applied or residual tensile stresses**.
- For stress rupture testing, an oxygen concentration threshold based on zero percent intergranular fracture is a better indicator of the potential for intergranular fracture during heat treatment than one based on time to rupture.
- No difference in stress rupture behavior was observed between the 10 and 20% cold work starting conditions. The solution annealed starting condition showed an improvement in stress rupture life compared to either of the cold worked starting conditions.
- The elimination of residual tensile surface stresses by applying compressive residual stresses through shot peening or reduction in tensile stresses through vacuum stress relief heat treatments eliminates stress assisted grain boundary oxidation.

REFERENCES

1. M.M. Morra, "Alloy 908, A New High Strength, Low Coefficient of Thermal Expansion Alloy for Cryogenic Applications", S.M. Thesis, Massachusetts Institute of Technology, February 1989
2. M.M. Morra, R.G. Ballinger, J.L. Martin, M.O. Hoenig, and M.M. Steeves, "Incoloy® 9XA, A New Low Coefficient of Thermal Expansion Sheathing Alloy for Use in ICCS Magnets", Advances in Cryogenic Engineering Materials, Vol. 34, A.F. Clark and R.P. Reed, eds., 1987, pp 157-164
3. M.M. Morra, R.G. Ballinger, and I.S. Hwang, "Incoloy® 908, A Low Coefficient of Expansion Alloy for High Strength Cryogenic Applications: Part 1-Physical Metallurgy", Met.Trans. A, December 1992, pp. 3177-3192
4. C.H. Jang, "Weld Development for Incoloy Alloy 908, A Low Thermal Expansion Superalloy", Ph.D. Thesis, Massachusetts Institute of Technology, January 1995
5. S.K. Hwang, F.C. Hull and J.M. Wells, "Thermal Expansion of Alloys Used in Power Generation", EPRI RD-3685, Project 2426-1, September 1984
6. H. Fujimori, "Thermal Expansion and Magnetovolume Effects of Invar Alloys", Physics and Applications of Invar Alloys, Part II, Honda Memorial Series on Materials Science, No. 3, Maruzen Company, LTD, Tokyo, 1978, pp. 80-96
7. S.K. Hwang, F.C. Hull and J.M. Wells, "Effects of the Alloying Elements on the Thermal Expansion Coefficients of Non Magnetic Ni-Base Alloys and Austenitic Steels", Superalloys 1984, Proc. 5th Int. Sym. on Superalloys, Seven Springs, PA, ASM, Metals Park, OH, 1984, pp. 785-794
8. D.F. Smith, E.F. Clustworthy, D.G. Tipton, and W.L. Mankins, "Improving the Notch-Rupture Strength of Low-Expansion Superalloys", Superalloys 1980, Proc. 4th Int. Sym. on Superalloys, Seven Springs, PA, ASM, Metals Park, OH, 1980, pp. 521-530
9. K. Sato and T. Ohno, "Development of Low Thermal Expansion Superalloys", Superalloys 1992, Proc. 7th Int. Sym. on Superalloys, Seven Springs, PA., ASM Metals Park, OH, 1992, pp. 247-255
10. E.A. Wanner and D.A. DeAntonio, "Development of A New Controlled Thermal Expansion Superalloy with Improved Oxidation Resistance", Superalloys 1992, Proc. 7th Int. Sym. on Superalloys, Seven Springs, PA, ASM, Metals Park, OH, 1992, pp. 237-246
11. S. Nicol, "Stress-Rupture Properties of Incoloy 908 in Air", B.S., M.E. Thesis, Worcester Polytechnic Institute, July 1993
12. T.M. Anandan, J.A. Lewis, and M.M. Steeves, "Complex vacuum HT cycle turns coil into superconductor", Heat Treating, September 1990, pp. 28-29

13. M.M. Steeves, T.A. Painter, M. Takayasu, R.N. Randall, J.E. Tracey, I.S. Hwang, and M.O. Hoenig, "The US Demonstration Poloidal Coil, IEEE Trans. Mag., Vol. 27, No. 2, March 1991, pp. 2369-2372
14. M.M. Morra, "Stress Accelerated Grain Boundary Oxidation of Incoloy Alloy 908 in High Temperature Oxygenous Atmospheres", Sc.D. Thesis, Massachusetts Institute of Technology, June 1995
15. T. Ericsson, "Review of Oxidation Effects on Cyclic Life At Elevated Temperature", Canadian Met. Quarterly, Vol. 18, 1979, pp. 177-195
16. M. Gell and D.J. Duquette, "The Effects of Oxygen on Fatigue Fracture of Engineering Alloys", Corrosion Fatigue: Chemistry, Mechanics and Microstructure, A.J. McEvily and R.W. Stuehle, NACE, Houston, TX, 1972, pp. 366-378
17. A. Pineau, "Elevated-Temperature Creep-Fatigue Cracking Interactions in Relation to Oxidation Effects", Nace 10, EICM Proceedings, pp 111-122
18. F.E. Fujita, "Oxidation and Dislocation Mechanisms in Fatigue Crack Formation", Fracture of Solids, Vol. 20, D.C. Drucker and J.J. Gilman, eds., Interscience Publishers, 1963, pp. 657-670
19. R.M.N. Pelloux, "Mechanisms of Formation of Ductile Fatigue Striations", Trans. ASM, Vol. 62, 1969, pp. 281-285
20. H.H. Smith and P. Shahinian, and M.R. Achter, "Fatigue Crack Growth Rates in Type 316 Stainless Steel at Elevated Temperature as a Function of Oxygen Pressure", Trans. Met. Soc. of AIME, Vol. 245, May 1969, pp. 947-953
21. M.R. Achter, G.J. Danek, Jr., and H.H. Smith, "Effect on Fatigue of Gaseous Environments Under Varying Temperature and Pressure", Trans. Met. Soc. of AIME, Vol. 227, Dec. 1963, pp. 1296-1301
22. S. Floreen and R.H. Kane, "An Investigation of the Creep-Fatigue-Environment Interaction in a Ni-Base Superalloy", Fatigue of Eng. Mat. and Struct., Vol. 2, pp. 401-412
23. H.F. Merrick and S. Floreen, "The Effects of Microstructure on Elevated Temperature Crack Growth in Nickel-Base Alloys", Met. Trans. A, Vol. 9A, Feb. 1978, pp. 231-236
24. J.P. Pedron and A. Pineau, "The Effect of Microstructure and Environment on the Crack Growth Behavior of Inconel 718 Alloy at 650 °C Under Fatigue, Creep and Combined Loading, Mater. Sci. and Eng., 56, 1982, pp. 143-156
25. H. Ghonem and D. Zheng, "Depth of Intergranular Oxygen Diffusion During Environment-Dependent Fatigue Crack Growth in Alloy 718", Mater. Sci. and Eng., A150, 1992, pp. 151-160
26. H.H. Smith and D.J. Michel, "Fatigue Crack Propagation and Deformation Mode in Alloy 718 at Elevated Temperatures", Ductility and Toughness Considerations in Elevated Temperature Service, MPC-8, G.V. Smith, ed., The American Society of Mechanical Engineers, NY, 1978, pp. 225-246

27. K.M. Chang, "Metallurgical Control of Fatigue Crack Propagation in Alloy 718", Superalloys 718, 625, 706, and Various Derivatives, E.A. Loria, ed., The Minerals, Metals & Materials Society, 1991, pp. 447-456
28. H. Ghonem, T. Nicholas and A. Pineau, "Elevated Temperature Fatigue Crack Growth in Alloy 718 - Part I: Effects of Mechanical Variables", Fatigue Fract. Engng. Mater. Struct., Vol. 16, No. 5, 1993, pp. 565-576
29. R.P. Skelton and J.I. Bucklow, "Cyclic Oxidation and Crack Growth During High Strain Fatigue of Low Alloy Steel", Metal Science, February 1978, pp. 64-70
30. K. Sadananda and P. Shahinian, "The Effect of Environment on the Creep Crack Growth Behavior of Several Structural Alloys", Mater. Sci. and Eng., 43, 1980, pp. 159-168
31. A. Diboine and A. Pineau, "Creep Crack Initiation and Growth in Inconel 718 alloy at 650 °C", Fatigue Fract. Engng. Mater. Struct., Vol. 10, No. 2, 4, 1987, pp. 141-151
32. K.R. Bain and R.M. Pelloux, "Effect of Environment on Creep Crack Growth in PM/HIP Rene'95", Met.Trans., Vol. 15A, 1984, pp. 381-388
33. M. Gao, D.J. Dwyer and R.P. Wei, "Chemical And Microstructural Aspects of Creep Crack Growth in Inconel 718 Alloy", Superalloys 718, 625, 706 and Various Derivatives, E.A. Loria, ed., The Minerals, Metals & Materials Society, 1994, pp. 581-592
34. K. Sadananda and P. Shahinian, "High Temperature Time-Dependent Crack Growth", Micro and Macro Mechanics of Crack Growth, K. Sadananda, B.B. Rath and D.J. Michel, eds., The Metallurgical Society of AIME, Warrendale, PA 1982, pp. 119-130
35. K. Sadananda and P. Shahinian, "Effect of Environment on High Temperature Crack Growth Behavior of Several Nickel-Base Alloys", Corrosion of Nickel-Base Alloys, ASM, 1984, pp.101-115
36. A. Ghonem, T. Nicholas and A. Pineau, "Elevated Temperature Fatigue Crack Growth in Alloy 718 - Part II: Effects of Environmental and Material Variables", Fat. Fract. Engng. Mater. Struct., Vol. 16, No. 6, pp. 577-590, 1993
37. S. Floreen and R.H. Kane, "Effects of Environment on High Temperature Fatigue Crack Growth in a Superalloy", Met.Trans., Vol. 10, 1979, pp. 1745-1751
38. W.H. Chang, "Tensile Embrittlement of Turbine Blade Alloys After High-Temperature Exposure", Superalloys Processing, AIME, MCIC-72-10, 1972, pp. V1-V41
39. R.H. Bricknell and D.A. Woodford, "The Embrittlement of Nickel Following High Temperature Air Exposure", General Electric Company, Schenectady, NY, Report Number 80CRD164, 1980
40. R.H. Bricknell and D.A. Woodford, "Embrittlement of Nickel Following High Temperature Air Exposure", Met.Trans., Vol. 12A, 1981, pp. 425-433

41. R.H. Bricknell and D.A. Woodford, "The Mechanism of Cavity Formation During Oxidation of Nickel", Acta Metall., Vol. 30, 1982, pp. 257-264
42. D.A. Woodford and R.H. Bricknell, "Grain Boundary Penetration of Oxygen in Nickel and the Effect of Boron Additions", Met.Trans., Vol. 12A, 1981, pp. 1467-1475
43. R.H. Bricknell and D.A. Woodford, "The Effect of High Temperature Air Exposure on the Stress Rupture Life of Nickel and Cobalt Base Superalloys", Superalloys 1980, Proc. 4th Int. Sym. on Superalloys, Seven Springs, PA, ASM, Metals Park, OH, 1980, pp. 633-641
44. D.A. Woodford, "Environmental Damage of a Cast Nickel Base Superalloy", Met.Trans., Vol. 12A, 1981, pp. 299-308
45. D.A. Woodford and R.H. Bricknell, "Environmental Embrittlement of High Temperature Alloys By Oxygen", Treatise on Materials Science and Technology, C.L. Briant and S.K. Banerji, eds., Academic Press, NY, 1983, pp. 157-199
46. J. Reuchet and L. Remy, "Fatigue Oxidation Interaction in a Superalloy - Application to Life Prediction in High Temperature Low Cycle Fatigue", Met. Trans., Vol. 14A, January 1993, pp. 141-149
47. R.H. Bricknell and D.A. Woodford, "Environmental Effects in the Iron Base Alloy IN903A", General Electric Company, Schenectady, N.Y., Report Number 80CRD268, 1980
48. R.H. Bricknell and D.A. Woodford, "Grain Boundary Embrittlement of the Iron-Base Superalloy IN903A", Met. Trans., Vol. 12A, 1981, pp. 1673-1680
49. D. J. Wilson, "Sensitivity of the Creep-Rupture Properties of Waspaloy Sheet to Sharp-Edged Notches in the Temperature Range 1000-1400 °F", J. Basic Eng., March 1972, pp. 13-21
50. D.J. Wilson, "Relationship of Mechanical Characteristics and Microstructural Features to the Time-Dependent Edge-Notch Sensitivity of Inconel 718 Sheet", J. Eng. Mater. and Tech., April 1973, pp. 112-123
51. C.J. Moss and J.W. Martin, "The Effect of Grain Boundary γ' Precipitation on the Stress Rupture Behavior of Nimonic PE16", Materials Forum, 15, 1991, pp. 324-332
52. P. Scott and M. LeCalvar, "Some Possible Mechanisms of Intergranular Stress Corrosion Cracking of Alloy 600 in PWR Primary Water", Presented at EPRI Alloy 600 PWSCC Experts Meeting, Warrenton, VA, March 6-9, 1993
53. E. Andrieu, "Influence de L'environnement sur la propagation des fissures dans un superalliage base nickel, L'Inconel 718", Thesis, Ecole des Mines de Paris, 1987
54. E. Andrieu, R. Molins, H. Ghonem, and A. Pineau, "Intergranular Crack Tip Oxidation Mechanism in a Nickel-Based Superalloy", Materials Science and Engineering, A154, 1992, pp. 21-28

55. E. Andrieu, G. Hochstetter, R. Molins, and A. Pineau, "Oxidation Mechanisms in Relation To High Temperature Fatigue Crack Growth Properties of Alloy 718", Superalloys 718, 625, 706, and Various Derivatives, E.A. Loria, ed., The Minerals, Metals & Materials Society, 1994, pp. 619-631
56. G. E. Wasielewski and R.A. Rapp, "High Temperature Oxidation", The Superalloys, C.T. Sims and W.C. Hagel, eds., John Wiley & Sons, 1972, pp 287-316.
57. H. Ghonem and D. Zheng, "Oxidation-Assisted Fatigue Crack Growth Behavior in Alloy 718 - Part I. Quantitative Modeling", Fatigue Fract. Engng. Mater. Struct., Vol. 14, No. 7, 1991, pp. 749-760
58. D. Zheng and H. Ghonem, "Oxidation-Assisted Fatigue Crack Growth Behavior in Alloy 718 - Part II. Applications", Fatigue Fract. Engng. Mater. Struct., Vol. 14, No. 7, 1991, pp. 761-768
59. R.A. Rapp, "Kinetics, Microstructures and Mechanisms of Internal Oxidation - Its Effect and Prevention in High temperature Alloy Oxidation", Proc. 21st Conference, National Association of Corrosion Engineers, St. Louis, MO, March 1965, pp. 382-400
60. F.H. Stott, G.C. Wood, Y. Shida, D.P. Whittle and B.D. Bastow, "The Development of Internal and Intergranular Oxides in Nickel-Chromium-Aluminum Alloys at High Temperature", Corrosion Science, Vol. 21, No. 8, 1981, pp. 599-624
61. J.H. Swisher, "Internal Oxidation", Oxidation of Metals and Alloys, ASM, OH, 1970, pp. 235-267
62. F.S. Pettit, C.S. Giggins, J.A. Goebel, and E.J. Felten, "Oxidation and Hot Corrosion Resistance", Alloy and Microstructural Design, J.K. Tien and G.S. Ansell, eds., Academic Press, NY, 1976, pp 349-402
63. G.J. Lloyd and J.W. Martin, "The Diffusivity of Oxygen in Nickel Determined by Internal Oxidation of Dilute Ni-Be Alloys", Metal Science Journal, Vol. 7, 1973, p. 74
64. G.J. Lloyd and J.W. Martin, "The Diffusivity of Oxygen in Nickel Determined by Internal Oxidation of Dilute Ni-Be Alloys", Metal Science Journal, Vol. 6, 1972, pp. 7-11
65. J.C. Hwang and R.W. Balluffi, "On a Possible Temperature Dependence of the Activation Energy for Grain Boundary Diffusion in Metals", Scripta Met., Vol. 12, 1978, pp. 709-714
66. Y. Shida, G.C. Wood, F.H. Stott, D.P. Whittle, and B.D. Bastow, "Intergranular Oxidation and Internal Void Formation in Ni-40% Cr Alloys", Corrosion Science, Vol. 21, No. 8, 1981, pp. 581-597
67. G.C. Wood, F.H. Stott, D.P. Whittle, Y. Shida, and B.D. Bastow, "The High-Temperature Internal Oxidation and Intergranular Oxidation of Nickel-Chromium Alloys", Corrosion Science, Vol. 23, No. 1, 1983, pp. 9-25
68. C.S. Giggins and F.S. Pettit, "Oxidation of Ni-Cr Alloys Between 800° and 1200°C", Trans TMS AIME, Vol. 245, December 1969, pp. 2495-2507.

69. N. Birks, Introduction to High Temperature Oxidation of Metals, Edward Arnold Publishers, LTD, London, 1983.
70. C.S. Giggins and F.S. Pettit, "The Effect of Alloy Grain-Size and Surface Deformation on the Selective Oxidation of Chromium in Ni-Cr Alloys at Temperatures of 900° and 1100°C", Trans TMS AIME, Vol. 245, December 1969, pp. 2509-2514.
71. F.H. Stott, Y. Shida, D.P. Whittle, G.C. Wood and B.D. Bastow, "The Morphological and Structural Development of Internal Oxides in Nickel-Aluminum Alloys at High Temperatures", Oxidation Of Metals, Vol. 18, Nos. 3/4, 1982, pp. 127-146
72. Y. Shida, F.H. Stott, B.D. Bastow, D.P. Whittle and G.C. Wood, "Development of Preferential Intergranular Oxides in Nickel-Aluminum Alloys at High Temperatures", Oxidation of Metals, Vol. 18, Nos. 3/4, 1982, pp.93-113
73. S. Guruswamy, S.M. Park, J.P. Hirth, and R.A. Rapp, "Internal Oxidation of Ag-In Alloys: Stress Relief and the Influence of Imposed Strain", Oxidation of Metals, Vol. 26, Nos.1/2, 1986 pp. 77-100
74. K. Mino, A. Ohtomo, and Y. Saiga, "The Effect of Stressing on the Intergranular Oxidation of Inconel 617", J. Japan Inst. Metals, Vol. 44, No. 12, pp. 1397-1403
75. J.H. Weber and H. Sizek, Private Communication from Inco Alloys Int., Huntington, WV, May 27, 1993
76. I.P. Vasatis and R.M. Pelloux, "dc Potential Drop Technique in Creep Stress Rupture Testing", J. Metals, October 1985, pp. 44-49
77. ASTM Book of Standards, E292-83
78. J.I. Goldstein, D.E. Newbury, P.Echlin, D.C. Joy, C. Fiori and E. Lifshin, Scanning Electron Microscopy and X-Ray Microanalysis. A Text for Biologists, Materials Scientists, and Geologists, Plenum Press, 1984, pp. 46
79. L.S. Toma, M.M. Steeves, and R.P. Reed, Incoloy Alloy 908 Data Handbook, M.I.T. Plasma Fusion Center Report # PFC/RR-94-2, March 1994
80. M.F. Asby and B.F. Dyson, "Creep Damage Mechanics and Micromechanics", Advances in Fracture Research (Fracture 84), S.R. Valluri, D.M.R. Taplin, P. Ramarao, J.F. Knot, R. Dubey, eds., Vol. 1, Pergamon Press, NY, 1984, pp. 3-30
81. S.T. Rolfe and J.M. Barsom, Fracture and Fatigue Control in Structures. Applications of Fracture Mechanics, Prentice-Hall, NJ, 1977
82. R.W. Hertzberg, Deformation and Fracture Mechanics of Engineering Materials, J.W. Wiley and Sons, NY, 1976
83. H.E. Boyer, ed., Atlas of Creep and Stress-Rupture Curves, ASM International, Metals Park, OH, 1988

84. H.H. Smith and P. Shahinian, "Effect of An Oxygen Atmosphere on Cyclic Hardening in Type 316 Stainless Steel", Met. Trans. A, Vol. 1, July 1970, pp. 2007-2009.
85. R.M. Goldhoff, "The Evaluation of Elevated Temperature Creep and Rupture Strength Data: An Historical Perspective", Characterization of Materials for Service at Elevated Temperatures, G.V. Smith, ed., ASME, NY, 1978, pp. 247-265
86. J.B. Conway, Numerical Methods for Creep and Rupture Analysis, Gordon and Breach, NY, 1967
87. D.A. Woodford, "Creep and Rupture of an Advanced Fiber Strengthened Eutectic Composite Superalloy", Met. Trans. A, Vol. 8A, April 1977, pp. 639-650.
88. R.G.H. Record, "Oxygen Potential Monitoring of Treatment Atmospheres", Metals and Materials, January 1971, pp. 25-30.
89. A.M. Emsley and M.P. Hill, "Intergranular Oxidation of Silicon in 20 Cr-25 Ni Niobium-Stabilized Stainless Steel at 1140-1230K", Oxidation of Metals, Vol. 34, Nos. 3/4, 1990, pp. 351-360
90. R.G. Iacocca and D.A. Woodford, "The Kinetics of Intergranular Oxygen Penetration in Nickel and Its Relevance to Weldment Cracking", Met. Trans., Vol. 19A, 1988, pp. 2305-2313.
91. G.E. Dieter, Mechanical Metallurgy, McGraw-Hill, Inc., 1976
92. S. Leistiko, "Chances and Limitations of Improved Corrosion Resistance in Oxidising Gases By Cold Working Pre-treatment of Austenitic Cr Ni-Steels", Behavior of High Temperature Alloys in Aggressive Environments, I. Kirman, J.B. Mariott, M. Merz, P.R. Sahm, and D.P. Whittle, eds, The Metals Society, London, 1979, pp. 197-207